Differential Interferometry for Multi-Frequency Ground-Based SAR Systems

A Degree Thesis

Submitted to the Faculty of the

Escola Tècnica d'Enginyeria de Telecomunicació de Barcelona

Universitat Politècnica de Catalunya

by

Sergi López Esteban

In partial fulfilment

of the requirements for the degree in

Grau en Enginyeria de Tecnologies i Serveis de Telecomunicació

ENGINEERING

Advisors: Carlos López & Roger Jové

Barcelona, October 2021

Abstract

Ground-Based Synthetic Aperture Radars (GB-SAR) are a type of Synthetic Aperture Radars (SAR) with a higher flexibility and lower cost than their satellite counterparts. The effectiveness of GB-SAR terrain displacement monitoring has already been proven with bare soils. There is interest in studying their effectiveness in areas covered by vegetation.

The Multi-Frequency GB-SAR system developed by Balamis is able to operate in bands X, C, L and P. A measurement campaign took place in the "Castell de Subirats" to study an area covered by vegetation. Two Trihedral Corner Reflectors (TCR) were placed in the area, one of them surrounded by vegetation. Can we consider the reflectors stable? A big Rock is present in the area but is covered by vegetation. Can it be used as natural reflector for low bands? Is it possible to monitor displacements in the reflectors in all bands?

In X-band the reflectors are not stable because of the surrounding vegetation. In C-band the TCRs are stable. In L-band one of the TCR and the Rock are stable. In P-band only the Rock is stable. The Rock can be used as a reflector and a calibrator for bands L and P as those frequencies can penetrate vegetation. It is possible to monitor the displacements, except in band X because of the phase shifts caused by the vegetation.

Resum

Els Radars d'Obertura Sintètica Terrestres (GB-SAR en anglès) són un tipus de Radars d'Obertura Sintètica (SAR) amb una major flexibilitat i un cost més baix que els seus homòlegs de satèl·lit. L'eficàcia de la monitorització de desplaçaments del terreny amb sistemes GB-SAR ja s'ha demostrat amb sòls nus. Hi ha interès per estudiar la seva efectivitat en zones cobertes de vegetació.

El sistema Multi-Freqüència GB-SAR desenvolupat per Balamis és capaç d'operar a les bandes X, C, L i P. Es va realitzar una campanya de mesura al "Castell de Subirats" per estudiar una zona coberta de vegetació. Es van col·locar a la zona dos Reflectors de Cantonades Trièdriques (TCR), un d'ells envoltat de vegetació. Podem considerar els reflectors estables? Hi ha una gran Pedra present a la zona però està coberta de vegetació. Es pot utilitzar com a reflector natural per a bandes baixes? És possible mesurar els desplaçaments als reflectors a totes les bandes?

A banda X, els reflectors no són estables a causa de la vegetació circumdant. A banda C, els TCR són estables. A banda L, un dels TCR i la Pedra són estables. A banda P, només la Pedra és estable. La Pedra es pot utilitzar com a reflector i calibrador per a les bandes L i P, ja que aquestes freqüències poden penetrar la vegetació. És possible mesurar els desplaçaments, excepte a la banda X a causa de les inestabilitats de fase provocades per la vegetació.

Resumen

Los Radares de Apertura Sintética Terrestres (GB-SAR en inglés) son un tipo de Radares de Apertura Sintética (SAR) con una mayor flexibilidad y un coste más bajo que sus homólogos de satélite. La eficacia de la monitorización de desplazamientos del terreno con sistemas GB-SAR ya se ha demostrado con suelos desnudos. Hay interés por estudiar su efectividad en zonas cubiertas de vegetación.

El sistema Multi-Frecuencia GB-SAR desarrollado por Balamis es capaz de operar en las bandas X, C, L y P. Se realizó una campaña de medida en el "Castillo de Subirats" para estudiar una zona cubierta de vegetación. Se colocaron en la zona dos Reflectores de Esquinas Triédricas (TCR), uno de ellos rodeado de vegetación. Podemos considerar los reflectores estables? Hay una gran Piedra presente en la zona pero está cubierta de vegetación. Se puede utilizar como reflector natural para bandas bajas? Es posible medir los desplazamientos en los reflectores en todas las bandas?

En banda X, los reflectores no son estables debido a la vegetación circundante. En banda C, los TCR son estables. En banda L, uno de los TCR y la Piedra son estables. En banda P, sólo la Piedra es estable. La Piedra se puede utilizar como reflector y calibrador para las bandas L y P, ya que estas frecuencias pueden penetrar en la vegetación. Es posible medir los desplazamientos, excepto en banda X debido a las inestabilidades de fase provocadas por la vegetación.

Acknowledgements

First, I would like to acknowledge and express my sincere gratitude to the advisors and directors of this thesis, Carlos López Martínez and Roger Jové Casulleras, who have supported me throughout the duration of this project and have provided good advice when needed. Thank you for giving me this opportunity.

I would also like to thank my parents and my grandfather for their continuous support and encouragement throughout my life but specially in these last four years of coursing this degree.

Revision History and Approval Record

Revision	Date	Purpose
0	20/08/2021	Document creation
1	21/09/2021	Document inclusion in the template
2	05/10/2021	Document revision
3	12/10/2021	Document final revision

DOCUMENT DISTRIBUTION LIST

Name	E-Mail
Sergi López Esteban	sergi.lopez.esteban@estudiantat.upc.edu
Carlos López Martínez	carlos.lopezmartinez@upc.edu
Roger Jové Casulleras	roger.jove@balamis.com

Written by:		Reviewed and approved by:	
Date	12/10/2021	**Date**	12/10/2021
Name	Sergi López Esteban	**Name**	Carlos López Martínez Roger Jové Casulleras
Position	Project Author	**Position**	Project Supervisors

Table of Contents

List of Figures

List of Tables:

1. Introduction

Synthetic Aperture Radars or SARs are an Earth Observation system that generate high spatial resolution images of an observed area. Typical SAR systems are mounted on airplanes or satellites to capture large areas and take advantage of the movement of the platform. For decades SARs have been used successfully in the monitoring of terrain displacements with a technique named Interferometric SAR or InSAR. InSAR focuses in the study of the phase difference between two or more images of the same area to measure the movement. The use of multiple frequencies in a single mission provides much more information as waves have different penetration depths depending on their wavelength. This penetration is extremely useful in the case of areas covered by vegetation.

Some years ago, the idea of a more flexible and accessible SAR platform surged, the Ground-Based SARs. This GB-SARs solve some of the problems inherent with aerial platforms but are affected by other limitations. Despite this limitations GB-SARs have been proven effective in the monitoring of terrain displacements in small uncovered areas, for example an open pit mine where the bare soil is easily measured. What has not been deeply studied in GB-SAR systems is the use of multiple frequencies and the efficiency of the monitoring in areas covered by vegetation.

The aim of this thesis is to study the efficiency of terrain monitoring in a vegetated area with a Multi-Frequency GB-SAR. The main objectives of this thesis are:

1. To test the stability of artificial reflectors placed in an area with vegetation in different frequency bands.
2. To investigate the viability of using a natural object such as a big rock from the scenery as a reflector and calibrator for low frequency bands.
3. To study the accuracy of the computed differential interferograms in the measurement of terrain displacements from 1cm to 1mm in different bands.

The basis of this work is a Multi-Frequency Ground-Based Synthetic Aperture Radar developed by Balamis in collaboration with the UPC in the frame of the industrial Ph.D. of Dr. Adrià Amézaga. The data comes from a measurement campaign performed by Balamis in the “Castell de Subirats”, near Barcelona on June 2020. The idea is to process the data from this measurement campaign to study the stability of the reflectors and assess the viability of measuring terrain displacement through vegetation using a Ground-Based SAR. The code used in the measurement campaign developed by Balamis, has been given to provide an idea of were to start coding.

The data is processed with the use of Python scripts. Python is a general-purpose programming language whose design philosophy emphasizes easy code readability. Python is a highly extensible programming language, as external modules, libraries and packages can be easily and efficiently incorporated. The scripts in Python are executed using Anaconda Navigator, which is a distribution of the Python language that provides an easy to operate Graphical User Interface and simplifies package management. A number of Python libraries are used in the scripts to aid in the processing of the data and the display of the results. Three of those libraries are NumPy, Matplotlib and Scipy, among others. The data is processed in two different terminals. My personal laptop and the computing services CALCULA from the CommSensLab Group from the Department of Signal Theory and Communications (TSC). The scripts that require little computational power are executed in my laptop. But the ones that require high computational power, for example the extraction of the Differential Interferograms for all images in all bands, are executed in the CALCULA server as they take a bit of time to finish. The results of these scripts usually take the form of images, charts and tables.

This Final Report for the thesis is structured in seven separate chapters and the appendices. Chapter 1, this same chapter named “Introduction”, includes the objectives and aims of this thesis, the breakdown of the Work Plan and the deviations from the initial plan. Chapter 2, named “Background & State of the Art of the Technology”, includes a theoretical overview of Radars, Synthetic Aperture Radars or SARs and Ground-Based SARs. Chapter 3, named “System Summary & Data Acquisition”, includes a presentation of Balamis, a description of the GB-SAR system developed by Balamis and the description of the measurement campaign in the “Castell de Subirats”. Chapter 4, named “Data Analysis”, includes an initial look into the images provided after processing the data from the measurement campaign and a description of the calibration applied to the data. Chapter 5, named “Stability Analysis”, studies the stability of the reflectors in the scenery. It includes the temporal evolution for the amplitude and phase for the pixels of the reflectors and the differential interferometric evolution. Chapter 6, named “Probability Model Analysis”, studies the statistical behaviour of the SAR images. It includes an overview in SAR probability models and the comparison between histograms and Probability Density Functions. Chapter 7, named “Conclusions and future development”, includes the final conclusions for this thesis and provides some ideas for future investigations. The Appendices include all the figures and graphs obtained as result in this thesis. Within the chapters only some of the figures are present to not clutter the text with images. In the Appendices the mentioned figures in the text are presented with greater detail.

This project’s Work Plan can been broken down into five separate Work Packages (WP). The five WP are: Bibliography, Software Development, Data Processing, Conclusions and Report Writing. Below each WP is described with its internal tasks in Table 1.1 and a Gantt diagram is shown in Figure 1.1.

Project: Bibliography	
Major constituent: Learning and Research	**WP ref:** WP1
Short description: Obtain and read any documentation that will help during the development of the project.	**Planned start date:** 15/02/2021 **Planned end date:** 19/03/2021
Internal task T1: Revise class notes from the RADAR course and the radar section in the TELED course from last quadrimester. **Internal task T2:** Read documentation such as Luca Pipia's PhD thesis "Polarimetric Differential SAR Interferometry with Ground-Based Sensors" and book "Synthetic Aperture Radar Signal Processing with MATLAB Algorithms" by Mehrdad Soumekh.	
Project: Software Development	
Major constituent: Software	**WP ref:** WP2
Short description: Understand the source code from Balamis and develop the code to test the stability and statistical behavior of the data.	**Planned start date:** 15/03/2021 **Planned end date:** 02/07/2021
Internal task T1: Learn Python language and read the source code from Balamis. **Internal task T2:** Develop code to test stability of the data. **Internal task T3:** Develop code to study the statistical behavior of the data.	
Project: Data Processing	
Major constituent: Software	**WP ref:** WP3
Short description: Process the already given data in the developed software.	**Planned start date:** 03/05/2021 **Planned end date:** 16/07/2021
Internal task T1: Test stability of the reflectors. Test validity of data provided. **Internal task T2:** Obtain the Interferograms and study the differential interferometric phase. **Internal task T3:** Study the statistical behavior of the data.	
Project: Conclusions	
Major constituent: Analysis	**WP ref:** WP4
Short description: Extract conclusions from the results obtained in the project.	**Planned start date:** 07/06/2021 **Planned end date:** 30/07/2021
Internal task T1: Extract conclusions from the stability analysis of the data. **Internal task T2:** Extract conclusions from the probability model analysis of the data.	
Project: Report Writing	
Major constituent: Writing	**WP ref:** WP5
Short description: Write the final report and prepare the final presentation.	**Planned start date:** 02/08/2021 **Planned end date:** 22/10/2021
Internal task T1: Write the final report for the project. **Internal task T2:** Prepare presentation for the project defense.	

Table 1.1: Work Plan Breakdown

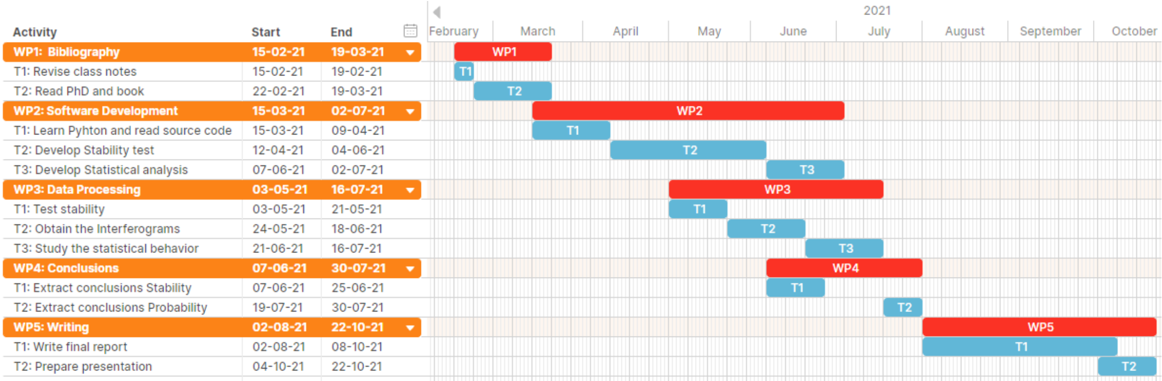

Activity	Start	End
WP1: Bibliography	**15-02-21**	**19-03-21**
T1: Revise class notes	15-02-21	19-02-21
T2: Read PhD and book	22-02-21	19-03-21
WP2: Software Development	**15-03-21**	**02-07-21**
T1: Learn Pyhton and read source code	15-03-21	09-04-21
T2: Develop Stability test	12-04-21	04-06-21
T3: Develop Statistical analysis	07-06-21	02-07-21
WP3: Data Processing	**03-05-21**	**16-07-21**
T1: Test stability	03-05-21	21-05-21
T2: Obtain the Interferograms	24-05-21	18-06-21
T3: Study the statistical behavior	21-06-21	16-07-21
WP4: Conclusions	**07-06-21**	**30-07-21**
T1: Extract conclusions Stability	07-06-21	25-06-21
T2: Extract conclusions Probability	19-07-21	30-07-21
WP5: Writing	**02-08-21**	**22-10-21**
T1: Write final report	02-08-21	08-10-21
T2: Prepare presentation	04-10-21	22-10-21

Figure 1.1: Gantt Diagram of the Work Plan

The Work Plan for this project has some differences with the original Work Plan described in the Project Proposal document. Some of the changes in the Work Plan were induced by incidences along the way.

The first difference is the change in the source code. Initially, the idea was to use the MATLAB code developed by Luca Pipia in his Ph. D. It was changed to the Python code developed by Balamis and used in the measurement campaign from where the data comes from. This change caused some difficulties as I had no previous experience with Python and some time was required to learn it properly. The second difference is the data. The data from the Subirats measurement campaign was provided in a number of formats, from the raw data generated by the system to the already focused Single Look Complex images. The initial idea was to start with the raw data and process it all the way with the help of the source code provided by Balamis. The problem was that the processing required the Library CuPy, which uses CUDA toolkit. There were some incompatibilities between the available hardware, basically the GPU, and the requirements from CUDA. To overcome this it was decided to use directly the provided focused SLC images from the measurement campaign. Thus the original task of creating the data cubes and processing the raw data was eliminated from the Work Plan. The third difference is the elimination of the additional measurement campaign described in the Project Proposal. The fourth and final difference is the inclusion of a Statistical and Probability Model Study in the project. This study aims to observe the statistical accuracy of the data and tries to set some connections with the results from the Stability Analysis.

There were no major incidences throughout this project. Most of the problems and small incidences were caused by my inexperience with the use of the Python programming language and the CALCULA computing services from the Department of TSC. The majority of the problems were solved after some online research, but the ones concerning the CALCULA server were solved after asking to the Computer Services of TSC via mail.

2. Background & State of the Art of the Technology

A RADAR, acronym for RAdio Detection And Ranging, is a system used to detect and observe objects, both static and moving objects, through electromagnetic radio waves. A radar can obtain the distance or range to the object and its velocity.

The radar systems first appeared in the 1930s, just before Word War II. The term radar would be coined in 1940. During the war, radars were extensively and successfully used in the detection of airplanes and other flying artefacts. Although it was created for its use in the military field, many other applications for the radar appeared in the following decades. Nowadays, one of the most important and impactful radar applications is remote sensing and Earth observation. From meteorological to terrain monitoring and terrain classification, radars are able to obtain two-dimensional or three-dimensional images of a desired area. These images are then used in various areas of knowledge with diverse purposes. In radar imaging the direction of the line of sight from the radar is called Range and the direction perpendicular to the Range is the Azimuth.

The radar system is very similar to the usual telecommunications system. Unlike in the telecommunications system, the radar does not transmit information, it creates the information using the propagation and reflection of the waves. It is basically composed of 2 parts, the transmitter or Tx and the receiver or Rx. The transmitter, as its name implies, is responsible for the emission of the radio waves in the direction of the object of interest. The receiver is responsible for the reception of the radio waves scattered by the object and its posterior processing. The Tx and the Rx of a radar system can be joined in the same location, which is called a monostatic radar, or separated a certain distance, which is called a bistatic radar.

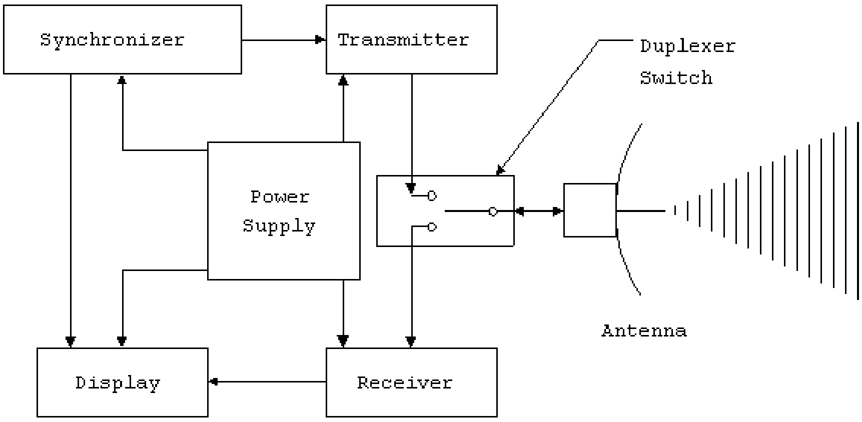

Figure 2.1: Basic Block Diagram of a Monostatic RADAR

In a more analytical and mathematical approach, the basic functioning of a radar is quite simple. The system emits a radio wave with a certain power and polarization at the selected wavelength. Depending on the wavelength and the target of interest the scattering or reflection of the wave varies. The range of the target depends on the time it took for the wave to return. The velocity of the target depends on the variation in the carrier frequency of the wave, the called Doppler shift. Other properties of the target may be obtained from the power, the phase or the polarization of the scattered wave.

The images obtained by a radar, like other common digital images, are made of pixels. The resolution of these pixels is the minimum distance between two or more targets for the radar to detect them individually. In the range direction the resolution, which is called range resolution, is inversely proportional to the Bandwidth of the transmitted signal. In the azimuth direction the resolution is called angular resolution, it is proportional to the beamwidth of the antenna, which is at the same time inversely proportional to the size of the antenna for a given wavelength. The angular resolution for a given wavelength is inversely proportional to the size of the antenna. This connection arises a big problem in that for a really high resolution in azimuth a really big or long antenna is required. Some resolutions are unreachable because of the unfeasibility of building a large enough antenna.

A new type of radar, the Synthetic Aperture Radars, were developed to overcome this limitation of conventional radar systems.

2.1. Synthetic Aperture Radar

The Synthetic Aperture Radar or SAR is a type of radar system that uses the movement of the antenna to simulate a bigger antenna. It allows for a much finer azimuth resolution than conventional radar systems. In SAR imaging the resolution is proportional to the antenna size, unlike conventional radar systems. SAR systems are generally mounted on airplanes or satellites to create images of areas from Earth or even other planets.

The first SARs appeared in the sixties, mainly in military applications. In 1978 the fist civil SAR satellite was launched, the SEASAT mission. Many other SAR missions have been launched over the years, such as the ERS-1/2 and Sentinel-1 from the European Space Agency (ESA). Nowadays SAR imagery is one of the most powerful tools for Earth observation, reaching very high resolutions from space.

Figure 2.2: Satellite mounted SAR, Sentinel-1 by ESA

Some new techniques appeared to further expand the power of SAR imagery. Two of these techniques are Polarimetry and Interferometry. SAR Polarimetry or PolSAR focuses on the study and interpretation of the polarization of the radio waves. Different wave polarizations interact differently with different objects. SAR Interferometry or InSAR focuses on the study of the phases between different images. InSAR is used to create Digital Elevation Model (DEM) and detect terrain deformations. InSAR uses two or more images of the same area, either images taken at different moments in time or images taken from different positions, to create Interferograms. About the images, the one used as reference is referred as Master and the rest of them are referred as Slaves. The changes in phase in the Interferogram could be cause by a terrain displacement, changes in the atmospheric conditions or noise, among others. After compensating the other phase shifts, it is possible to measure the displacement as:

$$\Delta\varphi=\frac{4\cdot\pi}{\lambda}\cdot\Delta d$$

Where $\Delta\varphi$ is the phase shift in radians and Δd is the displacement in the slant range in metres.

Another technique that further expands the power of PolSAR and InSAR is the use of Multi-Frequency analysis. The idea is to use two or more frequency bands to capture the same area and compare both images to obtain more information. Different frequency mean different wavelengths that interact differently with the targets and the terrain. Objects smaller than the wavelength do not reflect as much signal as objects bigger than the wavelength. This is because the Radar Cross Section or RSC of a target depends on its size relative to the wavelength of the signal. When talking about terrain a more precise explanation is the Speckle Phenomenon. The lower the wavelength the higher the number of independent scatterers in an area and thus more signal is backscattered. Another important aspect of Multi-Frequency analysis is the different penetration values for different wavelengths. The penetration depth depends on the material and also on the frequency. Lower frequencies have higher wavelengths and thus have more penetration capabilities than higher frequencies. This is particularly interesting and useful in areas under vegetation or with snow cover. In the case of vegetation, a high frequency signal is reflected on the canopy of the trees, a middle frequency signal is reflected inside the canopy and on the trunk of the trees, and a low frequency signal is reflected on the soil under the trees.

The idea of SARs is quite simple. Instead of building an incredibly big antenna, it is possible to electronically simulate a bigger antenna or aperture by moving the platform where the SAR is mounted. Generally the platform is a satellite or an airplane. Each acquisition along the aperture is recombined to create the high resolution image. The system is required to have a stable and coherent transmitter to successfully recombine all the acquisitions.

The high definition aerial SAR images are so powerful because of a few reasons. But first it is necessary to define the range and azimuth. The range is the direction of the boresight from the radar, perpendicular to the trajectory of the platform. The azimuth is the direction parallel to the trajectory of the platform, perpendicular to the range. The azimuth direction is also called cross-range direction in SAR.

The first reason is that the cross-range resolution is constant throughout the image, independent of the range. The reasoning behind is that the aerial platform has no physical limitation on the length of the aperture and the fact that distant ranges are illuminated more time by the radar.

Another reason is the high spatial resolution. The range resolution, like in conventional radar systems depends on the bandwidth of the emitted signal, the higher the bandwidth the higher the resolution. The azimuth resolution is different from conventional radars. It is approximately half of the real length of the antenna. This is the most significant result of SAR imaging. Unlike in conventional radars where a bigger antenna is required to obtain a higher resolution, SARs require a small antenna to obtain higher resolutions.

As a summary, Synthetic Aperture Radars or SARs are able to produce images with very high and constant spatial resolution thanks to their electronically simulated aperture but at the cost of requiring more computational power and complexity than conventional radar systems.

2.2. Ground Based – Synthetic Aperture Radar

Synthetic Aperture Radars or SARs have proven to be a very powerful tool. Creating very high definition images of extensive areas. As their usefulness increased, some limitations were found for satellite and airborne SARs. These limitations are intrinsically related to the platform the radar is mounted on. A new trend for SAR systems has surged in the recent years to counteract some of these limitations, the Ground Based SARs or GB-SARs. This systems, as their name suggest, are placed on the ground in a mobile platform, instead of being mounted in a satellite or flying aircraft.

The biggest limiting factor for satellite and airborne SARs is their price. The cost of creating and operating the platform is very high. Such expenses cannot be afforded by everyone. Another limiting factor is the observation geometry from satellites and airplanes. Although the area illuminated can be quite wide, the geometry is not ideal for steep and complex terrains such as the ones in a mining facility or natural gorges and canyons. Another limiting factor is the high revisit time, which is higher in satellites than in airplanes. It limits the amount of captures the sensor can make inside a certain time frame, thus limiting the amount of information created. This makes satellite and airborne SARs unfit for monitoring fast changing processes and small-scale phenomena.

GB-SARs appeared to counter these limitations. Firstly, GB-SARs are much less expensive to create and operate, thus making them more accessible. Secondly, GB-SARs are much more flexible than aerial SARs. It can be easily deployed almost everywhere to better illuminate the area of interest with the optimal observation geometry. Thirdly, the revisit time is very low. It can be as low as few minutes per capture. Finally, the terrestrial platform is very stable and we have perfect knowledge of the sensor's position. Which allows for precise interferometric studies. This makes GB-SARs optimal for the monitoring fast changing processes and small-scale phenomena such as landslides.

GB-SARs counteract some of the limitations of space and aerial platforms but have some other specific limitations on their own. The most obvious limitation of a ground based platform is the extension of the illuminated area and the maximum range. Unlike in space or air, the platform is surrounded by terrain that limits it. Another inconvenient of the terrestrial platforms is that the azimuth resolution is not as perfect as in satellite or airborne SARs. First of all, the azimuth resolution is no longer proportional to the size of the antenna, but instead is inversely proportional to the length of the rail, which is the length of the synthetic aperture. Because of that the longest possible rail within practical bounds is used. Usually the selected length is around two meters. Furthermore, the azimuth resolution is not constant throughout the image. It decreases with the range and the azimuth angle. The azimuth resolution is sometimes expressed as angular resolution in degrees instead of meters. The angular resolution is not dependent on the range but it still decreases with the azimuth angle.

There are various types of GB-SARs, depending on the type of rail along which the sensor moves to create the synthetic aperture. The most common and simple one is the Linear GB-SAR, where the sensor moves along a linear rail. As said before, usually the rail has a longitude of around two meters. Another type is the Circular GB-SAR, where the sensor is mounted in a circular rail that provides 360º coverage. The angular resolution in this radars is constant but for distant targets a defocusing effect appears. There is another type of GB-SAR that does not move the sensor along a rail, but instead has many antennas positioned strategically in space to simulate the aperture. It is called the Multiple Input Multiple Output (MIMO) GB-SAR. It has no mechanical moving parts but it requires a much higher computational power.

The images from a SAR are defined in the range (perpendicular to the trajectory) and azimuth (parallel to the trajectory) dimension. In the case of a GB-SAR, the dimensions need to be redefined as the synthetic aperture, the length of the rail, is much shorter than the area of interest. It is the case of a Short Synthetic Aperture or SSA. The range is defined as the radial distance from the center of the synthetic aperture. The azimuth is defined as the angular position. Because of this definition, the images from a GB-SAR can be represented with Polar or with Cartesian coordinates. An image with Polar coordinates represents the range in meters and the azimuth in degrees. An image with Cartesian coordinates represents the range and azimuth in meters. Because of the decrease in azimuth resolution with the range, in Cartesian images the factor of spatial oversampling increases drastically with the range. As a result Cartesian images are unsuitable for areas with range variations higher than 1 kilometre because of the oversampling. Although both images have the same information, Cartesian images are much bigger, have more pixels, than Polar images. Usually the range dimension is represented on the horizontal axis of the image and the azimuth domension is represented on the vertical axis of the image.

3. System Summary & Data Acquisition

Balamis Microwave Sensors and Electronics S.L. is a company specialized in the development and manufacture of cost-effective airborne and ground-based radars and radiometers. Balamis is settled in La Granada, province of Barcelona, Spain.

Figure 3.1: Balamis' Logo

Since its creation in 2015 as a spin-off company from the Remote Sensing Laboratory of the Universitat Politècnica de Catalunya (UPC), Balamis has converted the original university prototypes into industrial products. Balamis has been supported by the European Space Agency incubation program, the European Institute of Technology, and the Spanish agencies CDTI and ENISA.

Balamis has developed two L-band radiometers and a multi-frequency GB-SAR.

3.1. System Summary

Balamis in collaboration with UPC has developed, in the frame of the industrial doctorate of Dr. Adrià Amézaga, the first commercial prototype of a multi-frequency Ground Based Synthetic Aperture Radar.

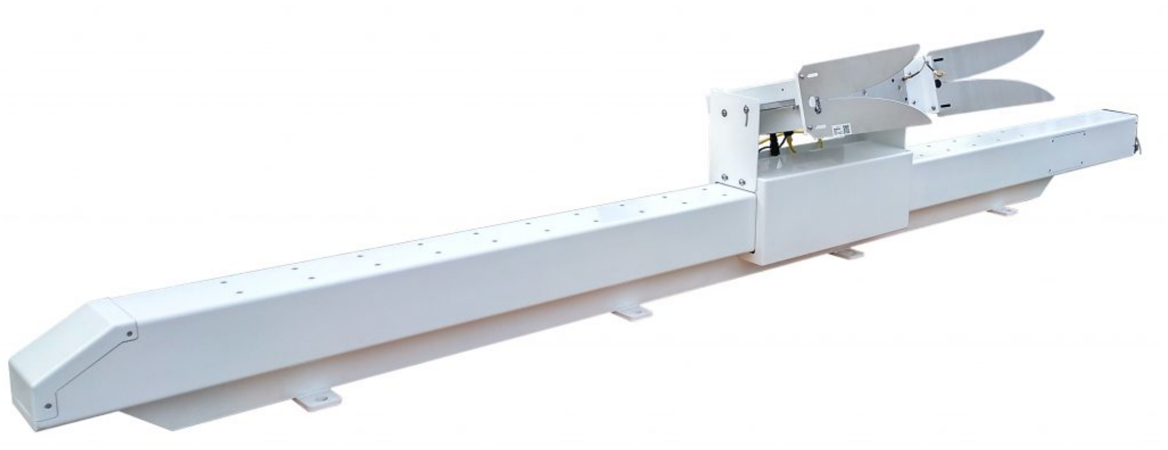

Figure 3.2: Multi-Frequency GB-SAR developed by Balamis

The GB-SAR is a Frequency Modulated Continuous Wave (FMCW) radar implemented with Software Defined Radio (SDR) devices. The GB-SAR is capable of operating in both real and synthetic aperture modes. In the latter, stop&go and fast continuous acquisitions are possible. The sensor operates at P, L, C and X-bands. S and Ku-bands are available upon request. The sensor is able to transmit and receive in both Vertical (V) and Horizontal (H) polarization.

Some of the main technical specifications of the system are:

- Aperture length of 2 m
- Output power is 27 dBm
- Long range measurement up to 4 km
- Acquisition time in On-The-Fly mode: 10s per frequency & 2min all four frequencies
- Acquisition time in Stop&Go mode: 3min per frequency & 15min all four frequencies
- Total weight is 100 kg
- Frequencies, Bandwidths and Resolutions in Table 3.1

Band	**Frequency**	**Bandwidth**	**Range Resolution**	**Azimuth Resolution @ 1km**
X	9,6 GHz	200 MHz	0,75 m	7,8 m
C	5,4 GHz	200 MHz	0,75 m	13,8 m
L	1,27 GHz	160 MHz	0,93 m	59 m
P	0,45 GHz	80 MHz	1,87 m	172 m

Table 3.1: Frequencies, Bandwidths and Resolutions for Balamis' GB-SAR

3.2. Measurement Campaign in Subirats

Balamis realized a measurement test campaign for the Multi-Frequency GB-SAR on the 22nd of June 2020. The campaign took place in the Castell de Subirats, west of Barcelona, Spain. The test consisted in capturing during a 3-hour period a vegetated area from the Castle where two corner reflectors had been placed. The only polarization used by the radar in this capaign is VV.

Figure 3.3: Castell de Subirats orthophoto. Radar & Reflectors positions

The area of interest is a hill facing South-West from the castle. The hill is composed by two vegetated areas separated by a road. The radar was located at 41º24’57,9’’N & 1º48’59,2’’E, at 289 m above the sea level, with a depression angle of 10º, looking at the road. This area was selected because its geometry is adequate to recreate the incidence angles of typical satellite SAR images. The corner reflectors used were Trihedral Corner Reflector or TCR. The first TCR had a side of 60 cm and it was placed just behind the road, surrounded by vegetation. Hereafter this TCR is denoted as Corner Large or CL. The second TCR had a side of 30 cm and it was placed next to the road. Hereafter this TCR is denoted as Corner Small or CS. From the scene two other objects require mention. The first one is the road itself, as it will be visible on some of the bands. The metal guardrails along the road strongly reflect the signal. The second one is a big rock covered by vegetation situated below the road. This rock will be used to test vegetation penetration and as a natural reflector for the lower bands. Hereafter this natural reflector is denoted as ROCK.

From this test measurement campaign a number of images for each band where captured in the 3-hour period, from 13:17 hour to 16:21 hour. For X-band and C-Band a total of 21 images were taken. For L-band a total of 20 images were taken. Finally, for P-band a total of 18 images were taken.

4. Data Analysis

From the measurement test campaign some images where captured. These images are stored in Single Look Complex or SLC format. In this format each pixel is represented by a complex (I & Q) number so it contains both amplitude and phase information.

As said before, GB-SAR images can be represented in Polar or in Cartesian coordinates. The horizontal axis corresponds to the range dimension and the vertical axis corresponds to the azimuth dimension. The range dimension is always represented in meters. The azimuth dimension is represented in degrees in a Polar image and in meters in a Cartesian image. This change of magnitude means an oversampling appears in the Cartesian image as range increases. Both formats of images are available from the measurement campaign in Subirats. After some thinking about which type of image should be used in this study we decided to use the Cartesian images. The selected format is the Cartesian images because it represents a more realistic image of the captured area and it makes it easier to identify the scatterers. Although some oversampling will appear at the higher ranges, because of the short maximum range of 170 meters for the image, little oversampling will happen and its effect will be low. To summarize, by using a Cartesian image we get a more realistic representation of the captured area at the cost of some minor oversampling at the higher ranges.

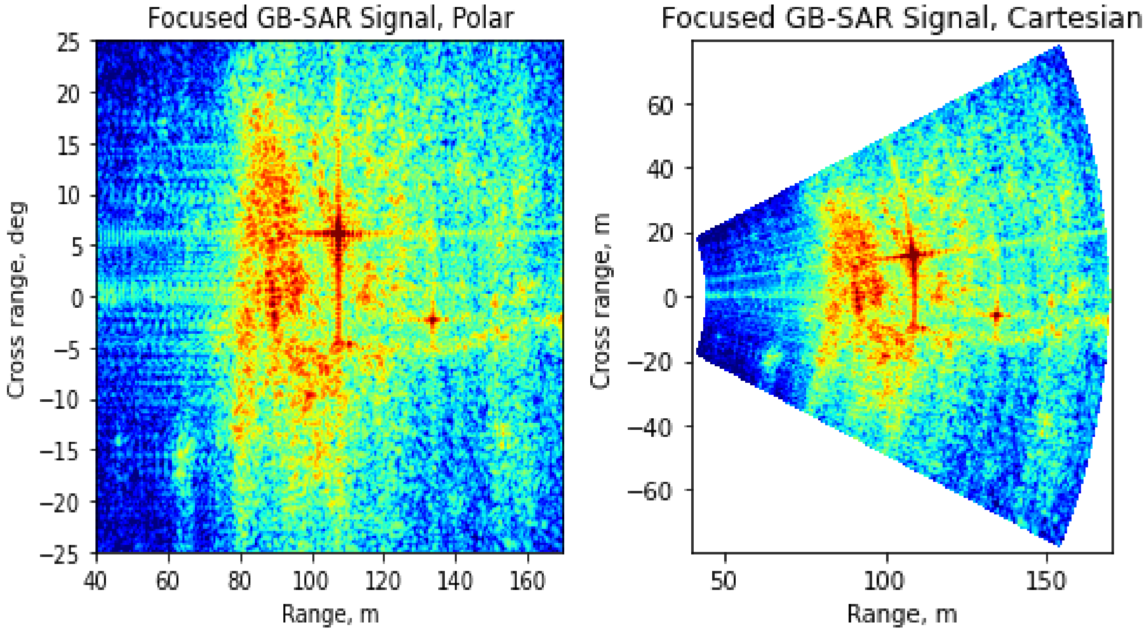

Figure 4.1: Absolute Power Images for X-band. Polar & Cartesian

4.1. Acquired Images

The images captured from the Castell de Subirats correspond to an area that goes from 40 to 170 meters away from the radar and up to 79,3 meters to each side of the sensor. At each frequency band the obtained image is different because of the different spatial resolution at each frequency and the different properties of each band.

In this section we will focus on the absolute amplitude information of the image. We are interested on the absolute power or modulus information of each pixel to identify the reflectors and landmarks of the captured area. Below is shown the first of the images taken at each band during the measurement campaign. The absolute amplitude is uncalibrated in the images and it is shown in logarithmic scale.

The GB-SAR does not appear in the image, it is located left of the image in the middle of the vertical axis The big reflector, the CL is the one located closer at around 110 meters from the radar looking a bit to the left. The small reflector, the CS is the one located far away at around 135 meters from the radar looking a bit to the right. The CL reflects a higher amplitude than the CS because of its bigger size. The natural reflector, the ROCK, is located at around 90 meters approximately in the centre.

All the figures can be seen with detail in the Appendices Section 1.1.

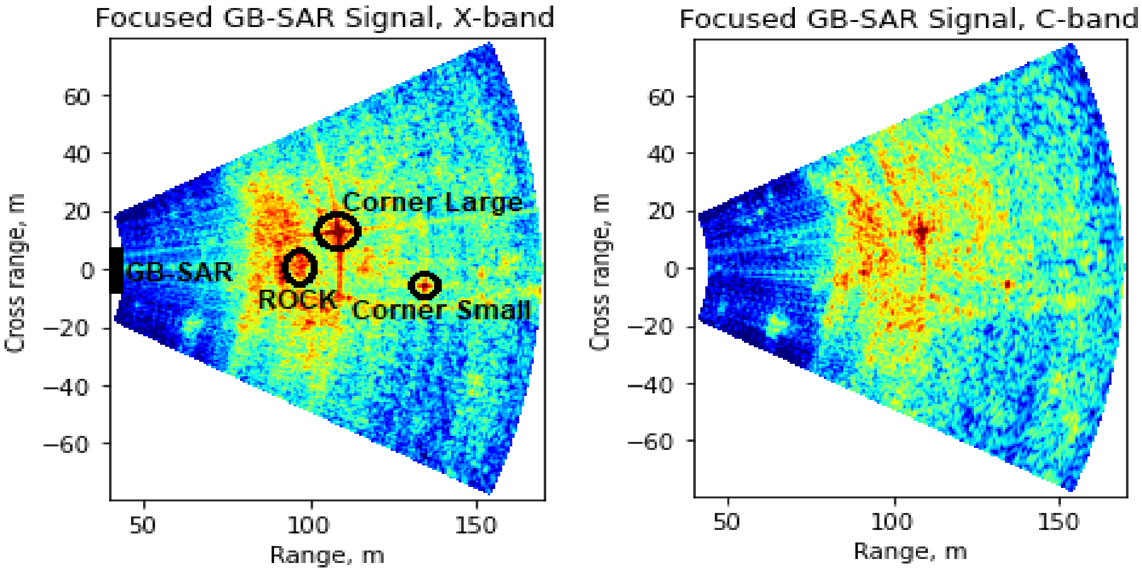

Figure 4.2: Absolute Power Images. 1st Acquisition for X-band & C-band

At first glance we can see a big difference between the images for X and C-band and the images for L and P-band.

In X-band the image is very clear. Both TCRs are easily identifiable in the image with their secondary lobes spreading through the image. The road can also be discerned although it is not as clear as the TCRs. Below the road some strong reflections appear probably caused by trees and parts of the ROCK uncovered by vegetation. Although strong reflectors, they are not very stable and change with every picture.

In C-band the image is still quite clear. Both TCRs are easily identifiable although their secondary lobes spread less than in the previous band. The road is more visible at this band because the bigger pixel size entails less variations in the reflections along the road. There is also the same unstable reflectors below the road. Some parts of the ROCK not covered by vegetation might be visible.

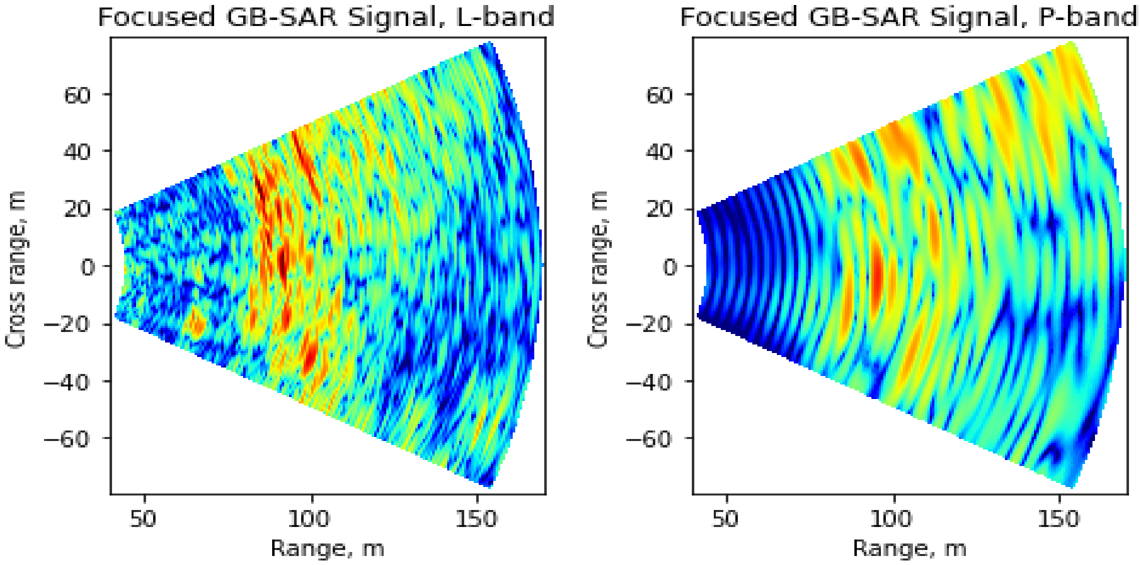

Figure 4.3: Absolute Power Images. 1st Acquisition for L-band & P-band

In L-band the image is not as clear. The CL cannot be identified by simply looking at the image, but by looking into the pixels where it should be a strong reflection is seen in all the images, therefore we can consider that the CL is visible with L-band. The CS cannot be identified and it is considered invisible in this band. The same happens for the road. For the ROCK, some very large and strong reflection is seen, it is clearly visible in this band. Some other strong reflections appear in the image and correspond to the soil below the vegetation.

In the P-band the image is even less clear. None of the TCRs nor the road are visible in this band. On the contrary, the ROCK is very clearly visible in this band, it is the strongest reflector in the image. Some other strong reflections appear in the image but are not as stable as the rock. This other reflections are the soil below the vegetation, as the P-band wave can easily penetrate vegetation.

4.2. Calibration

One of the most important aspects of radar processing is the calibration of the data. Calibration is needed to clearly see what is happening to the data and compare various dataframes with each other under the same reference. In SAR and GB-SAR imaging the calibration is crucial to check the stability of the image and observe the differences between images. It is critical in InSAR, as the phases have to be perfectly calibrated to obtain a valid result.

In SAR and GB-SAR images in SLC format the calibration consists in normalizing the whole image by a given absolute power and a given phase. The calibration is computed as:

$$S_{calib}=\frac{S}{P}=\frac{|S|\cdot e^{j\Phi_S}}{|P|\cdot e^{j\Phi_P}}=\frac{|S|}{|P|}\cdot e^{j(\Phi_S-\Phi_P)}$$

Where S is the SAR image, with each pixel having an amplitude and a phase. P is the calibration values, with |P| being the modulus and Φ_P being the phase.

Depending from where the values for this given magnitudes are obtained we can differentiate two types of calibration: Internal and External. In the Internal Calibration the references are obtained by the system itself. The system automatically makes an observation before every capture to get the phase and the total gains of the system to calibrate the measure. In the External Calibration the references are external to the system. A measure of an external target or calibrator, it can be a TCR with a very strong and stable reflection, is used to calibrate the whole image. Both types of calibrations are important as the Internal compensates the system's phase drift and amplitude gains whereas the External references all the measures to a strong a stable calibrator.

In satellite mounted SARs both calibrations are used simultaneously. Every capture is internally calibrated to compensate the phase and the gains of the system. Every measure is then referenced to an external calibrator measured previously. This external calibrator is usually an immense TCR placed in a very flat area such as a desert and it is measured every now and then. All images are referenced to this calibrator wherever it might be placed. In GB-SAR both calibrations are used although not simultaneously. I this project the internal calibration is used to check the stability of the images and study its statistical properties. The external calibration is used to compare images between them and compensate some of the slow atmospheric effects such as changes in temperature and humidity.

To perform the Internal Calibration we used as reference the observation amplitude and observation phase stored automatically by the system before each acquisition. Each image at each band is calibrated by its observation references. This observation references where stored in files and they are applied to their respective image.

To perform the External Calibration things got less simple. We decided to calibrate each image with respect to a reference within the same image as the calibrators used are quite stable. The external reference used as a calibrator depends on the frequency. In X and C-band the two TCR were candidates to become a calibrator. In the end we decided to use as a calibrator the CS. Even though the CS is smaller and thus less signal is reflected than in the CL, some strong changes in phase appear in CL at X-band that make it less stable. In L-band there were also two candidates for the calibrator, the CL and the ROCK. Both candidates perform similarly and have similar stability in phase, but in the end we decided to use as a calibrator the ROCK because the reflected power is higher. In P-band there is only one candidate to become the calibrator, the ROCK, as neither of the TCRs are visible in this band. To summarize, in X and C-bands the selected calibrator is the CS and in L and P-bands the selected calibrator is the ROCK.

5. Stability Analysis

Stability in a GB-SAR image is defined as the constant non variation of the values of a certain pixel throughout multiple acquisitions at the same band. If the amplitude and phase of a pixel are constant and do not change much between various acquisitions, then the pixel is considered stable. Stability is very important for various reasons. The first one is the need for calibration. To successfully carry out an external calibration a stable calibrator is required, otherwise the whole image will be affected by the instabilities of the calibrator. The second one is InSAR. Comparing phases between images to find out target or terrain displacements is useless if the phases are unstable and randomized.

In this project we are really interested in knowing the stability of the reflectors in the captured area: the two TCRs and the ROCK.

All figures and plots mentioned are visible with greater detail in the Appendices Section 2.

5.1. Reflector Stability

The first task is to study the stability of the calibrated images by themselves. We are interested in seeing constant amplitudes and phases throughout the images in the reflectors from the scenery. As the different acquisitions were taken consecutively in different moments in time, we can consider this as seeing the temporal evolution of the calibrated reflectors. Specific pixels were selected from the image. A pixel from each of the TCRs was selected. Three different pixels from the ROCK were selected as it is a big target. Two other pixels from the image were selected randomly to observe the difference between a reflector and the scenery. The uncalibrated images will not be used in this study. These images provide little information as the amplitudes and phases are affected by the internal shifts of the system.

Firstly, we will start with the images Internally Calibrated. At first glance we can see some stability in the reflectors. As expected on both randomly selected pixels, the amplitude and phase jump all over the place.

Below, in Figure 5.1, are shown the plots of the temporal evolution for the amplitude in dB and the phase in degrees for the selected pixels at each band. Also in Table 5.1 are shown some statistical values about the stability of the phases of the selected pixels. To compute the statistical values the phases for the CL and CS in X-band have been unwrapped.

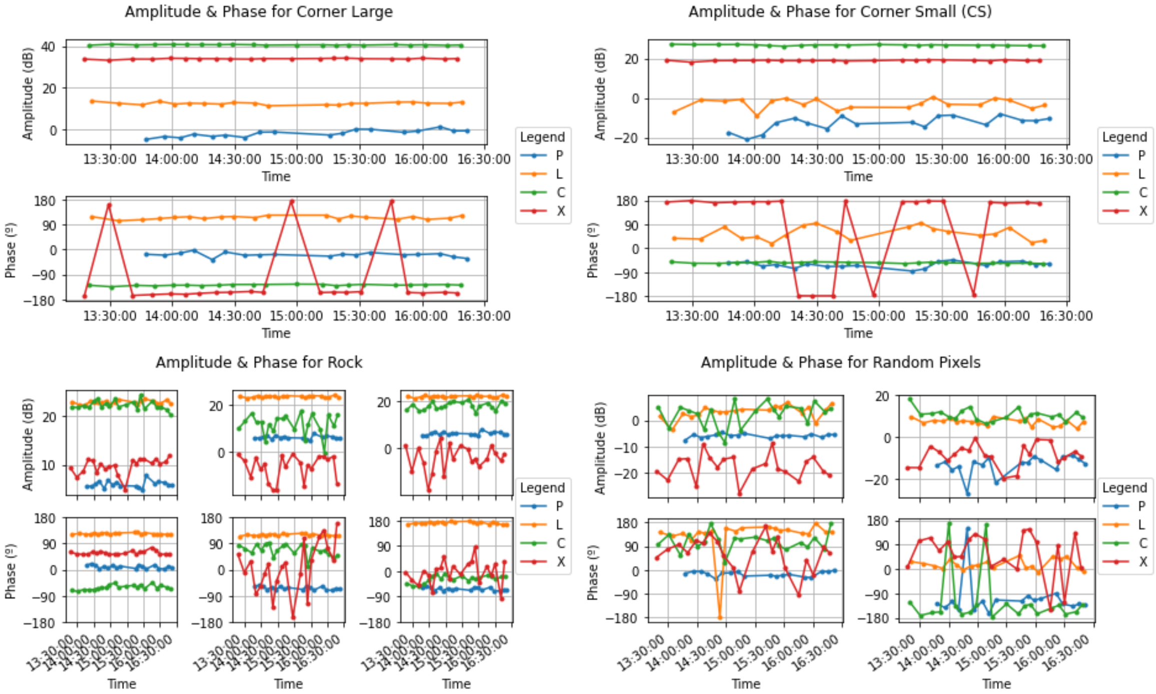

Figure 5.1: Reflector Amplitude & Phase Temporal Evolution. Internal Calibration

In X-band the results show how the amplitudes for the CL and CS are very stable and high value, which is a very good result as expected from a permanent scatterer. For the pixels corresponding to the ROCK the amplitudes shift from acquisition to acquisition. It is also interesting how on the first of the pixels from the ROCK the amplitude is much higher than in the other two, although it still shifts. The reasoning might be that the first pixel corresponds to a part of the ROCK not covered by vegetation whereas the other two pixels are covered. The phases deliver a more curious result. The jumps in phase higher than 180º are caused by the wrapping of the signal. For the CL the phase is located around -162º but there is some small phase instabilities caused by slow atmospheric effects such as changes in humidity and temperature. Three important peaks happen at the 2nd, 12th and 17th acquisitions and they deviate around 35º from the mean. They appear around 170º because of the wrapping of the image. This strong shifts in phase might be caused by strong and fast changes in the atmospheric conditions. This three strong shifts in phase are bad news and they are the reason for the moderate standard deviation of 11.7º. For the CS the phase is located around 176º but the same small phase instabilities appear. It is also interesting that on acquisitions 2, 12 and 17 some stronger shift in phase can be seen, although it is not as strong as in the CL, only around 9º from the mean. The standard deviation is low at 4.5º. The strong phase shifts are probably more noticeable in the CL because it is surrounded by vegetation, whereas the CS is not. The fast change in the atmospheric conditions, such as a breeze of wind, might have affected the vegetation surrounding the CL and thus shifting more the phase. For the ROCK the phase from the fist pixel is somewhat stable as it is probably not covered by vegetation. The phases for the other two pixels are highly unstable. Therefore, for the first pixel the standard deviation is a moderate 6.5º whereas for the other two pixels is a very high 84.2º and 41.5º respectively.

In C-band the results are somewhat similar to X-band. The amplitude is stable and high for the CL and CS but unstable for the ROCK. The amplitude is higher in this band than in X-band because the emitted power is higher. The phases for CL and CS are more stable than in X-band. The standard deviation is a low 2.2º for both TCRs. The mean phase for the CL is -128.5º and for the CS is -54.7º. They are still affected by some minor instabilities caused by slow atmospheric effects but no big shifts in phase appear, the biggest shift for the CL is 6º and for the CS is 4.8º. The phases for the pixels of ROCK are still unstable but they shift less than in X-band. The standard deviations for each pixel are high at 8º, 20.1º and 12.9º respectively. In general we could say that at C-band the results are more stable than in X-band because of the increased power and the slight increase in penetration.

In L-band the results are quite different from the previous bands. The CL has a moderate and stable amplitude. The phase is around 116.2º can be considered stable with some small shifts that go up to 11.6º from the mean. The standard deviation is a low 5.6º. The CS has a low and varying amplitude and a shifting phase. For the phase the standard deviation is 24º, high value. This confirms what was said previously that in L-band the CL is visible but the CS is not. The ROCK provides a stable and similar result on the three pixels. The standard deviation in the selected pixels are 2.6º, 3º and 3.8º respectively, all low values. Which confirms the fact that the wave is penetrating the vegetation covering the ROCK.

In P-band the results are the expected ones. For the CL and CS the amplitude is very low and the phase is unstable with a moderate standard deviation of 7.7º and 10.8º for each TCR respectively. The TCRs are not visible in this band. For the ROCK the results are on the contrary. The same result is seen on the three pixels selected as ROCK. The amplitude is moderate with some minor shifts. The phase has some shifts up to 10º so it is not as stable as in L-band. The standard deviations are a bit higher at 5.7º, 5.4º and 5º respectively for every pixel. In general we could say that at P-band the results are less stable than in L-band. The reflected amplitude is lower and the lower spatial resolution might mean that more clutter is inside each pixel.

Band	Pixel	Mean phase (º)	Max phase (º)	Min phase (º)	Max shift (º) w.r.t. Mean	Standard Deviation (º)
X	***CL***	-162.084	-151.860	-197.253	35.169	11.711
	CS	176.182	185.656	168.305	9.473	4.476
	ROCK 1	57.871	76.699	51.399	18.828	6.494
	ROCK 2	7.536	158.493	-162.732	170.268	84.248
	ROCK 3	-2.344	87.299	-96.404	-96.404	41.564
C	***CL***	-128.460	-125.180	-134.506	6.046	2.200
	CS	-54.737	-49.909	-57.945	4.828	2.267
	ROCK 1	-60.687	-43.565	-75.166	17.122	8.074
	ROCK 2	67.066	93.546	10.483	56.583	20.136
	ROCK 3	-26.646	-7.731	-54.722	28.076	12.952
L	***CL***	116.217	124.924	104.565	11.652	5.628
	CS	55.585	95.661	17.444	40.077	24.025
	ROCK 1	124.446	129.262	120.546	4.815	2.583
	ROCK 2	119.882	125.064	114.869	5.182	3.028
	ROCK 3	172.191	178.085	165.640	6.550	3.854
P	***CL***	-18.596	-2.345	-36.252	17.656	7.719
	CS	-62.063	-44.216	-85.983	23.920	10.814
	ROCK 1	10.163	20.496	1.697	10.332	5.764
	ROCK 2	-63.094	-53.325	-71.530	9.769	5.452
	ROCK 3	-62.837	-53.760	-69.850	9.078	5.035

Table 5.1: Phase Stability Statistics. Internal Calibration (unwrapped phases)

Finally, we will end with the images Externally Calibrated. As said in a previous chapter, each individual image is calibrated with respect to a reference pixel located in the image. For X and C-band the reference pixel is the CS as the shifts in phase are lower than in CL. For L and P-band the reference pixel is the second pixel of the three selected as ROCK. As a result of this calibration, the temporal evolution of the reference pixels does not provide any information. These pixels are the reference of the whole image and as a result their amplitude and phase are always 0.

Below, in Figure 5.2, are shown the plots of the temporal evolution for the amplitude in dB and the phase in degrees for the selected pixels at each band. Also in Table 5.2 are shown some statistical values about the stability of the phases of the selected pixels. To compute the statistical values the phases for the pixels 2 and 3 corresponding to the ROCK in X-band have been unwrapped.

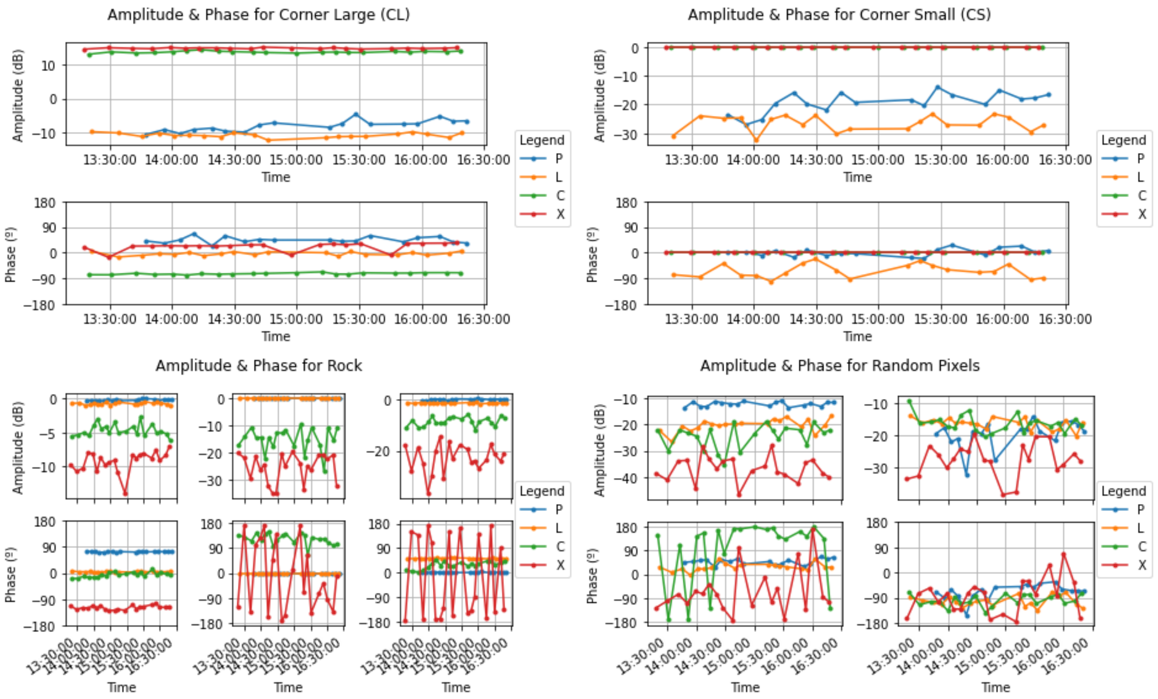

Figure 5.2: Reflector Amplitude & Phase Temporal Evolution. External Calibration

In X-band the results show the amplitude for the CL is stable and as expected it is around 15 dB higher than the amplitude in the CS. The phase is also stable around 21.7º but the big shifts in acquisitions 2, 12 and 17 appear. This confirms that the big shifts are stronger in the CL than in the CS, if the shifts were equal in both TCRs the line would be straight. The maximum shift from the mean is 38.1º. Apart from this big shifts the phase is straight, as the small shifts caused by slow atmospheric effects are compensated by the calibration. A small slope on the line can be perceived. This slope might be caused by changes in atmospheric artefacts such as the refractive index. The standard deviation is high at 14.1º because of the strong shifts in the mentioned acquisitions. For the ROCK, like in the Internal Calibration, one of the pixels is somewhat stable with a moderate standard deviation of 6.6º, but the other two jump all over the place with very high standard deviations of 86.4º and 41º on the phase.

In C-band the results are stable. For the CL the amplitude is stable and higher, around 14 dB, than in the CS. The phase is very stable, almost a straight line, as no big shifts appear in this band. The maximum shift with respect to the mean is 5.9º and the standard deviation is a low 2.9º. Also a slope can be perceived on the line, but it is smaller than in X-band. This slope is what prevents the maximum shift and standard deviation of being even lower. For the ROCK the result is the same, somewhat stable one pixel with a standard deviation of 8.3º and unstable the other two pixels with standard deviations of 20º and 12.9º respectively.

In L-band the results are the expected ones. For the CL the amplitude is stable although around 10 dB lower than the in the referenced pixel. The phase generally is stable but some minor phase shifts up to 11.6º appear. The standard deviation is a moderate/low 6º. For the CS both amplitude and phase shift on every acquisition. The standard deviation for the phase is a high 23.2º. For the ROCK the results are very stable. The second of the pixels is the reference. The other two pixels have a very similar and constant amplitude and a stable phase. The maximum shift with respect to the mean is 1.9º for the first pixel and 2.7º for the third pixel. The standard deviations are very low at 0.8º and 1.2º respectively.

In P-band the results are similar to the previous band. The CL and CS are both unstable as amplitude and phase shift with every acquisition. The standard deviation for the phase is high at 10.5º and 13.2º for each TCR respectively. For the ROCK the results are very stable. The second pixel is the reference for calibration. The other two pixels also have constant amplitudes and stable phases. The maximum shift and standard deviations are very similar to the previous band. The shift is 1.8º and 3.1º while the deviation is 0.8º and 1.1º respectively.

Band	**Pixel**	**Mean phase (º)**	**Max phase (º)**	**Min phase (º)**	**Max shift (º) w.r.t. Mean**	**Standard Deviation (º)**
X	***CL***	21.733	34.408	-16.377	38.110	14.130
	CS	0.000	0.000	0.000	0.000	0.000

X	***ROCK 1***	-118.311	-104.824	-129.358	13.487	6.650
	ROCK 2	-168.646	-9.812	-346.732	178.085	86.359
	ROCK 3	-178.527	-89.902	-267.989	89.462	41.064
C	***CL***	-73.724	-67.796	-79.003	5.927	2.942
	CS	0.000	0.000	0.000	0.000	0.000
	ROCK 1	-5.950	13.488	-19.136	19.438	8.263
	ROCK 2	121.803	149.666	63.029	58.774	19.994
	ROCK 3	28.091	48.390	2.431	25.661	12.903
L	***CL***	-3.665	6.311	-15.322	11.658	6.087
	CS	-64.297	-22.354	-101.141	41.943	23.224
	ROCK 1	4.564	6.525	3.024	1.961	0.835
	ROCK 2	0.000	0.000	0.000	0.000	0.000
	ROCK 3	52.309	54.457	49.546	2.763	1.181
P	***CL***	44.498	66.314	23.797	21.816	10.552
	CS	1.030	26.441	-20.756	25.411	13.252
	ROCK 1	73.257	74.462	71.399	1.858	0.813
	ROCK 2	0.000	0.000	0.000	0.000	0.000
	ROCK 3	0.256	3.393	-1.189	3.137	1.087

Table 5.2: Phase Stability Statistics. External Calibration (unwrapped phases)

To summarize everything said in this section. The Corner Large or CL, in X-band it could be very stable but some big phase shifts appear on some acquisitions that make it unstable, in C-band it is very stable, in L-band it is stable, and in P-band it is unstable. The Corner Small or CS, in X-band it could also be stable but the same strong phase shifts appear with less effect, in C-band it is very stable, in L and P-bands it is unstable. The ROCK, in X and C-bands it is somewhat stable if not covered by vegetation but unstable otherwise, in L and P-bands it is very stable as the wave penetrates the vegetation.

5.2. Differential Stability

We are now interested in observing in more detail the evolution in time of the acquisitions. We want to know how different each acquisition is from the first one, it is an Interferometric Analysis. To carry out this differential analysis the correlation between images is computed. The correlation between the first acquisition and the rest of the acquisitions for each band is used to obtain the results. The first acquisition in each band is used as the Master and the rest of the consequent acquisitions as Slaves. That means the correlation is calculated between the 1st and 2nd acquisition, between the 1st and 3rd acquisition, between the 1st and 4th acquisition, …, and so on for the rest of the acquisitions.

The correlation is defined as a statistical measure of how similar two signals are. In SAR images this corresponds to how similar a pixel is between two images. The higher the value the more similar or correlated the two pixels are. The phase of the correlation is used in InSAR to detect movements or deformations in the terrain. Being S_1 and S_2 two SAR images, their correlation image is computed as:

$$\rho = |\rho| \cdot e^{\varphi} = \frac{\langle S_1 \cdot \bar{S}_2 \rangle}{\sqrt{\langle |S_1|^2 \rangle \cdot \langle |S_2|^2 \rangle}}$$

Where: $|\rho|$ is the modulus of the correlation image, φ is the differential or interferometric phase of the correlation image, the “ ¯ “ is the conjugate operator, and the “ < > “ operator is the expected value operator. To execute the expected value operator a low-pass filter is used. The low-pass filter is a spatial domain linear filter that consists in the convolution between a matrix, usually a 3x3 or 5x5 uniform matrix, called kernel and the image.

For this study the externally calibrated images are used. As we want all images referenced to the same reflector at each band. For the correlation calculation a 3x3 low-pass filter is used instead of a 5x5 filter. This is because both procedures provide very similar results but the 3x3 filter is faster, around 20% less execution time, and requires less computing power. We are expecting to have very high correlation in the areas near the reflectors, both TCRs and the ROCK, and for the phase to be constant and close to zero in the reflectors.

5.2.1. Differential General Stability

The correlation is computed between the first acquisition and the rest of the acquisitions for each band. In this section the general full-image stability of the correlation is analysed. We are interested in the areas with a very high correlation value, as that means the area is similar between images. Because of that low correlation pixels are ignored.

The following figures correspond to the pixels with a correlation modulus higher than 0,8 in all the correlations computed at each band. The rest of figures and plots mentioned are visible in the Appendices Section 2.2.1.

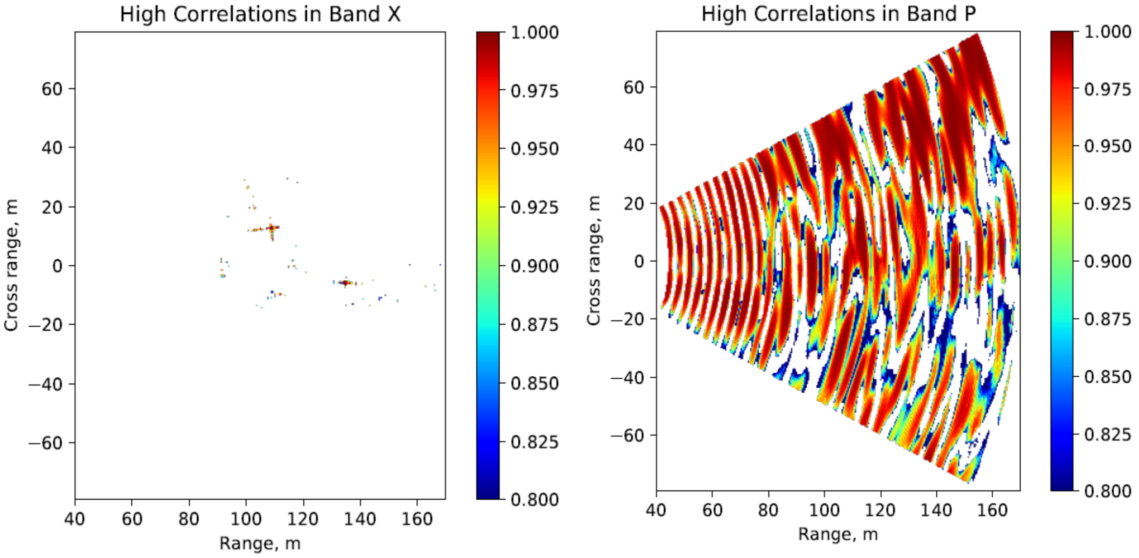

Figure 5.3: Pixels with High Correlation in X-band & P-band

At each band the highly correlated areas are different. As a general observation, there are more areas the lower the band is. The reasoning behind is that at lower frequencies the penetration increases and as a result the system receives the waves reflected inside the vegetation or even the soil below, which is a much more stable target than the outer foliage. At X-band the only areas with a very high correlation are the two TCRs with their secondary lobes, some pixels in the area of the ROCK that correspond to non covered areas of the natural reflector, and some disperse pixels than can be identified as the road. At C-band the same areas are present, the road is much more noticeable. More pixels appear scattered around the image. At L-band the area below the road shows areas with high correlation in addition to the ROCK. Some pixels with very high correlation appear in the area of the CL. At P-band much of the image shows high correlation because of the high vegetation penetration, the ROCK is clearly visible.

5.2.2. Differential Temporal Stability

After looking into the areas with a high correlation modulus in all the bands, we will focus in studying the evolution of the modulus and the phase of the computed correlations for specific pixels. The ideal result would be a constant high modulus and a constant zero value phase. As in section 5.1. the selected pixels of study are the CL, the CS and the same three pixels selected from the ROCK. The correlations are computed between the first acquisition and the rest of the acquisitions, therefore this study can be understood as a the temporal evolution of the difference between acquisitions.

The following figures show the evolution for the modulus and the phase of the correlation between the first and the next acquisitions in the selected pixels. The figures and plots mentioned are more visible in the Appendices Section 2.2.2. As the images are externally calibrated, the graphs corresponding to the reference calibrators provide little information. Below there is also Table 5.4 where the mean value and the standard deviation for the correlation phase in the reflectors are shown.

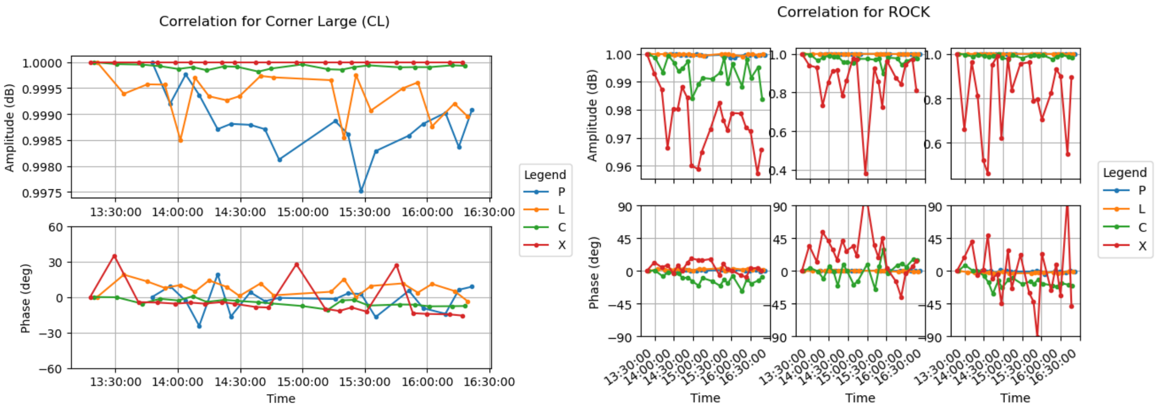

Figure 5.4: Correlation Temporal Evolution for CL and ROCK in all Bands

In X-band the results show that for the CL the modulus is almost perfect around 1, which means unbelievably high similarity in this area between all the images. It is in the phase were the interest lies again. The big phase shifts caused by a strong and fast change in atmospheric conditions appear again in acquisitions number 2, 12 and 17. Because of these shifts the standard deviation has a high value of 14.13º. In addition to this big shifts, it can be observed that the phase tends to a slow decrease with every acquisition. This decrease lowers the mean to -3º. The evolution can be adjusted to a sloped line. This decrease is the same slope noticed in section 5.1, caused by changes in atmospheric artefacts such as the refractive index of the medium. For the CS everything is null as it is used as the reference in the calibration. For the ROCK, the pixel that corresponds to a non-covered by vegetation area the modulus is high and the phase does not have big shifts, the standard deviation is a moderate 7.5º. The other two pixels have a varying modulus and unstable phase, the standard deviation is 28.7º and 40.2º respectively. The varying modulus means it changes on every acquisition and the high deviation means it is not stable..

In C-band the results are quite similar to the previous band. For the CL the modulus is also extremely high with some insignificant variances. The phase does not have the big shifts the previous band had but there are some minor variances between correlations. Thus the standard deviation is a low 2.9º. Although it is not as linear as the previous band, the graph can be adjusted to a sloped line. The slope is smaller than in X-band, which confirms that the changes in the refractive index have a bigger effect on the phase the higher the frequency is. For the CS everything is null as it is used as the reference in the calibration. For the ROCK the results are similar to X-band, the modulus is less variable and higher in general and the phase is less variable, as confirmed by the lower standard deviations of 7.1º, 12.9º and 9º for each pixel corresponding to the ROCK.

Instead, in L-band the results show a different behaviour than the previous bands. For the CL the modulus is variable but it has an extremely high value. The phase shifts a bit, the deviation is a moderate 5.8º, and it does not seem to be adjustable by a sloped straight line. For the CS the modulus is quite unstable but with a high value, which is a surprise since it is not clearly visible in the images. On the contrary the phase shifts a lot. The standard deviation is 19.6º, it is unstable. For the ROCK the second pixel is null as it is used as the reference in the calibration. The first pixel has a high modulus with minor variations and a stable phase at 0 degrees. The third pixel has a higher perfect modulus, around 1, and a stable phase at 0 degrees. Both pixels have very low standard deviations of around 0.9º.

In P-band the results are similar to L-band. For both the CL and CS the modulus is high but variable, the phase shifts constantly with standard deviations of 10.6º and 13.3º respectively. For the ROCK we can extract the same conclusions as in L-band.

The correlation phase or interferometric phase for the CL in X and C-band can be adjusted by a sloped straight line. It is possible to obtain this line by using linear regression. The linear regression provides a polynomial that best fits the data. The success of the fitting is measured by the R^2 score, 1 meaning perfect fitting and 0 meaning null fitting. As we require a straight line, we get a polynomial of degree one defined as: $p(x) = b_1 \cdot x + b_0$

For X-band, if we consider all acquisitions the R^2 score obtained is 0.11. The big shifts on acquisitions number 2, 12 and 17 corrupt the regression and thus the polynomial does not fit. For this reason these three acquisitions are omitted in this calculation. For C-band all acquisitions are considered.

Band	Polynomial that fits the data	R^2
X	$p_X(x) = -0.801 \cdot x - 1.709$	0.92
C	$p_C(x) = -0.349 \cdot x - 1.073$	0.505

Table 5.3: Linear Regression to adjust the Interferometric Phase for CL in Bands X/C

For X-band, the high score means that if were not for those three acquisitions, the phase drift would fit very well a straight line. For C-band, the moderate score means the phase drift is not constant between acquisitions. This drift is caused by the changes in the refractive index of the air between acquisitions. This drift is dependent on the range and the frequency. The furthest the target is or the higher the frequency, the drift caused by the refractive index is higher. Fortunately this drift in the interferometric phase can be compensated by applying an atmospheric artefacts compensation technique as described in Luca Pipia Ph. D. dissertation.

Band	Reflector	Mean (º)	Standard Deviation (º)
X	***CL***	-3.015	14.130
	CS	0.0	0.0
	ROCK 1	4.909	7.469
	ROCK 2	23.212	28.733
	ROCK 3	-3.939	40.258
C	***CL***	-4.566	2.977
	CS	-0.043	0.188
	ROCK 1	-10.845	7.141
	ROCK 2	1.086	12.870
	ROCK 3	-13.479	8.983
L	***CL***	7.388	5.798
	CS	-2.690	19.641
	ROCK 1	1.971	0.935
	ROCK 2	-0.142	0.394
	ROCK 3	-2.094	0.897
P	***CL***	-1.785	10.655
	CS	-0.576	13.280
	ROCK 1	0.661	0.706
	ROCK 2	0.192	0.196
	ROCK 3	-0.758	1.200

Table 5.4: Interferometric Phase Mean & Standard Deviation

Finally, to validate the precision of the differential phases of the computed correlations a basic subtraction is computed between the externally calibrated images. For the same pixels studied in the previous section, the difference between the phase in the first acquisition and the other acquisitions is computed.

As it can be observed from the graphs in the Appendices Section 2.2.2, the lines follow an almost identical evolution for all bands in all the selected pixels as in the plots previously shown. The values are slightly higher because the low-pass filter used in the correlation calculation has a smoothing effect that averages the values of the pixels. The variances and shifts described in the differential analysis are accurate and not a product of the computation of the correlation.

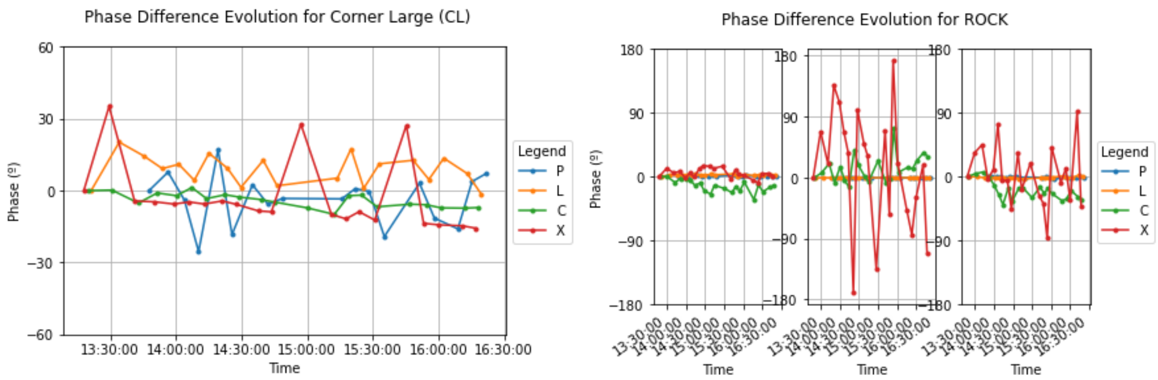

Figure 5.5: Phase Difference between 1st and rest of acquisitions. CL & Rock

5.3. Summary of Stability

In this section a summary of all the Stability Study is given. Each band is discussed and summarized individually.

In X-band at first glance the images appear stable. For both TCRs the amplitude is high and constant. Unfortunately, the phase cannot be considered completely stable. In acquisitions number 2, 12 and 17 a big shift appears. It might be caused by a fast and strong change in the atmospheric conditions, for example a breeze of wind. This possible breeze has a bigger effect in the CL than in the CS because the first one is completely surrounded by vegetation. Some other small atmospheric effects appear but they can be compensated with external calibration. A drift in the phase is observed in the differential temporal study with the correlations. It is caused by the change in the refractive index of the medium but it can be compensated by applying an atmospheric artefacts compensation technique. For the ROCK there is not much to say. Few parts of it are uncovered by vegetation and therefore visible, but in general it is a non stable target because of the vegetation. To sum up, we cannot consider the images at X-band stable because both of the artificial reflectors, which are used as calibrators, are affected by strong phase instabilities.

In C-band the images are more stable than in X-band. For both TCRs the amplitude is high and constant. The phase suffers from some small instabilities caused by small atmospheric effects that can be partially compensated with external calibration. A small drift in the phase caused by the change in the refractive index appears but it can be compensated by applying an atmospheric artefacts compensation technique. The ROCK cannot be considered a stable target as it is mostly covered by vegetation and thus invisible to this band. To sum up, we can consider the images at C-band stable. Both artificial reflectors can be used as calibrators as the phase instabilities can be mostly compensated.

In L-band the images are different from the previous bands. The CL is visible with a moderate amplitude and somewhat stable phase, as the resolution is lower and there is more clutter inside the pixel. On the contrary, the CS is not visible. As a result the CL can be considered a mildly stable target but the CS is unstable. The ROCK is at this band clearly visible through the vegetation. The amplitudes and phases have some minor instabilities that are compensated by external calibration. In consequence the ROCK is a stable target. To sum up, we can consider the images at L-band stable. Both the CL and the ROCK can be used as calibrators although the ROCK provides the less variances.

In P-band the images are similar to L-band. Neither of the artificial reflectors, the CL and CS, are visible and therefore cannot be considered stables. The ROCK is very clearly visible at this band through the vegetation. The amplitude is constant and the phase is stable after the external calibration. To sum up, we can consider the images at P-band stable. The ROCK can be used as a natural reflector and as a calibrator.

6. Probability Model Analysis

The Probability Model Analysis consists in studying the different Probability Models that best describe and fit the statistical behaviour of the data obtained from the radar. This Probability Analysis is usually used in aerial and spatial SARs for classification purposes. We will use it to extract some new information about the data obtained and to verify some of the ideas extracted from the Stability Analysis.

In this chapter some probability models are described and then compared with the data to extract the conclusions. At the end the parameters used in the probability models are studied to search for the same instabilities described in the Stability Analysis.

All figures and plots mentioned are visible with greater detail in the Appendices Section 3.

6.1. Probability Models in SAR Images

Even though the idea behind SAR is simple, lots of different probability models for the estimation of the Probability Density Function or PDF of the data have been developed throughout the years. Each probability model is fitted for a different purpose or for a specific situation in the image. Also there are various levels of complexity and generalization between the different models.

The basic model behind all SAR information is the Speckle phenomena. The Speckle is based on the high ratio between the spatial resolution and the wavelength of the signal. If the number of scatterers or reflectors in the resolution cell is very big, ideally infinite, then the Central Limit Theorem can be applied. This theorem states that if the number of independent random variables is high enough, their addition tends to a normal distribution. In the case of SAR, this addition makes the scattering a noise-like random process. If the theorem is fulfilled, the real and imaginary parts of the backscattered signal are independent zero-mean Gaussian random variables. Because of that, the signal intensity follows an Exponential distribution and the signal amplitude follows a Rayleigh distribution. The phase is uniformly distributed in $[0,2\pi]$. This case is referred as fully developed speckle. When the theorem is not fulfilled and not many scatterers are present, it is referred as partially developed speckle and much more complex statistical distributions are required.

As the data from the GB-SAR is amplitude and phase, considering the speckle is fully developed, the Rayleigh distribution will be studied. A Rayleigh distribution is a continuous probability distribution for non-negative random variables. The PDF is:

$$f(x,\sigma)=\frac{x}{\sigma^2}\cdot e^{-\frac{x^2}{2\cdot\sigma^2}} \quad , \qquad \forall x\geq 0$$

Where σ^2 is the scale parameter of the distribution. This parameter can be estimated using a Maximum Likelihood Estimator or MLE. This estimator is unbiased. If N is the number of independent and identically distributed Rayleigh random variables x_i , the estimator is defined as:

$$\hat{\sigma}^2=\frac{1}{2N}\cdot\sum_{i=1}^{N} x_i^2$$

The problem is that real SAR data does not always follow the theoretical distributions, thus some more accurate PDF are required. Various statistical models have been developed to better fit the different typologies of SAR data. One of those models is the Nakagami distribution. This distribution was proposed to model the statistical behaviour of SAR data in the presence of a single strong reflector in a homogeneous clutter. A Nakagami distribution is a probability distribution related to the Gamma distribution. The PDF for the amplitude is:

$$f(x;m,\Omega)=\frac{2\cdot m^m}{\Gamma(m)\cdot\Omega^m}\cdot x^{2m-1}\cdot e^{-\frac{m}{\Omega}\cdot x^2} \quad , \quad \forall x\geq 0$$

Where Γ(·) is the standard Gamma function, *m* is the shape parameter and *Ω* is the spread parameter. These two parameters can be estimated. The basis of this estimators is the kth sample moment. If there are N random variables x_i , their kth sample moment is defined as:

$$\mu_k=\frac{1}{N}\cdot\sum_{i=1}^{N} x_i^k$$

The spread parameter estimator is defined as the 2nd sample moment and it is an unbiased estimator. The shape parameter can be estimated by an Inverse Normalized Variance estimator (INV). For small values of N it is unbiased. The estimators are defined as:

$$\hat{\Omega}=\mu_2=\frac{1}{N}\cdot\sum_{i=1}^{N} x_i^2$$

$$\hat{m}=\frac{\mu_2^2}{\mu_4-\mu_2^2}=\frac{\left(\frac{1}{N}\cdot\sum_{i=1}^{N} x_i^2\right)^2}{\frac{1}{N}\cdot\sum_{i=1}^{N} x_i^4-\left(\frac{1}{N}\cdot\sum_{i=1}^{N} x_i^2\right)^2}$$

Other probability models are the “heavy-tailed” Rayleigh distribution, the K distribution and the Inverse Gaussian (IG), between many others. The problem with this other statistical models is that their implementation and parameter estimation is immensely more complex and costly.

6.2. Probability Models & Histograms

To study the probability model of the GB-SAR images we will make use of histograms. A histogram is the representation of the distribution of numerical data, with the height being proportional to the frequency a value appears. By using a histogram it is possible to compare the amplitude values from the GB-SAR images to a specific probability model and to compare the phase values to a uniform distribution.

The histograms are built using the data from all the acquisition at each band. All the images are counted in the histograms. The GB-SAR images are only internally calibrated. We want to have the internal gains and shifts compensated but we do not want to have the images referenced to a calibrator. The pixels between the ranges of 40 meters and 80 meters are ignored in this study as they correspond to the shadowed area below the radar that is captured by the side-lobes of the antenna.

6.2.1. Complete Images

In this section the amplitude histograms for the full images, except for the shadowed areas below the sensor, are compared to the theoretical Rayleigh and Nakagami distribution models. The phase histograms for the full images are also discussed.

The figures for all histograms and statistical models are visible with detail in the Appendices Section 3.1.1. Here only four figures are shown.

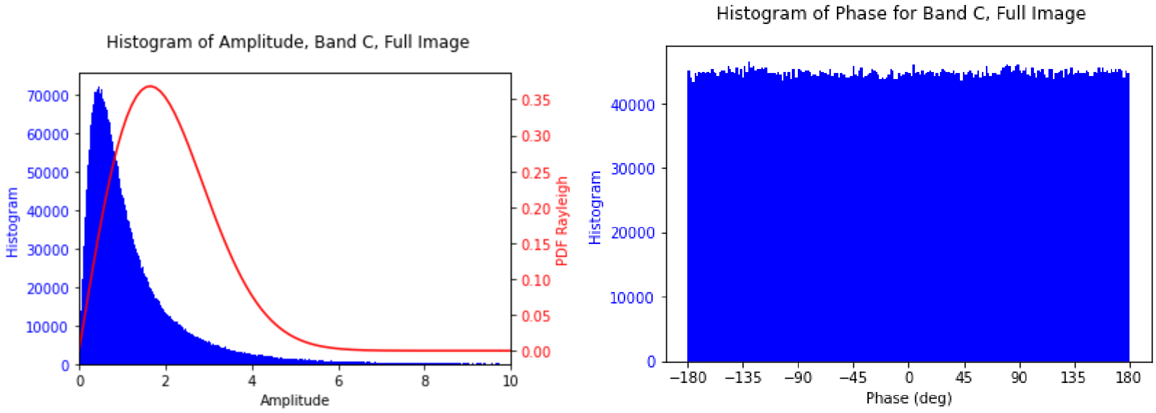

Figure 6.1: Amplitude & Phase Histogram with Rayleigh PDF. Full Image in C-band

In X-band, C-band and L-band the results are pretty similar. The majority of the pixels have a very low amplitude. The histograms are cropped to show only the amplitudes below 4, 10 and 10 in X, C and L-band respectively. It is cropped because almost all the pixels fall inside these small intervals and it provides a better look into how the probability models fit the amplitude histogram. About the probability models neither of them fit the amplitude histogram. For the C and L-band the Rayleigh distribution have a similar shape to the amplitude histogram but they do not fit. Because of these results, we can conclude that at X, C and L-band the real GB-SAR data, when considering the complete image, likely follows a more complex amplitude distribution. The phase histogram is very similar in the three bands. It is clearly uniformly distributed in bands X and C, which means the speckle is fully developed and the Central Limit Theorem is fulfilled. In L-band it is still quite uniformly distributed although not as constant as the previous bands. We can consider the speckle as almost fully developed in L-band.

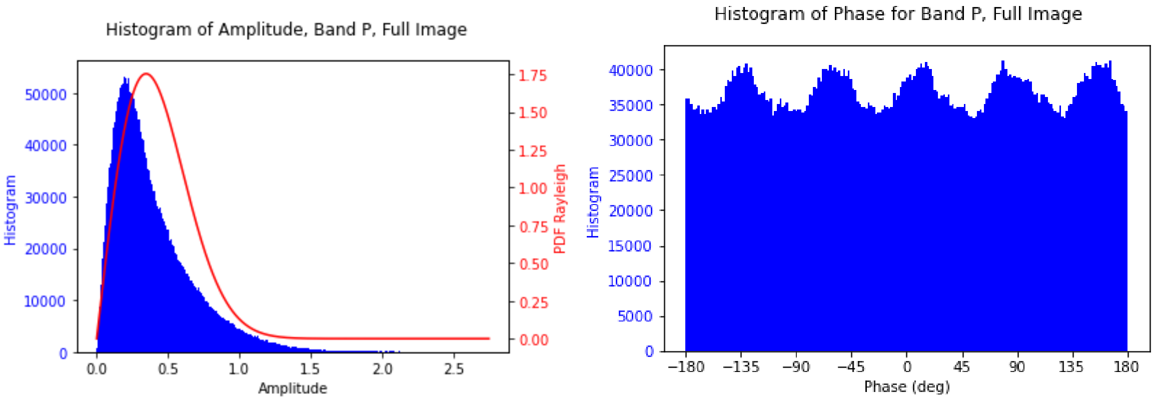

Figure 6.2: Amplitude & Phase Histogram with Rayleigh PDF. Full Image in P-band

In P-band the results are a bit different. The amplitude histogram is mainly congregated in the lower values, although it less concentrated than the previous bands. This histogram is not cropped. About the probability models, the Rayleigh distribution is quite similar but it does not fit the histogram, the Nakagami does not fit at all. On the phase histogram the result is interesting, it is not uniformly distributed. It has a sinusoidal-like oscillating shape. This means the Central Limit Theorem is not fulfilled and thus the speckle is partially developed.

To summarize the most important results from this section, in X, C and L-band the speckle is fully developed whereas in P-band it is partially developed. This means that in P-band there are not many scatterers inside each resolution cell and in consequence the Central Limit Theorem is not fulfilled. The amplitude histograms do not fit either Rayleigh nor Nakagami distributions, but the Rayleigh has a much closer shape. They follow a more complex distribution.

6.2.2. Close up to the Reference Points

In this section only the pixels inside a window centred in the reference targets are compared to the Nakagami distribution. As before, all images at each band are considered for the creation of the histograms. The reference targets are the CL, the CS and the ROCK. For the TCRs the central pixel is used as a reference, whereas for the ROCK the second of the three pixels described in previous chapters is used as reference. Only the Nakagami distribution is analysed because it models a single strong reflector surrounded by clutter, which is the situation we want to simulate by selecting a window close to the reflector. Two different sized windows have been analysed, a big one with sizes 10x10 pixels in C, L and P-bands and 14x14 pixels in X band., and a small one with size 5x5 pixels in all bands. The big window is to observe the reflector and the area surrounding it, the difference in sizes for the window between bands is there to zoom into a similarly sized area in all bands, as the images in X-band have around three times more pixels than the other bands. The small window is to observe only the reflector and its vicinity. We want to observe very narrow distributions corresponding to the windows which means the targets are visible.

The figures for all reflectors and window sizes in all band are visible with detail in the Appendices Section 3.1.2. Here only four of the figures are shown below.

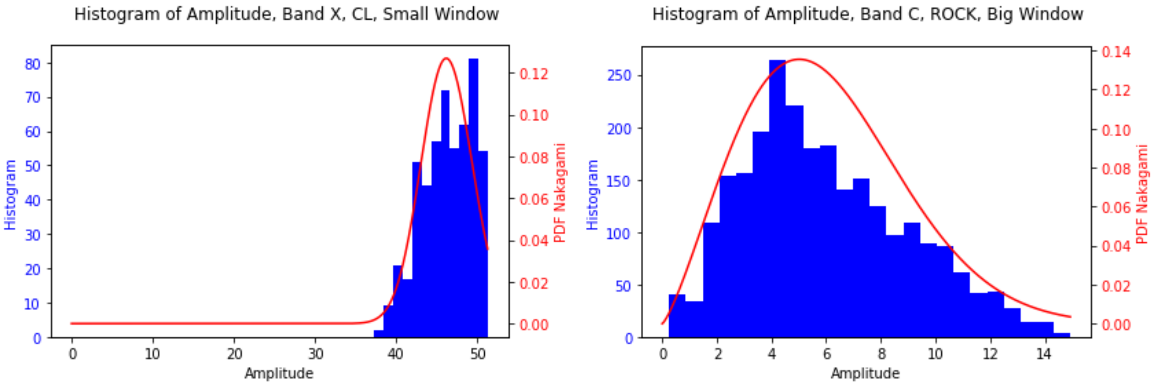

Figure 6.3: Ampl. Histograms & Nakagami PDFs. CL in X-band & ROCK in C-band

In X-band both CL and CS are visible and the ROCK is mostly covered by vegetation. For the CL, when using the big window the Nakagami distribution wraps nicely around the amplitude histogram. The histogram is centred around a medium-high value, which makes sense as the pixels surrounding the reflector are affected by its secondary lobes. When using the small window the PDF fits better the histogram, which is narrow and centred at the high values. This is a prime example of a Nakagami distribution, a single strong reflector surrounded by clutter. For the CS the results are very similar although the distribution does not fit as perfectly as before. For the ROCK both windows provide similar results, which makes sense as this target is not defined by a single pixel like the TCRs are and thus the variations between consecutive pixels are less steep. The PDFs fit the amplitude histogram which is wide and centred in the low values, meaning the target is not visible.

In C-band very similar conclusions can be extracted from the results. For the CL and CS, when using the big window the distribution does not fit as perfectly to the histogram, but when using the small window they fit very well. The big window provides an amplitude histogram centred in the medium values while the small window provides narrow histograms centred in the high values. For the ROCK both windows provide similar results. The distribution fits the histogram, which is wide and centred in low values, meaning the target is not visible.

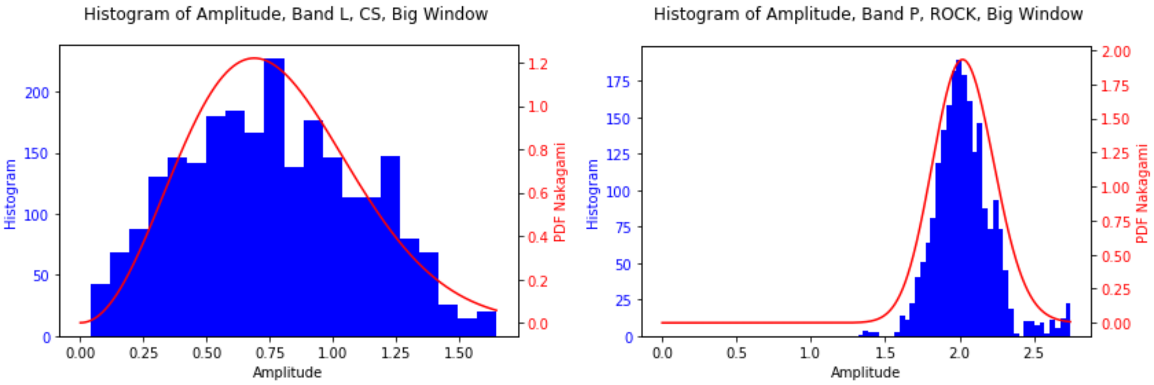

Figure 6.4: Ampl. Histograms & Nakagami PDFs. CS in L-band & ROCK in P-band

In L-band the results change a little bit. For the CL, when using the big window the distribution does not quite fit the amplitude histogram. But when using the small window it fits tightly around the narrow histogram. In both cases it is centred in high values. This reflector is visible at this band. For the CS we get the opposite result. For both windows the histogram is wide and centred in low values. Although the distribution fits the histogram, this target is not visible. For the ROCK, when using the big window the distribution fits quite well to the histogram which is centred in medium-high values. When using the small window the PDF fits perfectly the narrow histogram. The ROCK is visible at this band.

In P-band the results are as expected. For the CL and CS, for both window sizes the amplitude histograms are wide and centred in the very low values. The TCRs are not visible at this band. On the contrary we have the ROCK. For both windows the histogram is narrow and centred in the high values. The distribution fits nicely around both the histograms. The ROCK is visible at this band.

About the phase histograms not many conclusions can be extracted. In general, when a reflector is visible and their amplitude histogram is narrow, the phases are less variable and are stored in a reduced number of bins in the histogram, they are concentrated in a few values. When a reflector is not visible the phases are less concentrated in the histogram.

From this section we can confirm again which reflectors are visible at each band. Also, despite the fact that the speckle is partially developed in P-band, as discussed in the previous section, the ROCK is still seen as a strong reflector because of its large size. Even if there are not lots of scatterers in each resolution cell, as the ROCK corresponds to various pixels, it strongly reflects the waves at P-band.

6.3. Probability Parameters Temporal Evolution

In this section we will focus on the statistical distributions of the amplitude for each acquisition at each band. We are interested in seeing if there is any correlation between the statistical distributions for the amplitudes and some of the phase instabilities described in previous chapters. To do so on each acquisition a probability distribution is computed and their parameters plotted in a temporal order for each band. Also all distributions are shown in a single plot to observe the variability of the PDFs. As in the previous section, the GB-SAR data is internally calibrated to compensate all the internal gains of the system.

6.3.1. Complete Images

For the complete images of the scenery the same procedure is used. The shadowed area below the radar, ranging from 40 to 80 meters, is not considered for the computation. This is because the area provides little information as it has been captured by the side-lobes of the antenna. About the statistical distributions, in the previous section we observed that the Rayleigh distribution does not quite fit the amplitude histogram but it has a similar shape. The Nakagami distribution on the contrary does not fit at all the histograms. For this reason here only the Rayleigh distribution will be calculated. The Rayleigh distribution only has one scale parameter, the 'σ^2'. As in the previous section, the plots showing the distributions are cropped to show only the amplitudes below 10 in C and L-band and below 4 in X-band.

The figures for the PDFs and for the scale parameter evolution in all bands are visible with detail in the Appendices Section 3.2.1. Here only four of the figures are shown below. In general at all bands the distributions are quite similar between all acquisitions. There are some variances in the scale parameter between acquisitions. Below, in Table 6.1 is also shown the mean and the normalized standard deviation of the scale parameter at each band. The normalized standard deviation is used to better compare the bands with different means. In general the normalized standard deviation in all bands takes a very low value, which means there is not much variation in the scale parameter.

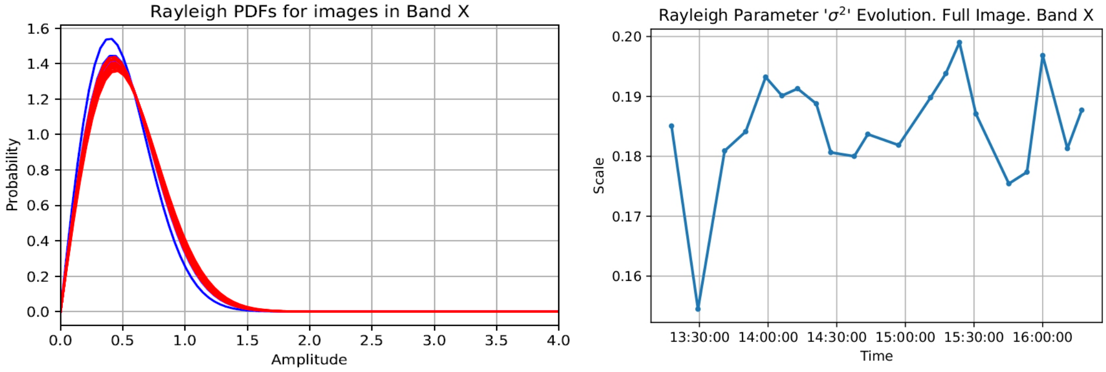

Figure 6.5: Rayleigh PDFs & Rayleigh Parameter Evolution. Full Images in X-band

In X-band one of the distributions is clearly different from the other twenty. When looking at the parameter evolution, we observe that the second acquisition has a much lower value for ‘σ^2’ than the rest. The second acquisition follows a distinguishable distribution. If we remember from previous chapters, in X-band a strong phase shift appeared in some of the acquisitions, being the number 2, 12 and 17. The second acquisition, where the phase shifts strongly, has a different distribution from the other acquisitions. Unfortunately, for acquisitions number 12 and 17 the distribution is not distinguishable from the others. In the figure the distributions corresponding to this three mentioned acquisitions are plotted in colour blue to differentiate them from the rest.

In C-band and L-band all distributions are very similar. The parameter shift a bit between acquisitions but in the end all PDFs are similar. The only exception is in L-band for acquisition 19, were the parameter is lower than the rest and the function is a bit narrower. This does not correlate to any of the instabilities described in Chapter 5.

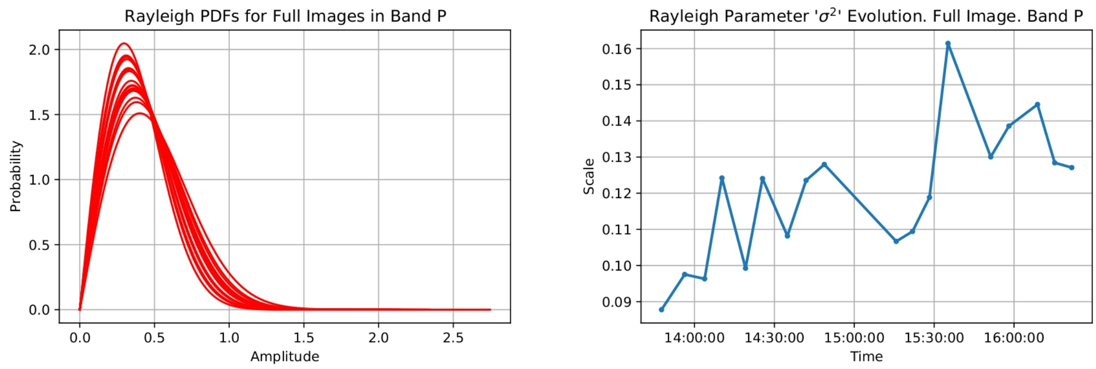

Figure 6.6: Rayleigh PDFs & Rayleigh Parameter Evolution. Full Images in P-band

In P-band some variances are seen between all acquisitions. The parameter evolution follows an increasing trend, which corresponds to the distributions being less narrow in latter acquisitions. This could suggest that in latter acquisition the amplitude of the pixels is slightly higher or more diverse. Further investigation is needed to explain the cause of this phenomena.

Band	**Mean of 'σ^2'**	**Normalized Standard Deviation of 'σ^2'**
X	0.185	0.049
C	2.708	0.036
L	1.103	0.038
P	0.120	0.015

Table 6.1: Rayleigh scale parameter σ^2 Mean & Norm. Std. Deviation. Full Image

6.3.2. Close up to the Reference Points

In this section the focus will be in the areas surrounding the reflectors. The reflectors are the same CL, CS and ROCK. To zoom into the reflectors a small window centred in the pixel corresponding to the reflector for the CL and CS is used. For the ROCK the second pixel of the three selected is defined as the centre of the window. The statistical model to study is the Nakagami distribution, as previously we have observed that it is a good fit for the amplitude histograms from the zoomed areas. In section 6.2.2 two different sized windows were used, here only the small 5x5 pixel window is used. The small window is used because, from the results of section 6.2.2, for this window generally the PDF fits more perfectly the amplitude histogram than for the big one. The Nakagami distribution is defined by two parameters, the 'm' shape parameter and the 'Ω' spread parameter.

The figures for all reflectors, both the PDFs and the parameters, in all band are visible with detail in the Appendices Section 3.2.2. Here only two of the figures are shown below. Also, below is Table 6.2, where the mean and the normalized standard deviation of both parameters is shown for all reflectors at all bands. The normalized standard deviation is used to better compare the results with different means.

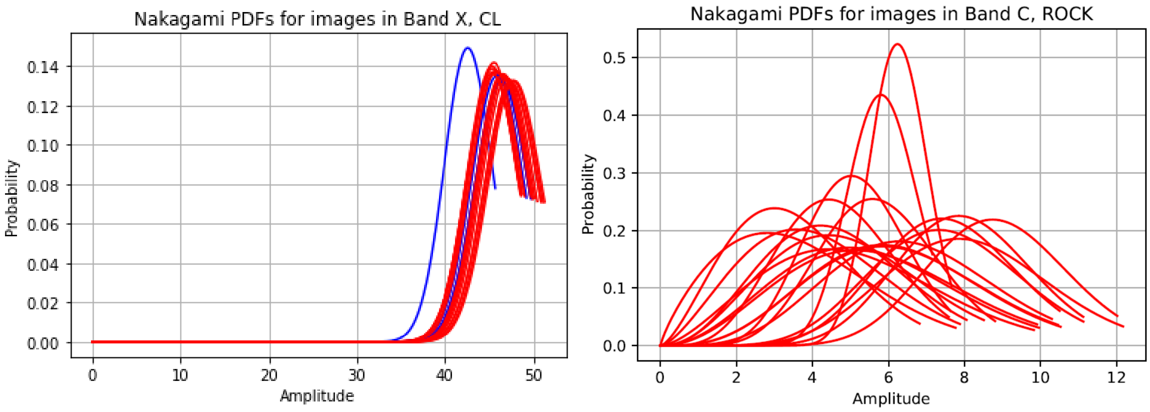

Figure 6.7: Nakagami PDFs. CL in X-band & ROCK in C-band

In X-band the results show that for both the CL and the CS all the distributions except one are quite similar. The different distribution corresponds to the second acquisition, which is one of the acquisitions affected by strong phase shifts in this band. The distributions are narrow which means the TCRs are visible in all the images. The high value for the mean value of ‘m’, being 62.3 and 94.6 for the CL and CS respectively, corroborates it. By observing the evolution of the parameters, the shape parameter varies quite a bit between acquisitions but it does not correlate to great changes in the distributions, as the normalized standard deviations for both parameters and reflectors are low. Moreover, the deviations for both parameters are higher in the CS than in the CL, which makes sense as the power scattered is lower in the CS. The spread parameter shows a very low value on the second acquisition, the different one. This change in the spread parameter is causing the different distribution for the second acquisition mentioned before. In the stability analysis, apart from the second acquisition, the acquisitions number 12 and 17 also had strong phase shifts. Unfortunately no much difference on the distribution nor in the parameters can be observed for those two special acquisitions, they are coloured in blue in the figures. For the ROCK the distributions for each image are a bit different from one another, but a pattern can be observed. The low mean of 0.98 for the shape parameter indicates the distributions are generally wide. The normalized standard deviations are moderate being 0.28 and 0.2 for shape and spread parameters respectively. All of this correlates to the idea that this reflector is not visible at this band and thus the distributions are quite wide in general and vary for every image.

In C-band the results are more clear. For both the CL and the CS all the distributions are quite similar. Although both statistical parameters vary a bit for each acquisition, the normalized standard deviations are low for both parameters, in the end the plotted PDFs are quite similar. The distributions are narrow, as expected from the high means of ‘m’, being 48.5 and 21 for the CL and CS respectively. This means the TCRs are visible in all the images. For the ROCK the distributions are very different from one another. The parameters vary a lot and therefore each PDF looks different from the others. The low mean of ‘m’ indicates the distributions are wide, but the high deviation of 0.993 means some are much more wider or narrower than others. This correlates to the idea that the ROCK is not visible at this band.

In L-band the results are a bit less clear. For the CL the distributions are a bit different but a pattern can be observed. They are narrow distributions centred around high values. The high mean value for ‘m’ of 42.2 confirms the pattern that the PDFs are narrow, but the moderate normalized deviation for ‘m’ of 0.27 explains the variances in the distributions. The spread parameter has a low normalized deviation of 0.135, which correlates to the distributions not being dispersed. Despite the variability, we can consider that the CL is visible because the PDFs are narrow and centred in high values. For the CS the opposite happens. The distributions are very different from each other. In general they are quite wide as the mean of ‘m’ is a low 7.7. But the normalized deviation for ‘m’ is very high at 0.997, which explains the high variability in the shapes of the different distributions. The moderate normalized deviation for the spread parameter of 0.4 explains the dispersion of the PDFs. This reflector is not visible. For the ROCK the distributions are less variable than for the CL. They are narrow and centred around a very high value. The high mean of ‘m’ at 94.6 and low normalized deviation of 0.1 indicates the PDFs are narrow. The low normalized deviation for the spread parameter at 0.07 means the distributions are concentrated. All of this correlates to the idea that the ROCK is visible at this band in all the images.

In P-band the results are more simple. For both the CL and CS the distributions vary a lot, which correlates to the reflectors not being visible at this band. The parameters vary a lot for both reflectors, but an increasing tendency can be observed in both parameters. This tendency is more clear for the CL. This changes in the parameters drift the distributions to higher values, which is the same phenomena seen for the complete images in the previous section. The normalized deviations for both parameters are moderate for the CL and high for the CS. For the ROCK the figure plotting all the distributions is not available because the parameters have such high values that the program is not able to compute the PDF. The shape parameter has a very high mean value, which means the distributions are narrow, but the high normalized deviation of 0.997 means some might be wider. The low deviation of 0.16 for the spread parameter means the PDFs are concentrated. In all, the ROCK is visible at this band.

Band	Reflector	Mean of ‘m’	Normalized Standard Deviation of ‘m’	Mean of ‘Ω’	Normalized Standard Deviation of ‘Ω’
X	***CL***	62.334	0.023	2152.116	0.048

X	***CS***	95.592	0.083	71.921	0.056
	ROCK	0.979	0.278	1.917	0.202
C	***CL***	48.462	0.029	10146.001	0.035
	CS	20.966	0.070	382.746	0.057
	ROCK	3.737	0.993	41.237	0.439
L	***CL***	42.232	0.273	16.807	0.135
	CS	7.731	0.997	0.693	0.421
	ROCK	94.588	0.115	198.059	0.074
P	***CL***	32.990	0.234	0.560	0.386
	CS	31.088	0.755	0.070	0.612
	ROCK	1046.220	0.997	4.413	0.164

Table 6.2: Nakagami parameters Mean & Norm. Std. Deviation. Zoom into Reflectors

As a summary of this section, we can say that the statistical analysis of each acquisition independently confirms again which reflectors are visible at each band. In each band, the reflectors that are visible have very similar and narrow Nakagami distributions concentrated in the high values of amplitude. When the reflector is not visible the distributions are different, in general are wide and dispersed.

In X-band a different distribution is obtained for the second acquisition, which probably means that whatever caused the big shifts in the phase also affected the probability distribution that models the amplitudes of the image. Unfortunately this cannot be confirmed as the other two acquisitions with strong phase shifts do not present such different statistical distribution for the amplitude.

Finally, in P-band there seems to be can increase in the value of the amplitudes for the latter acquisitions that was not perceived in the Stability Analysis. This supposed increase requires further investigation.

7. Conclusions and future development:

With all the results over the table the conclusions of this thesis can be presented. First of all, a summary of the studies and actions performed during this project is given. Following this the final results and conclusions of the thesis are presented. At the end, some future developments and works are mentioned.

The aim of this thesis is to study the efficiency of terrain displacement monitoring in an area covered with abundant vegetation with the use of a Multi-Frequency GB-SAR. Balamis has developed this GB-SAR that is able to capture at bands X, C, L and P. The data analysed in this thesis comes from a measurement campaign performed in the “Castell de Subirats” on June 2020. The measurement campaign consisted in capturing an area ranging from 40 m to 170 m South-West of the Castle. A road passes across the area of interest. Two artificial TCRs are placed in the area: a big one referred as Corner Large (CL) is placed above the road completely surrounded by vegetation, and a smaller one referred as Corner Small (CS) is placed next to the road. Apart from the artificial reflectors a big rock mostly covered by vegetation is present below the road and it is used as a natural reflector for lower bands. The study is divided into two separate studies. First the Stability Analysis studies the stability of the mentioned reflectors and assesses the computation and results of the differential interferograms. Then the Probability Model Analysis studies the statistical behaviour of the SAR images and tries to correlate it to the instabilities described in the previous study.

Let’s start with the Stability Analysis. Each reflector behaves differently in each frequency band. The images were studied after applying an internal calibration and after an external calibration. The results were quite similar for both calibrations but the external one had the advantage of compensating some of the atmospheric effects like changes in humidity and temperature. The reflector surrounded by vegetation, the CL, presented in X-band a strong phase shift in three of the acquisitions. The CS also presented a phase shift in the same acquisitions but not nearly as strong. This strong phase shift could have been caused by a fast atmospheric effect such as a breeze of wind that greatly affects the vegetation surrounding the CL causing the instability. In C-band it is very stable, which is probably caused by the increased power and the increase in the penetrating depth of the wave. In L-band it is somewhat stable and in P-band it is unstable as it is too small for this wavelength. The small reflector, the CS, suffers from the same shifts that affect the CL in X-band although the effect is not as strong. In C-band it is very stable but for L-band and P-band is unstable as it is too small for their respective wavelengths. The ROCK covered by vegetation is not visible in X-band and C-band, as the waves are not able to penetrate enough, thus it is unstable. On the contrary, in L-band and P-band the waves penetrate the vegetation and scatter on the bare rock. In this bands the ROCK is a very stable reflector.

The main focus of this analysis has to be the differential interferogram. The interferogram is the result of computing the correlation between two images at the same band. The first acquisition at each band is the Master image and the rest of the images are the Slaves. As there was no displacement in the reflectors between acquisitions, the interferogram should not have any phase shifts. In reality the results are not as idyllic. In X-band the strong phase shifts in three of the acquisition are clearly visible in the interferogram. In X-band and C-band the differential phase for the CL presents a drifting behaviour. This constant drift in phase is the result of changes in the refractive index of the air. Luckily it can be compensated by applying an atmospheric artefact compensation technique described in Luca Pipia Ph. D. thesis. In L-band the ROCK provides a much more stable interferogram than the CL, but both are good results. In P-band only the ROCK provides a stable interferogram.

About the Probability Model Analysis, some interesting results were obtained. First of all the statistical behaviour of the reflectors corroborated which ones are visible and distinguishable at each band. The complete images do not follow a Rayleigh distribution for the amplitude, but it is quite similar. When zooming into the reflectors they do follow a Nakagami distribution. One of the most unexpected results is the discovery that in P-band the Central Limit Theorem is not fulfilled and thus the phases are not uniformly distributed. What this means is than in this band there is a small number of scatterers in each resolution cell and therefore the speckle phenomena is not fully developed. Another interesting result is that in X-band, one of the three acquisitions with a strong phase shift follows a slightly different PDF for the amplitude than the rest. This could imply that whatever caused the phase shifts also had an effect in the amplitudes and their probability distribution. Unfortunately this cannot be confirmed as the other two acquisitions with strong phase shifts do not present a distinguishable distribution. Finally there seems to be in P-band an increase in the amplitudes on each consecutive acquisition. This increase in amplitude has not been noticed in the Stability Analysis nor what might have caused it. Further investigation is required about this incident.

Three objectives were laid out in the introduction of this thesis as the main conclusion to be extracted.

The first objective was to test the stability of the TCRs. For a single TCR undisturbed by vegetation, such as CS, their response is stable in amplitude and phase as long as the frequency is not too low for the reflector size. In this case for X-band and C-band it is stable. For a single TCR placed in a location surrounded by vegetation, such as the CL, their response depends on the band. A low frequency is unaffected by the vegetation surrounding the reflector but if it is too low the wave will not scatter in the TCR. On the other side, a high frequency ensures the reflection in the TCR but it is more vulnerable to the instabilities caused by the clutter of vegetation. In this case for X-band the reflector seems very stable but some instabilities appear in some acquisitions caused by the vegetation, which makes the TCR unstable at this band. For C-band the reflector is very stable as the wavelength is long enough to be less affected by the vegetation but still be reflected in the TCR. For L-band the reflector is moderately stable as the frequency is low enough to ignore the vegetation but in the limit of being reflected in the TCR. If a reflector was to be placed behind some vegetations, only the frequencies with enough penetration but not excessive wavelength would provide a stable response. This TCRs might suffer from some minor deviations caused by changes in humidity or temperature, but they can be mostly compensated by externally calibrating the image with respect to one of the TCRs.

The second objective was to investigate the viability of using a natural object from the scene as a reflector and calibrator. In this case the natural object is a large rock covered by vegetation. For this reason we can already discard high bands such as X and C that are not able to penetrate the vegetation. The remaining L and P bands can penetrate vegetation and scatter in the rock. Both bands present a very stable response which is very good news. In the case of L-band the natural Rock is a more stable reflector than the artificially placed CL. Both bands present an almost identical level of standard deviation in the phase for the Rock. This indicates that despite P-band not having a fully developed speckle, the natural reflector provides a very stable response. Because of this stability it can be used as a reference for the external calibration procedure. This indicates that if a big and stable object, such as the mentioned rock, is present in the scenery, for some bands it might not be necessary to place an artificial TCR to use as reference.

Finally, the third objective was to study the accuracy of the differential interferograms at the different frequencies. In the introduction, the requirement of measuring displacements in the range from 1 cm to 1 mm was established. This displacements are related to a phase shift that depends on the frequency. The Table 7.1 below shows the phase shifts caused by the displacements at each band.

		Phase Shift Δφ	
Bands	**Frequency**	**for Δd = 1 cm**	**for Δd = 1 mm**
X	9.6 GHz	230.4º	23.04º
C	5.4 GHz	129.6º	12.96º
L	1.27 GHz	30.48º	3.05º
P	0.45 GHz	10.8º	1.08º

Table 7.1: Phase Shifts caused by Terrain Displacements in all bands

In order for a differential interferogram to successfully measure terrain displacements, the phase shift caused by the displacement has to be easily identifiable and distinguishable from the rest of phase deviations. Ideally in an interferogram there would not be any phase deviations not caused by displacements, but it is not always possible to compensate all the shifts. Let's take a look into each frequency band. For bands X and C the only viable interferogram would be the CL, as the Rock is not even a stable reflector. Both interferograms present a drifting phase that is the result of the changes in the refractive index of the atmosphere. This drift is stronger the higher the frequency, for this reason in bands L and P it cannot be identified. Luckily this drift in the phase of the interferogram can be compensated by applying an atmospheric artefacts compensation technique. This compensation technique is described in Luca Pipia's Ph.D dissertation. Unfortunately in X-band, the strong phase shifts in three of the acquisitions appear clearly in the interferogram and are not easily compensated. Because of this we cannot use X-band to accurately measure terrain displacements. On the other side in C-band, the standard deviation of the phase is around 3º without having applied the refractive index compensation, so after this compensation it would be even lower. As seen in Table 7.1 the minimum phase shift caused by a displacement of 1mm would be 12.96º, which is many times the deviation. For this reason we can accurately use C-band to measure displacements in the CL. For band L there is the possibility of measuring displacements in the CL as well as in the Rock. For the CL the standard deviation is around 5.8º and for the Rock it is around 0.9º. For this reason we can accurately measure displacements in the Rock but only measure large displacements in the CL. For band P the only possibility is the Rock, which has a standard deviation of around 1º. For this reason medium and large displacements can be accurately measured but not small ones, as the shift is similar to the deviation of the interferogram.

As a summary of everything said in this paragraph. The measurement of displacements in X-band would not be accurate because of the instabilities induced in some acquisitions by the vegetation surrounding the TCR. In C-band and in L-band the measurement would be accurate as the minimum phase shift caused by the displacement is higher than the standard deviation of the interferometric phase. In P-band, despite having a partially developed speckle and having a smaller number of scatterers per pixel, the measurement of displacements in the Rock would be relatively precise.

Finally we will discuss some future developments and works related to this thesis.

The next step to continue the investigation about this topic would be the realization of another measurement campaign in the same area, the “Castell de Subirats”, with some variations from the previous one. To begin with, it would be beneficial to get an additional bigger reflector and place it somewhere undisturbed by vegetation. This way a very stable reflector could be used as reference for the external calibration in bands X, C and probably L, simultaneously. Another focus of this new measurement campaign would be to manually displace the reflectors and study if the displacement could be measured with precision. The Rock is impossible to displace so P-band would not be used in the measures, but the new bigger TCR mentioned above could enable L-band for precise measures.

Another road the investigation could turn into is the disuse of artificially placed reflectors. Not every scenery is fitted for the placement of artificial reflectors, such as very steep cliffs. It would be an interesting topic of investigation the exclusive use of natural reflectors as reference points for calibration and measurements.

A topic that was left hanging in this thesis and could be further investigated is the supposed increase in the amplitude of every consecutive image in Band P. In the Probability Model Analysis this increase in the amplitude could be seen in the figures corresponding to Chapter 6.3. During the Stability Analysis this increase was not perceived but we did not dig into the numbers to accept or dismiss this supposed increase. If this supposed increase in the amplitudes is true then the causes behind it can be searched and preferably compensated. It could have been a software or a hardware problem with the GB-SAR system.

[This page is intentionally left blank]

Bibliography:

Books

[1] Mehrdad Soumekh. *Synthetic Aperture Radar Signal Processing with MATLAB Algorithms*. New York, USA: John Wiley & Sons Inc. , 1999.

[2] Allen B. Downey, Jeffrey Elkner, Chris Meyers. *How to Think Like a Computer Scientist: Learning with Python*. Massachusetts, USA: Green Tea Press, January 2002.

Ph. D. Dissertations

[3] Luca Pipia, “Polarimetric Differential SAR Interferometry with Ground-Based Sensors” Ph.D. dissertation. Department of Signal Theory and Communications. Universitat Politècnica de Catalunya. Barcelona, Spain, 2009.

[4] Adrià Amézaga, “Design and implementation of an SDR-based multi-frequency ground-based SAR system” Ph.D. dissertation. Department of Signal Theory and Communications. Universitat Politècnica de Catalunya. Barcelona, Spain, August 2020.

Papers

[5] A. Ferretti, C. Prati, and F. Rocca. “Permanent Scatterers in SAR Interferometry”. IEEE Transactions on Geoscience and Remote Sensing, Vol. 39, No. 1, January 2001. DOI: 10.1109/36.898661.

[6] A. Amézaga, C. López, R. Jové. “A Multi-Frequency SDR-Based GBSAR: System Overview and First Results”. Remote Sensing, Vol. 13, No. 9: 1613. April 2021. DOI: 10.3390/rs13091613.

[7] Giu Gao. "Statistical Modeling of SAR Images: A Survey". Sensors, Vol. 10, No. 1: 775-795. January 2010. DOI: 10.3390/s100100775

[8] G. Moser, J. Zerubia, S. B. Serpico. "*SAR amplitude probability density function estimation based on a generalized Gaussian model*". IEEE Transactions on Image Processing, Vol. 15, No. 6, pp. 1429-1442, June 2006. DOI: 10.1109/TIP.2006.871124.

[9] K. M. Noga, R. Studański. “Estimation of Nakagami Distribution Parameters in Describing a Fading Radio-Communication Channel”. Scientific Journal of Polish Naval Academy, Vol. 204, No.1, pp.69-81, March 2016. DOI: 10.5604/0860889X.1202437.

[10] A. Abdi and M. Kaveh. "*Performance comparison of three different estimators for the Nakagami m parameter using Monte Carlo simulation*". IEEE Communications Letters, Vol. 4, No. 4, pp. 119-121. April 2000. DOI: 10.1109/4234.841316.

Online Resources

[11] Balamis official website. Online Available: https://www.balamis.com/

[12] Thuy Le Toan. Fabio Rocca. “*Advanced Training Course on Land Remote Sensing*”. SAR & Interferometry lectures. European Space Agency (ESA), July 2014. Material Online Available: https://earth.esa.int/landtraining07/material.html .

[13] A. Ferretti, C. Prati, and F. Rocca. “An Overview of SAR Interferometry”. European Space Agency (ESA), July 2014. Material Online Available: https://earth.esa.int/workshops/ers97/program-details/speeches/rocca-et-al/

[14] Eric Fielding. “Applied Remote Sensing Training: Introduction to SAR Interferometry”. National Aeronautics and Space Administration (NASA). Online Available: https://appliedsciences.nasa.gov/sites/default/files/Session4-SAR-English_0.pdf

[15] Python Documentation. Online Available: https://docs.python.org/3/tutorial/index.html

[16] Python Library NumPy Documentation. Online Available: https://numpy.org/doc/stable/reference/index.html

[17] Python Library MATPLOTLIB Documentation. Online Available: https://matplotlib.org/stable/contents.html

[18] Wikipedia. Various entries about diverse topics. Online.

- https://en.wikipedia.org/wiki/Synthetic-aperture_radar
- https://en.wikipedia.org/wiki/Central_limit_theorem
- https://en.wikipedia.org/wiki/Nakagami_distribution
- ...

Appendices:

In the appendices all the figures obtained as result of this project are shown with greater detail. The figures are organized by chapters.

Appendices Sections

1. Data Analysis

In this chapter the figures shown correspond to the absolute value in dB of the first acquisition at each band in both Polar and Cartesian coordinates.

1.1. Acquired Images

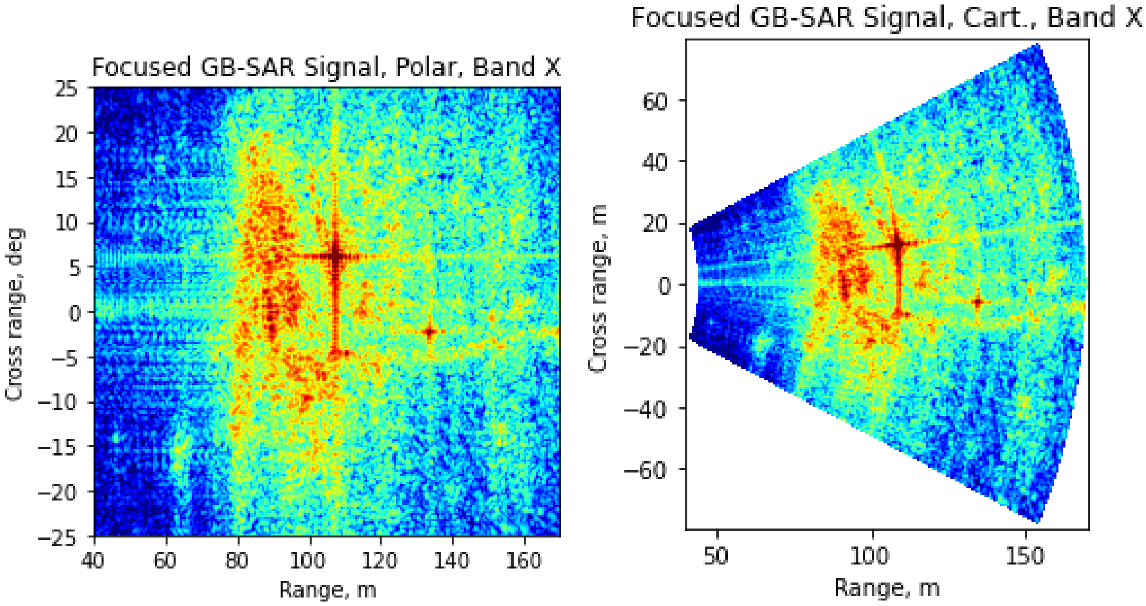

Focused Signal. Absolute power in dB. Polar & Cartesian Coordinates. Band X

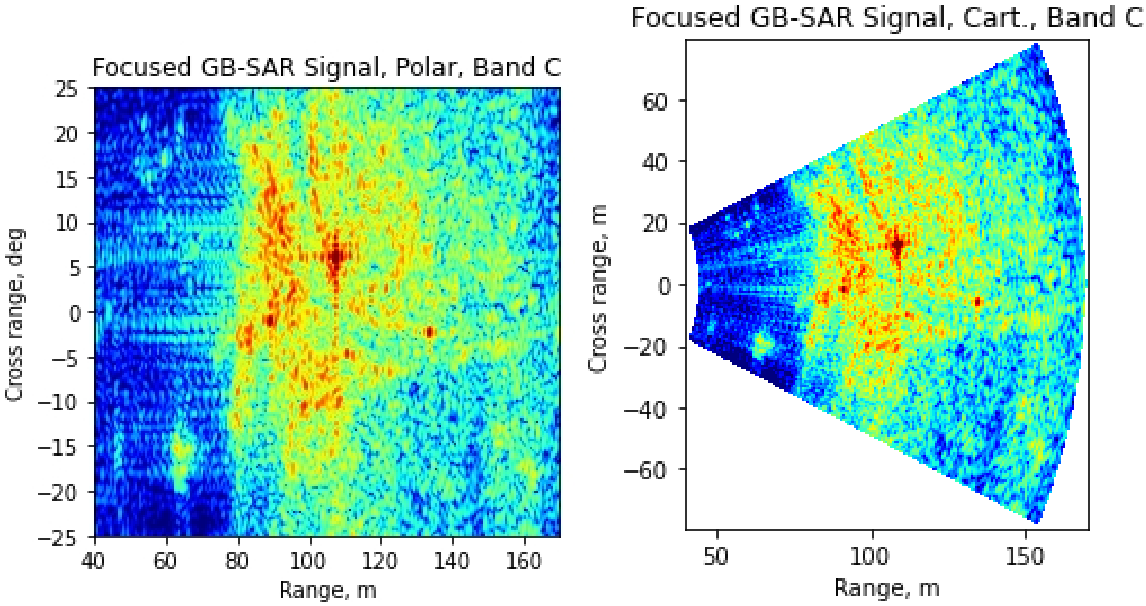

Focused Signal. Absolute power in dB. Polar & Cartesian Coordinates. Band C

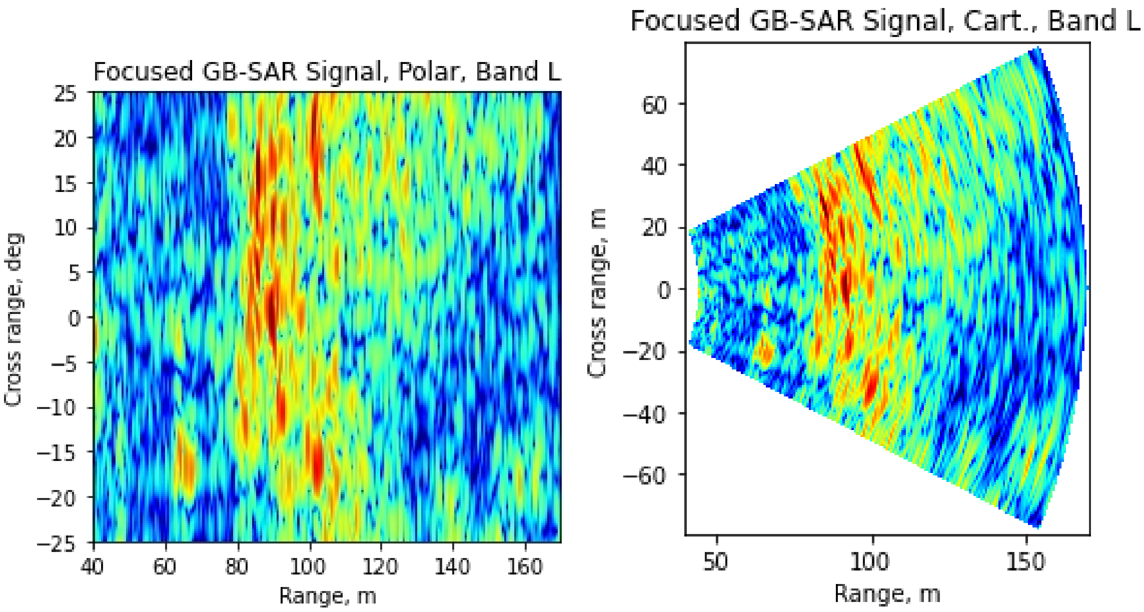

Focused Signal. Absolute power in dB. Polar & Cartesian Coordinates. Band L

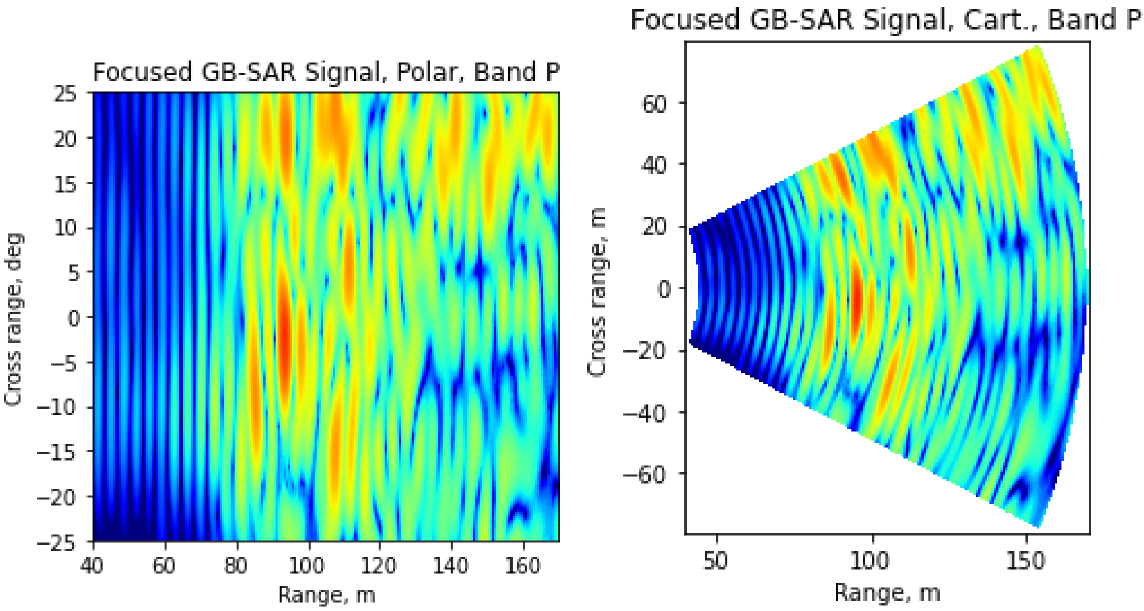

Focused Signal. Absolute power in dB. Polar & Cartesian Coordinates. Band P

2. Stability Analysis

In this chapter the figures show the stability of the selected reflectors throughout the consecutive acquisitions at each band.

2.1. Reflector Stability

In this section the figures show the temporal evolution of the amplitude and the phase for some pixels selected from the images. The images are uncalibrated, internally calibrated and externally calibrated respectively.

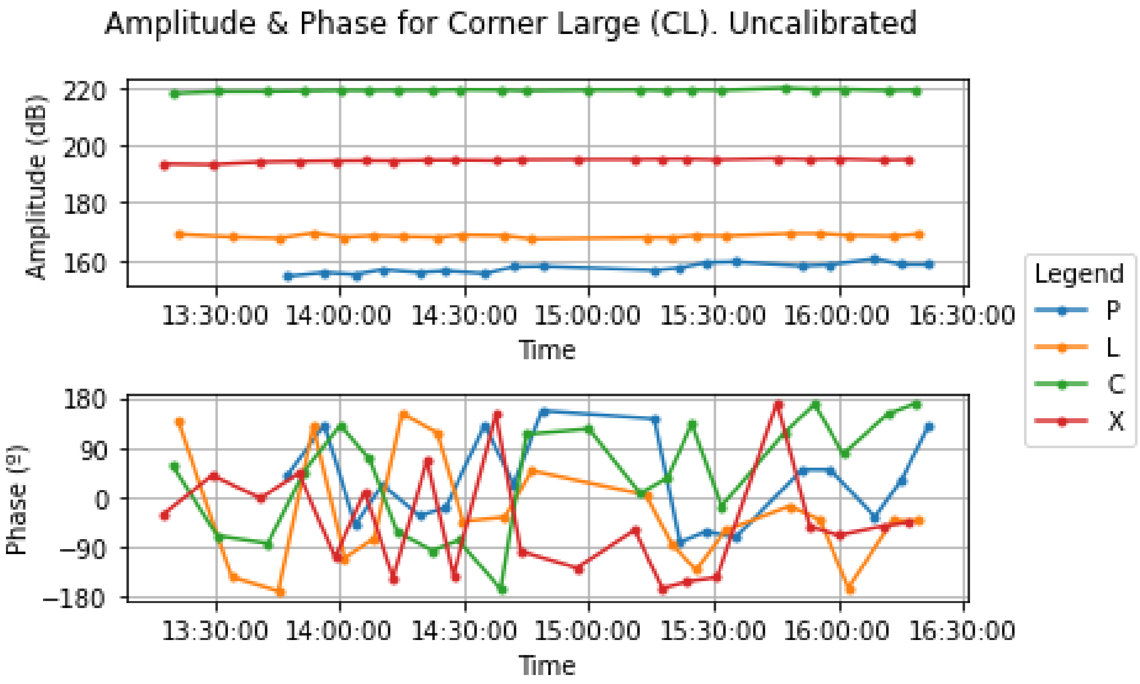

Amplitude & Phase Temporal Evolution. Uncalibrated. Corner Large

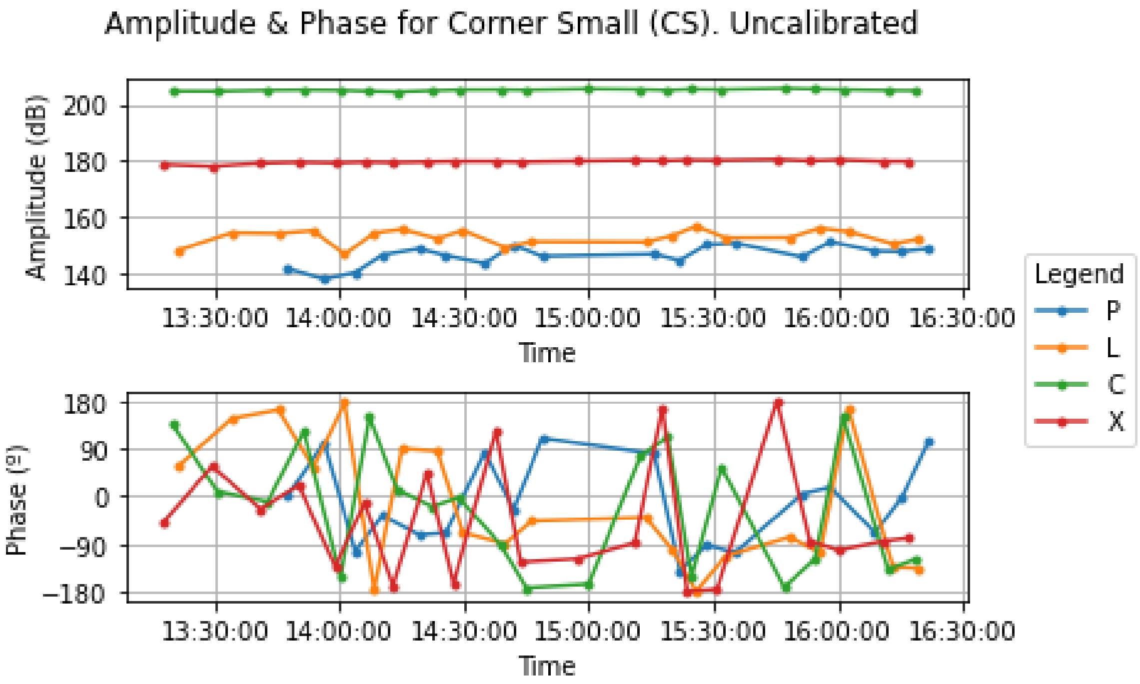

Amplitude & Phase Temporal Evolution. Uncalibrated. Corner Small

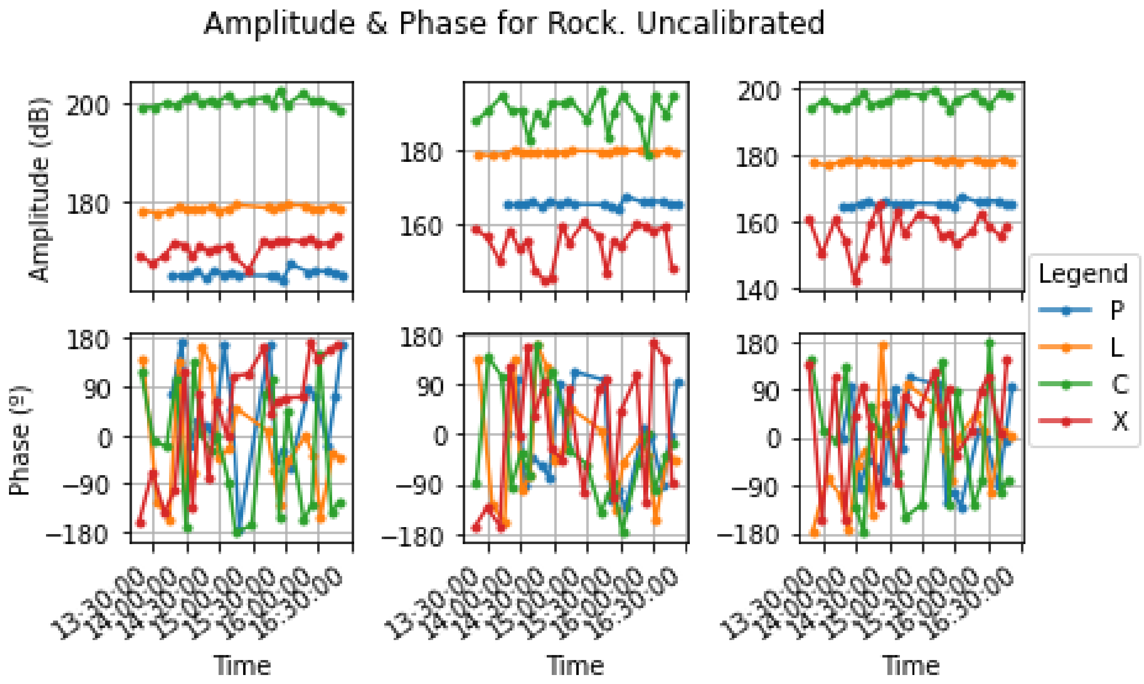

Amplitude & Phase Temporal Evolution. Uncalibrated. Rock

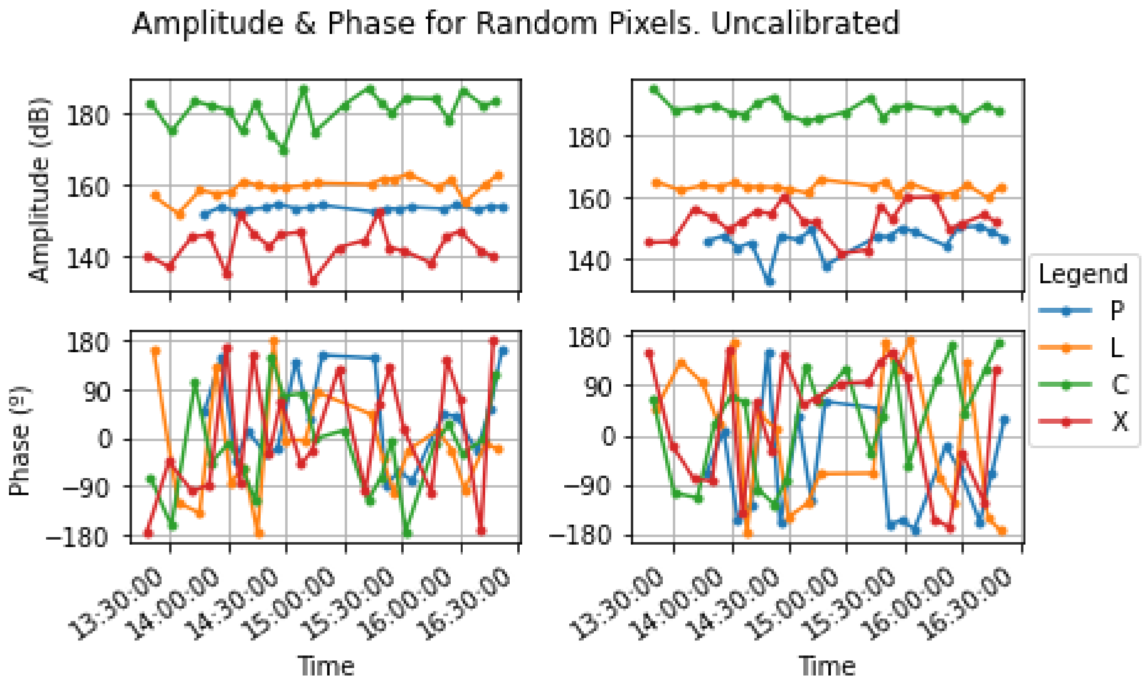

Amplitude & Phase Temporal Evolution. Uncalibrated. Random Pixels

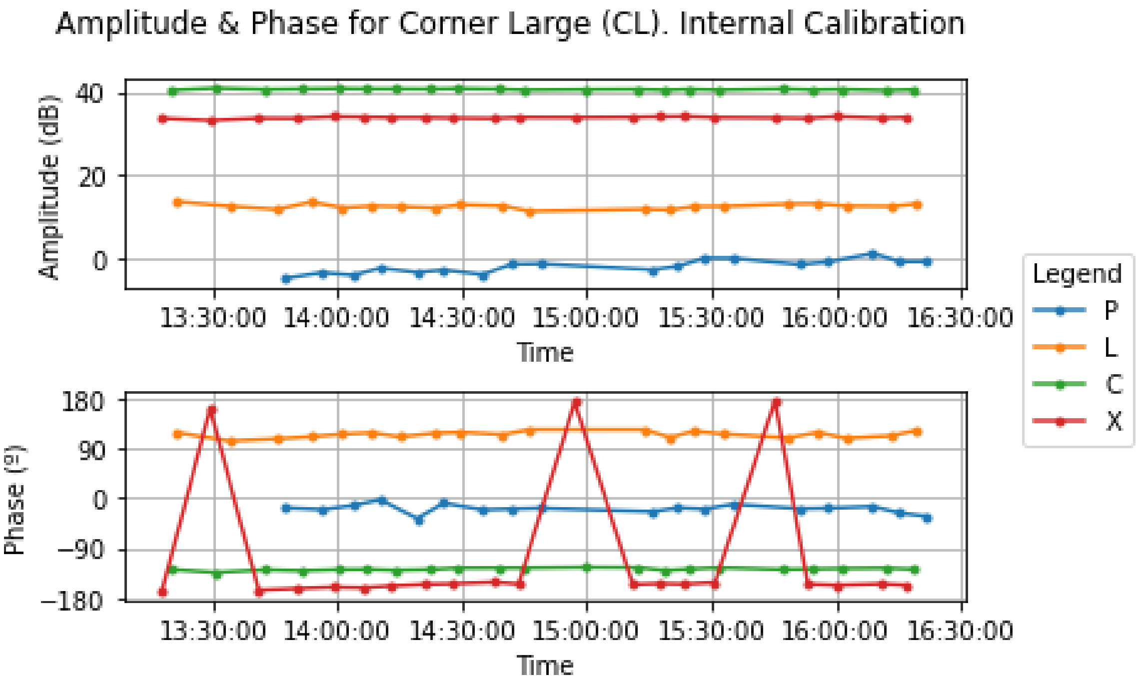

Amplitude & Phase Temporal Evolution. Internal Calibration. Corner Large

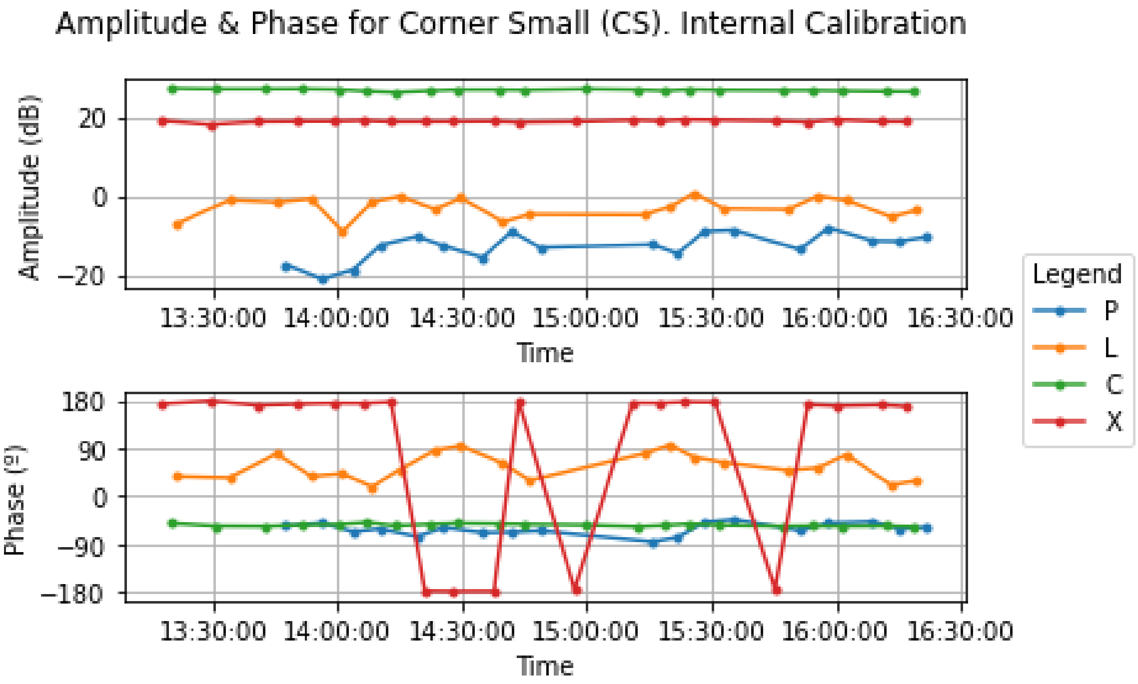

Amplitude & Phase Temporal Evolution. Internal Calibration. Corner Small

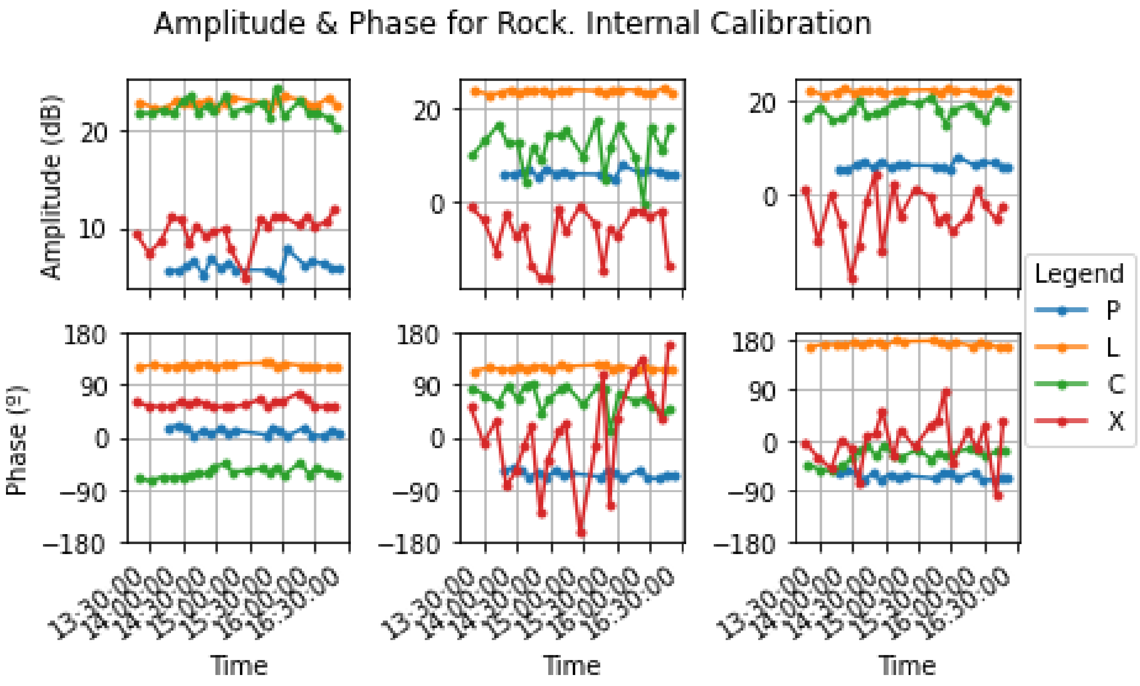

Amplitude & Phase Temporal Evolution. Internal Calibration. Rock

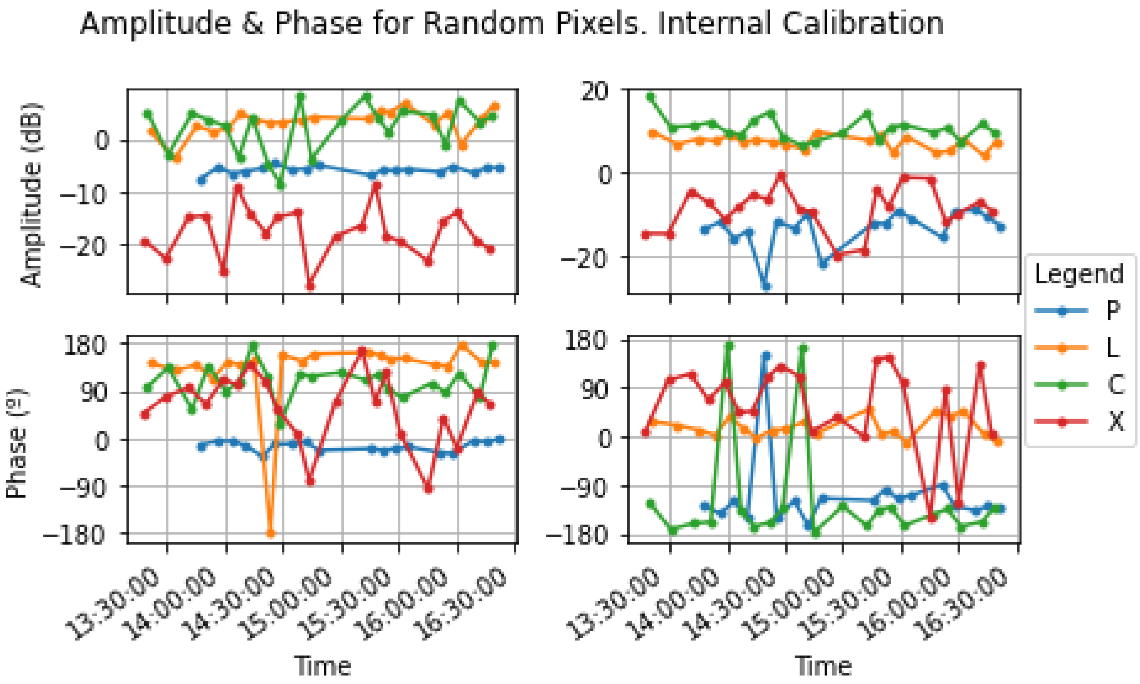

Amplitude & Phase Temporal Evolution. Internal Calibration. Random Pixels

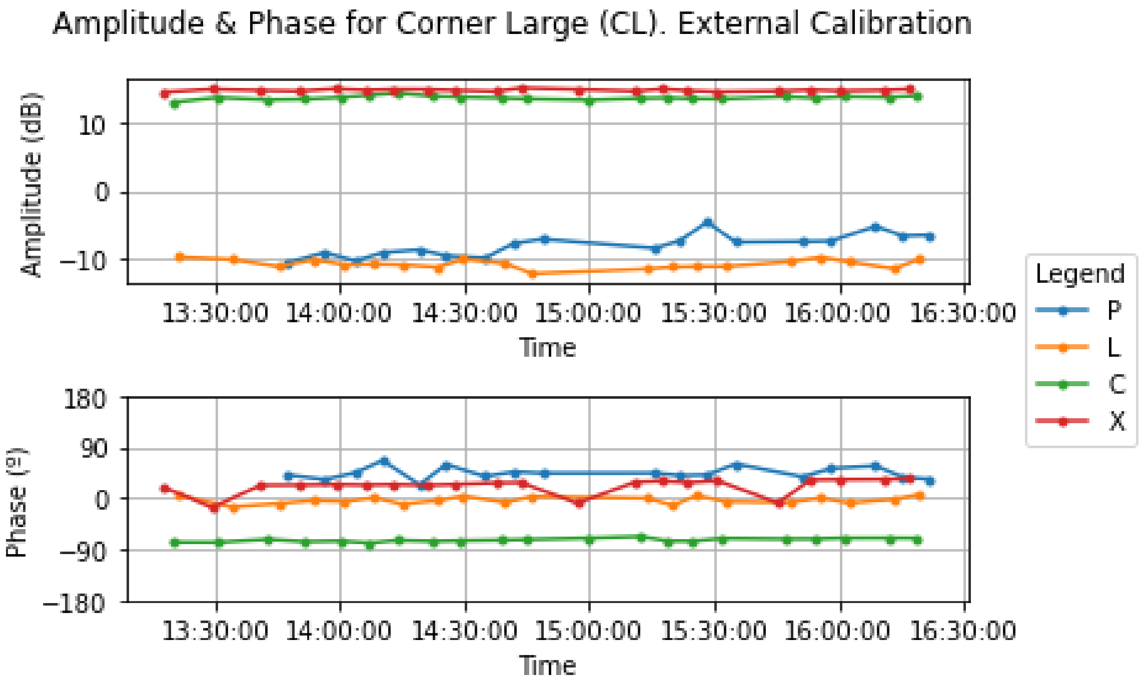

Amplitude & Phase Temporal Evolution. External Calibration. Corner Large

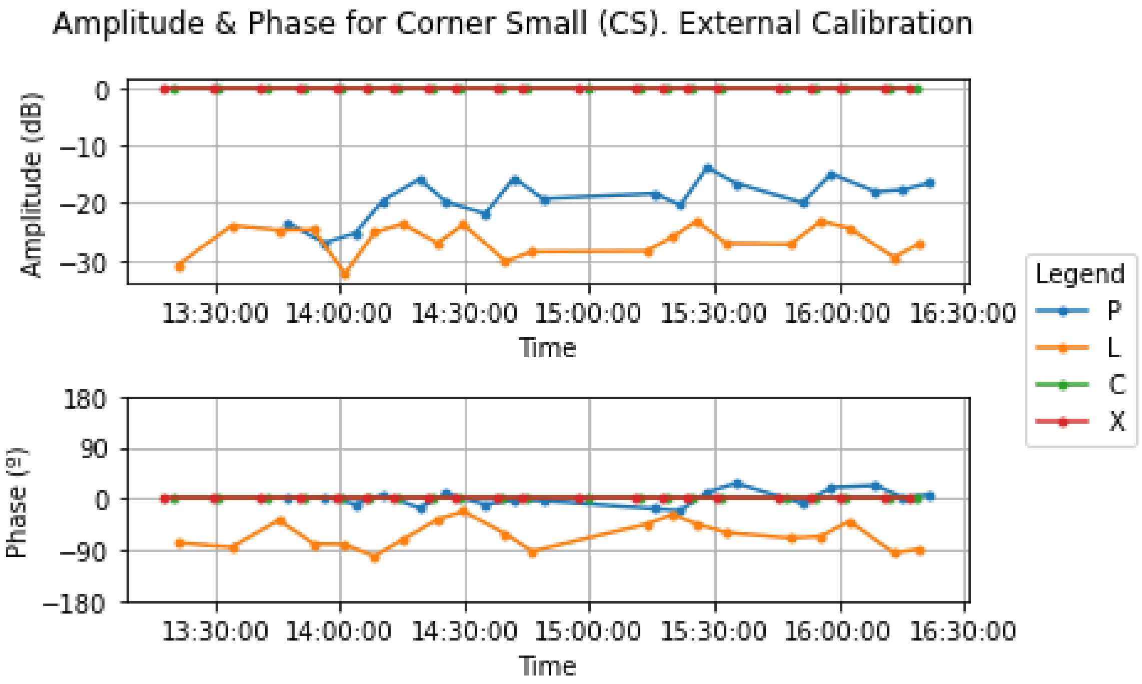

Amplitude & Phase Temporal Evolution. External Calibration. Corner Small

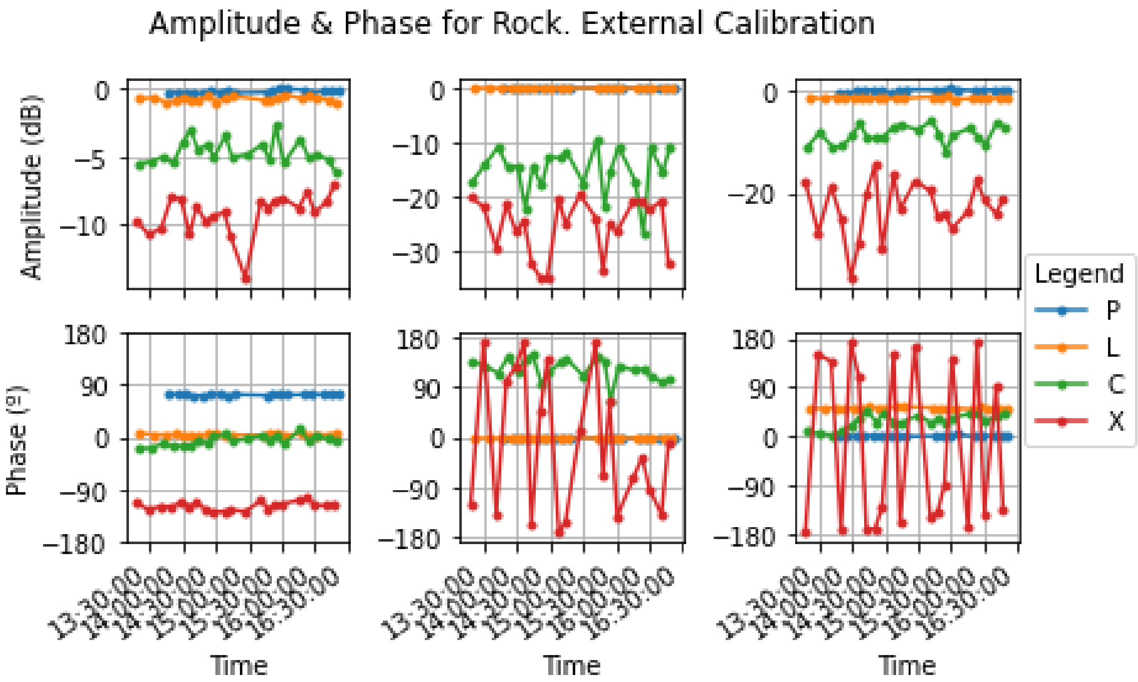

Amplitude & Phase Temporal Evolution. External Calibration. Rock

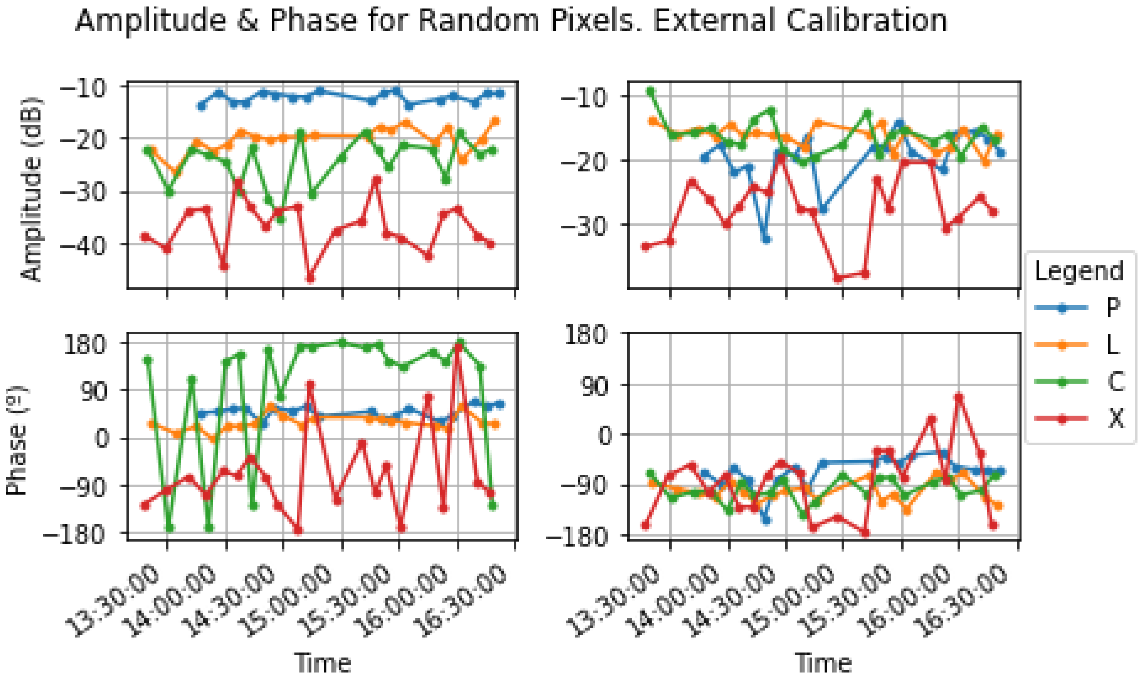

Amplitude & Phase Temporal Evolution. External Calibration. Random Pixels

2.2. Differential Stability

In this section the figures show the results of the correlation between images. First are shown the pixels with high correlation and finally the differential phase is shown.

2.2.1. Differential General Stability

Here are shown the pixels with a high correlation modulus (higher than 0,8) in all the correlations computed at each band.

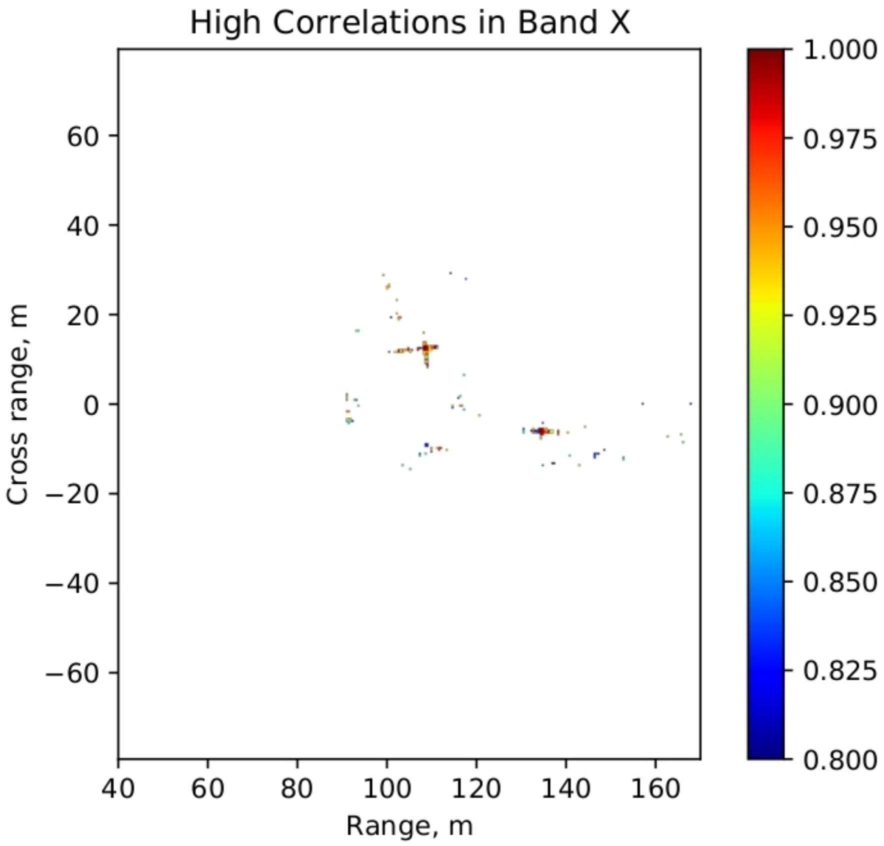

Pixels with abs(correlation)>0,8 in all the correlations computed for Band X

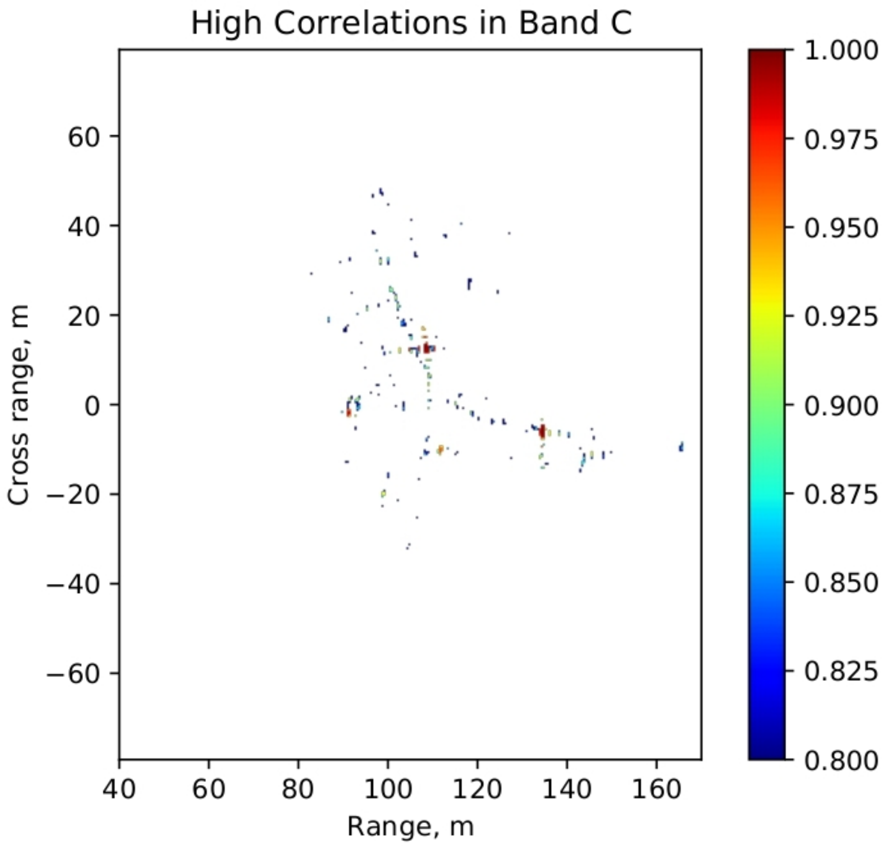

Pixels with abs(correlation)>0,8 in all the correlations computed for Band C

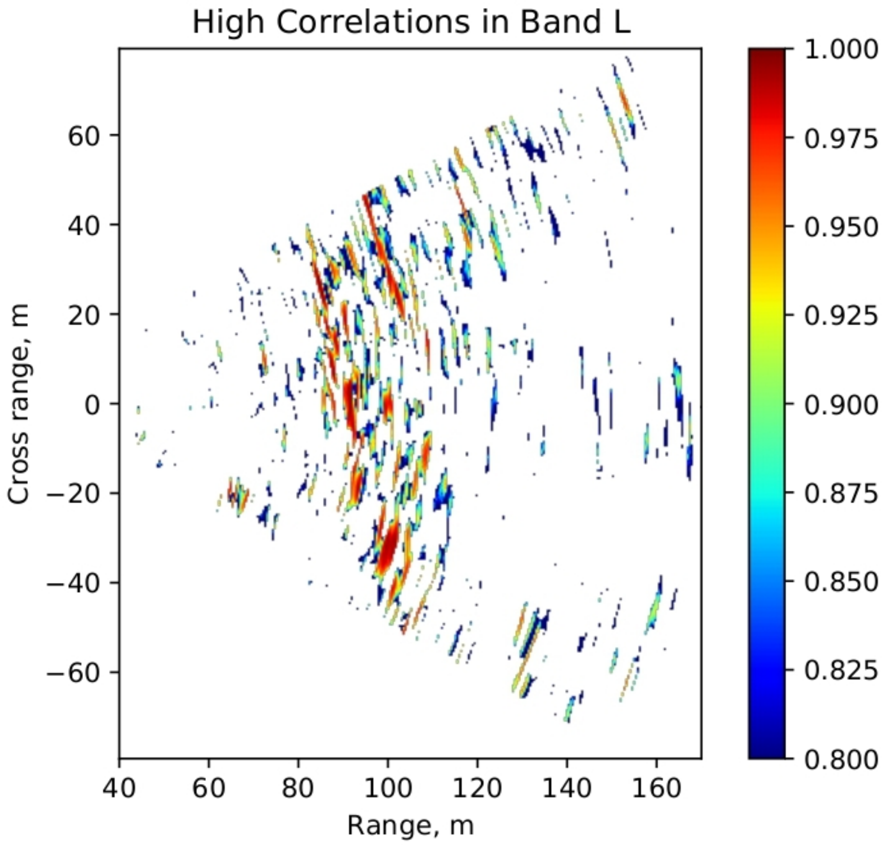

Pixels with abs(correlation)>0,8 in all the correlations computed for Band L

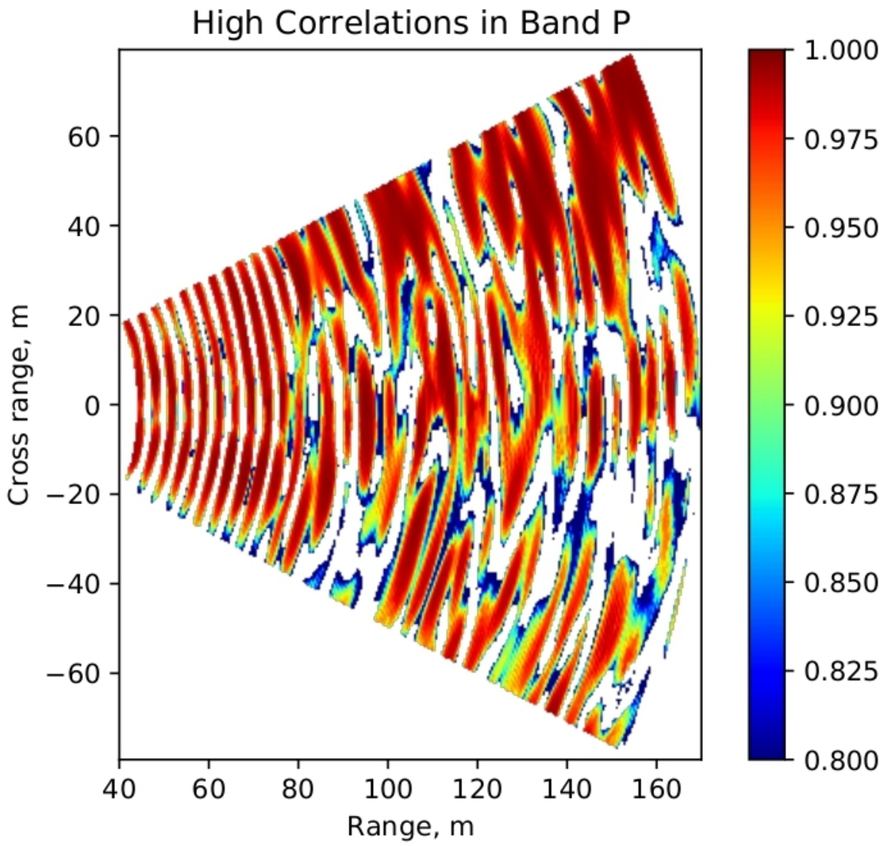

Pixels with abs(correlation)>0,8 in all the correlations computed for Band P

2.2.2. Differential Temporal Stability

Here are shown the correlation modulus and differential phase of the correlation for the selected reflectors.

At the end are also shown the simple phase difference between calibrated images for the selected reflectors.

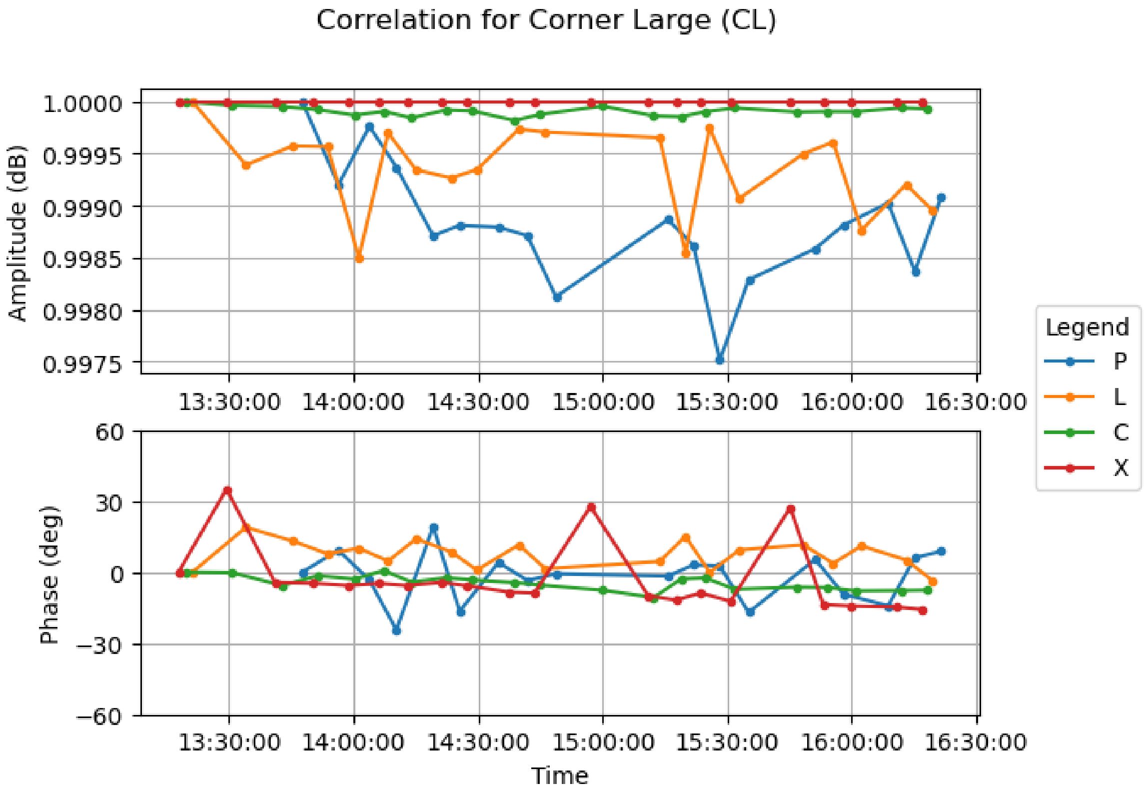

Correlation Amplitude & Phase Temporal Evolution. Corner Large

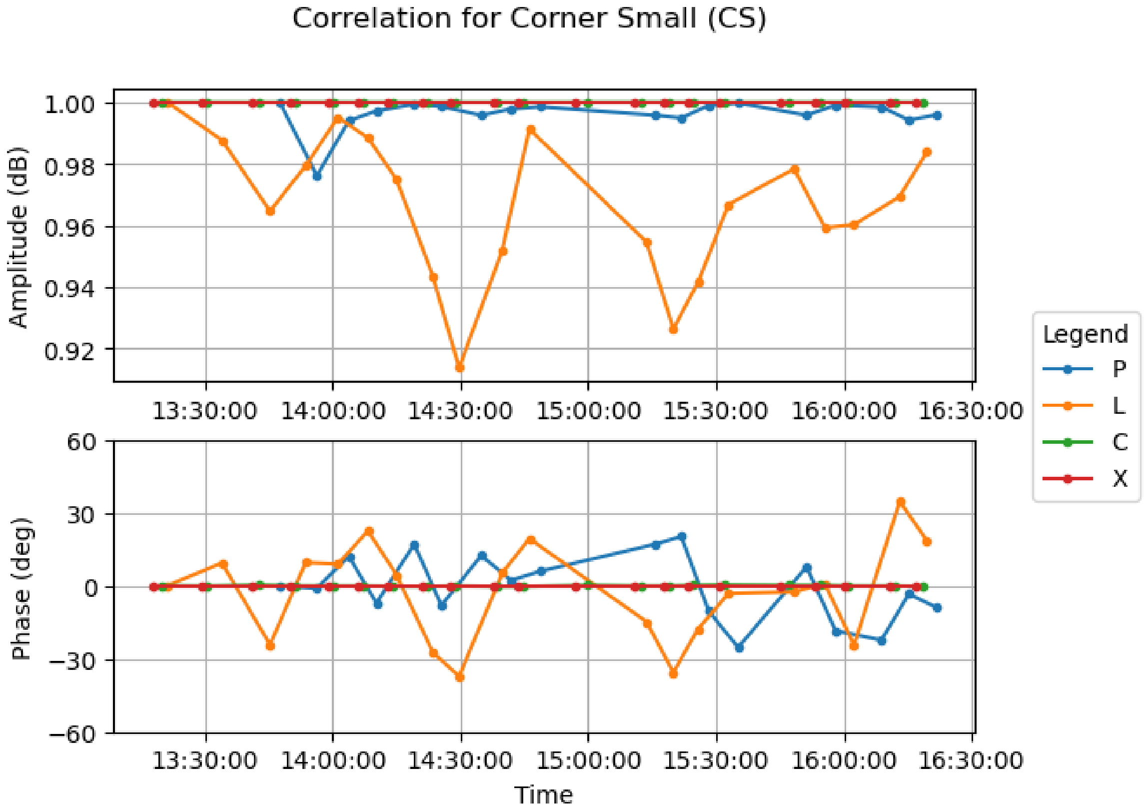

Correlation Amplitude & Phase Temporal Evolution. Corner Small

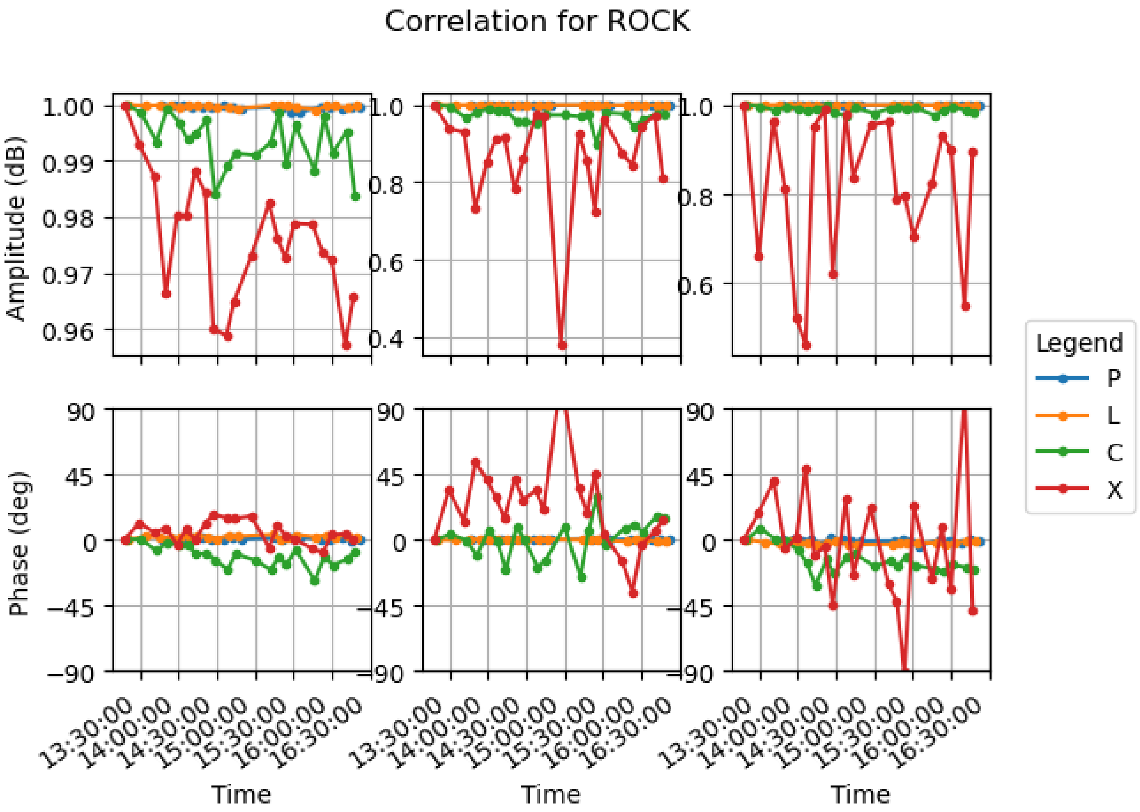

Correlation Amplitude & Phase Temporal Evolution. Rock

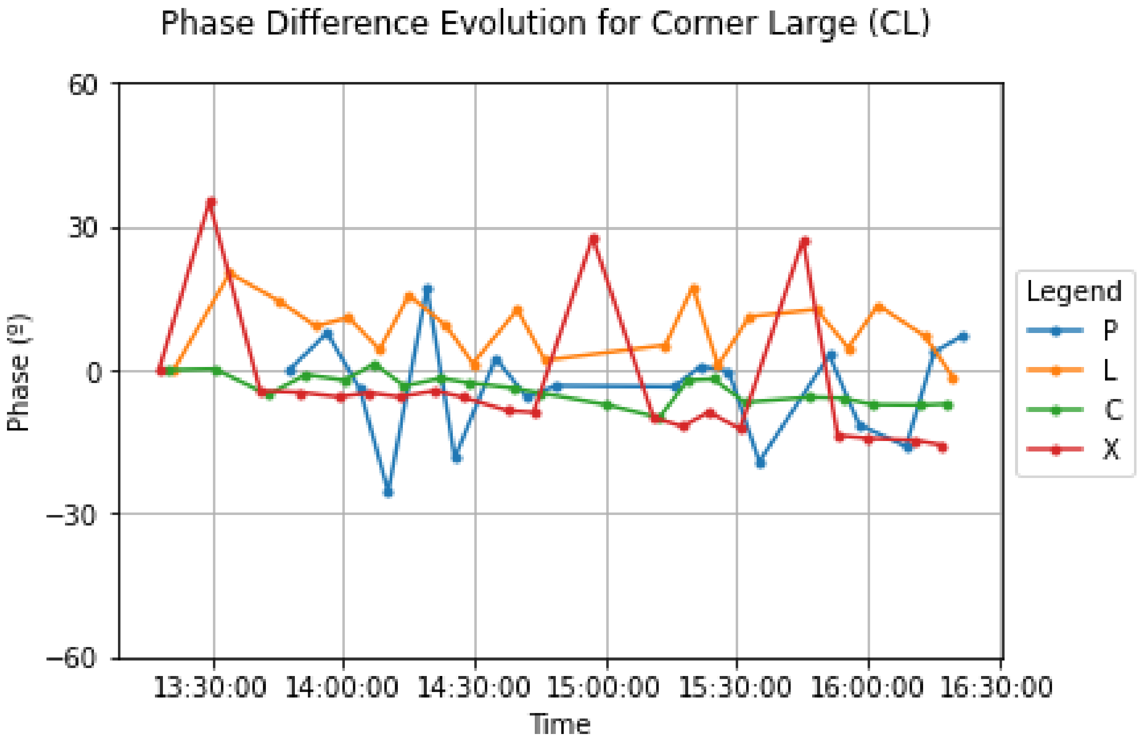

Phase Difference between the 1st & the rest of acquisitions. Corner Large

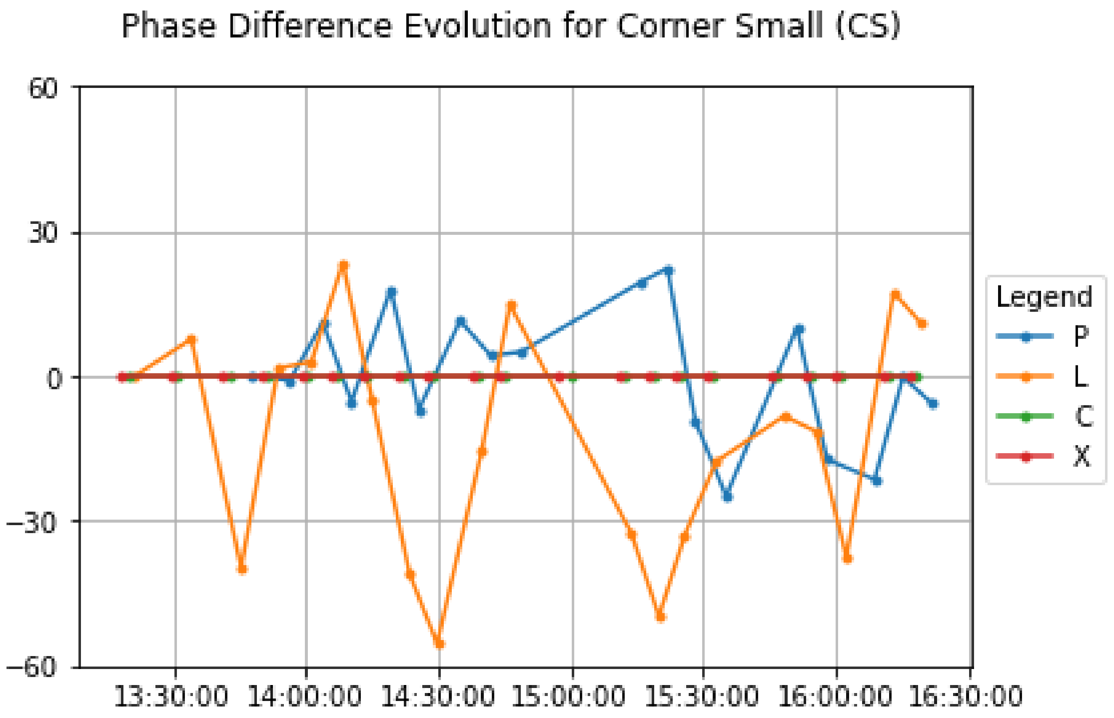

Phase Difference between the 1st & the rest of acquisitions. Corner Small

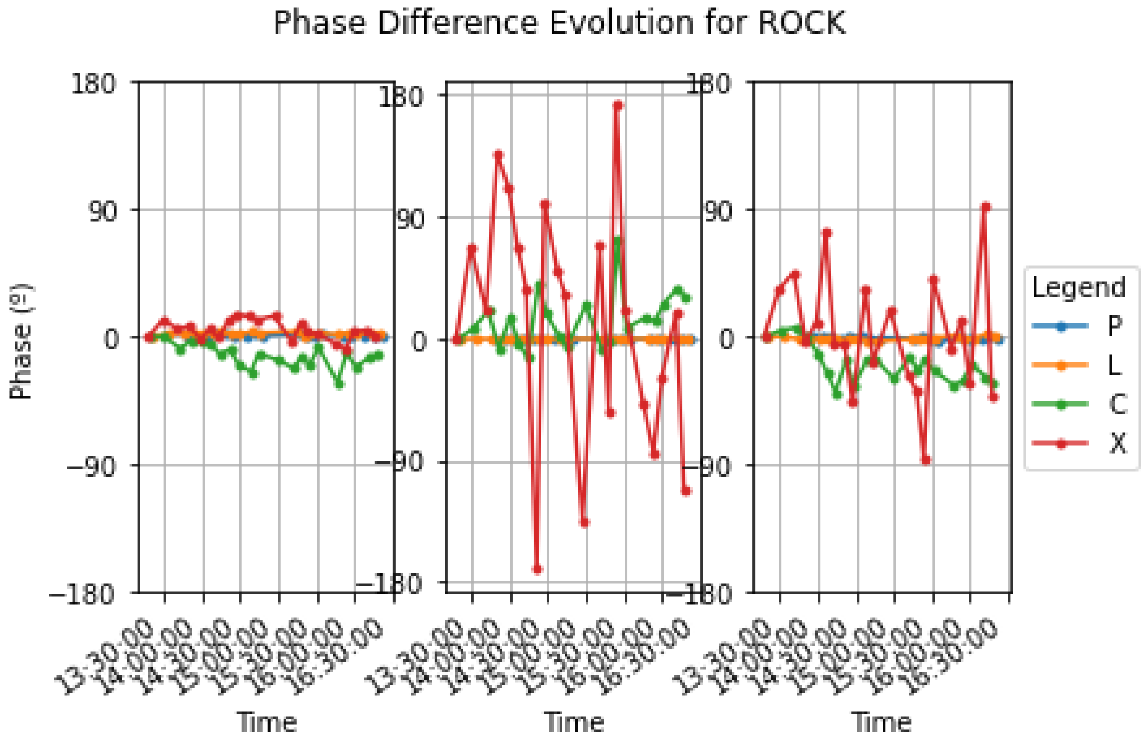

Phase Difference between the 1st & the rest of acquisitions. Rock

3. Statistical Model Analysis

In this chapter the figures show the results of the statistical analysis.

3.1. Probability Models & Histograms

In this section the figures show the comparison between the histograms obtained from the pixels of the images and the Probability Density Functions.

3.1.1. Complete Images

Here are shown the histograms obtained from using all the pixels, except for the shadowed area just below the sensor, from all images at each band.

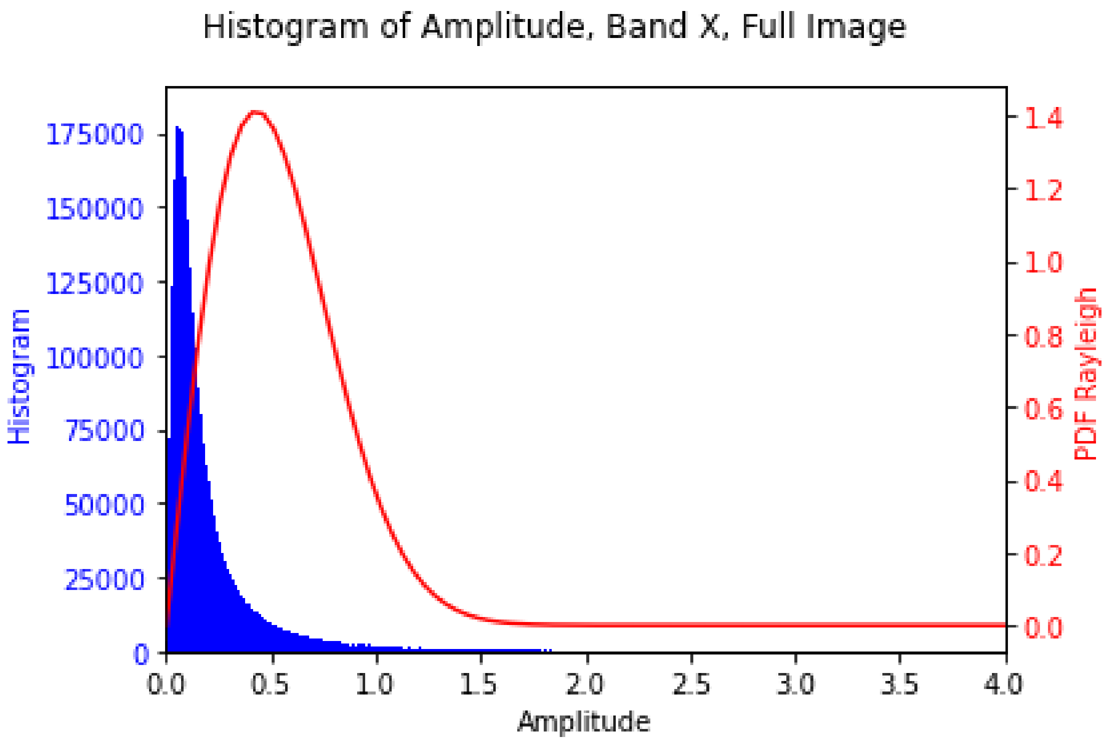

Histogram of Amplitude & Rayleigh PDF Comparison. Full Image. Band X

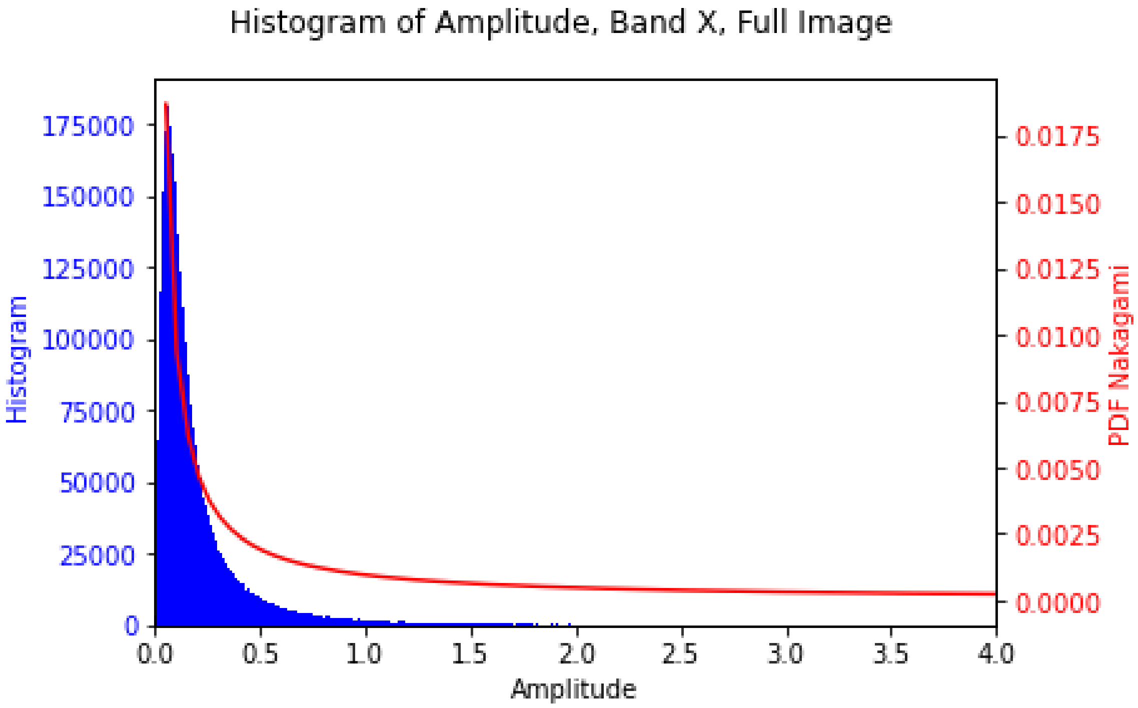

Histogram of Amplitude & Nakagami PDF Comparison. Full Image. Band X

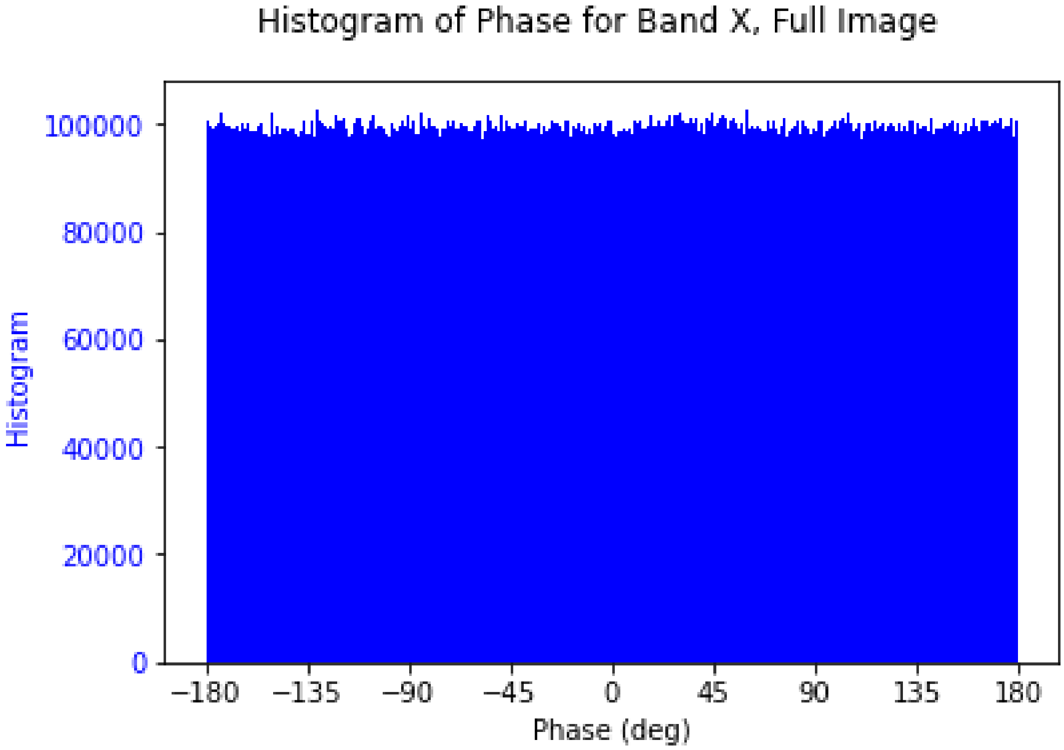

Histogram of Phase. Full Image. Band X

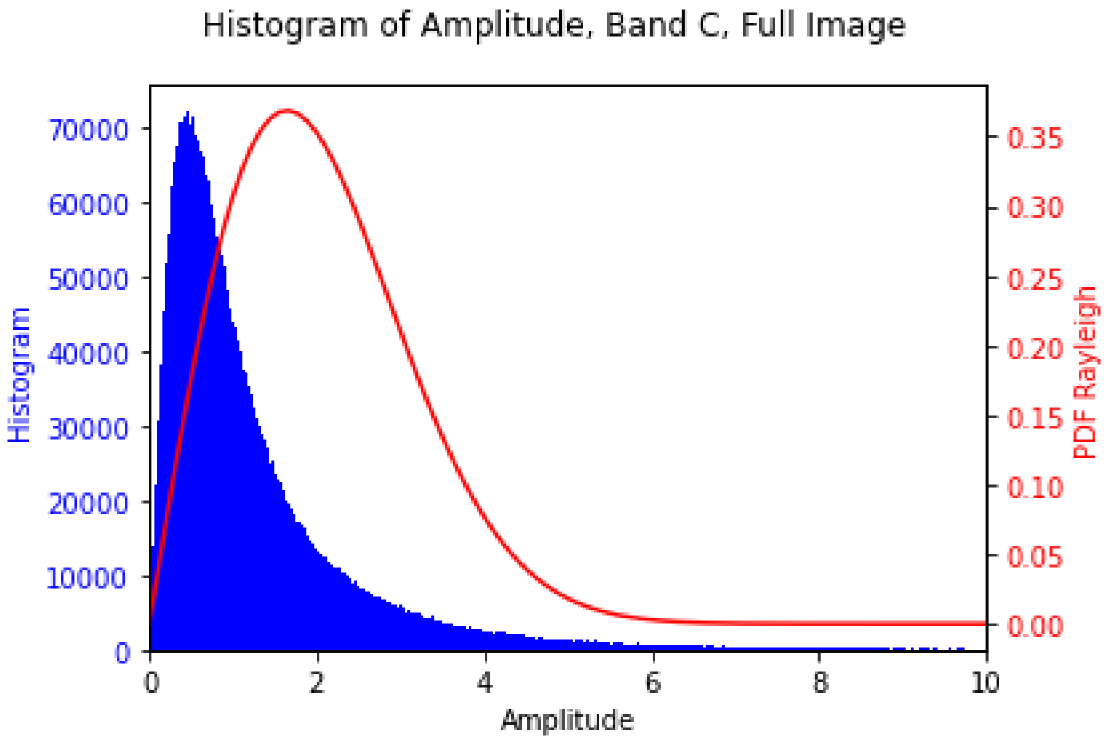

Histogram of Amplitude & Rayleigh PDF Comparison. Full Image. Band C

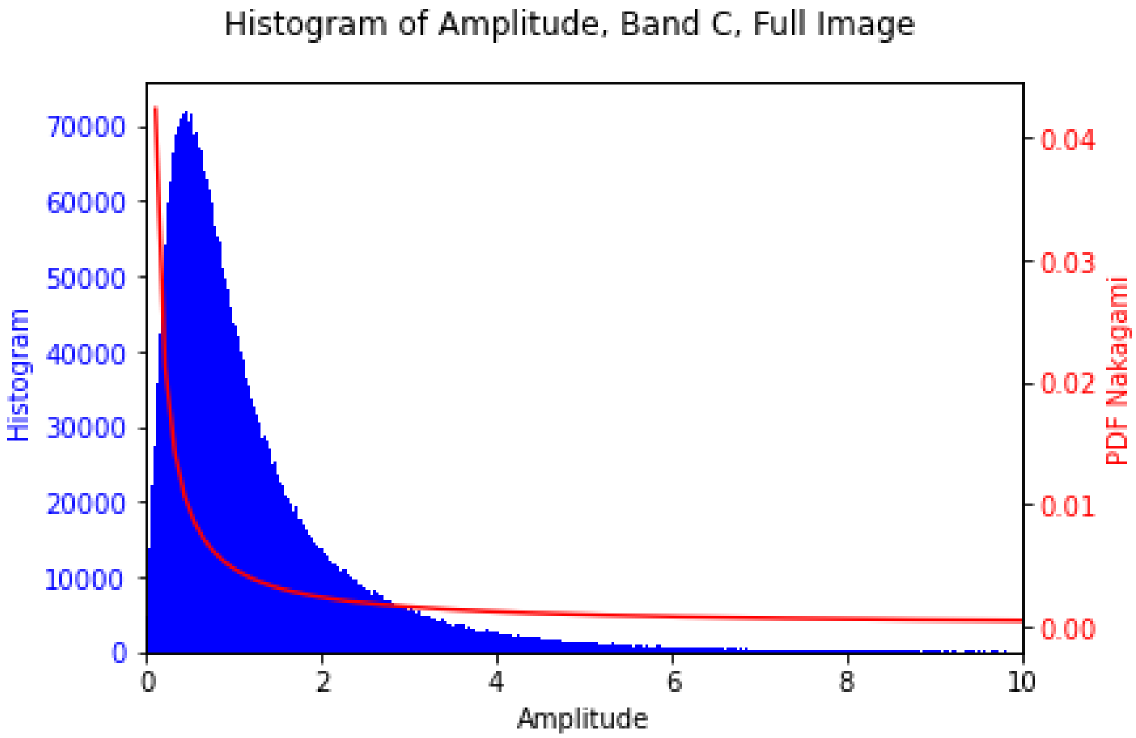

Histogram of Amplitude & Nakagami PDF Comparison. Full Image. Band C

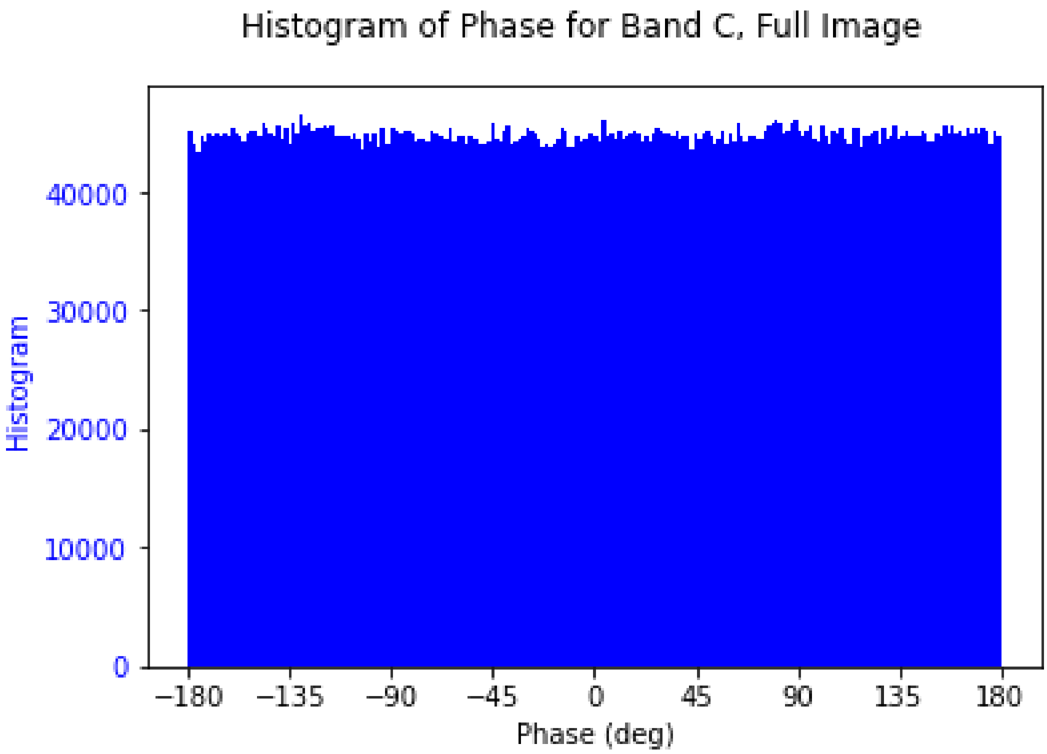

Histogram of Phase. Full Image. Band C

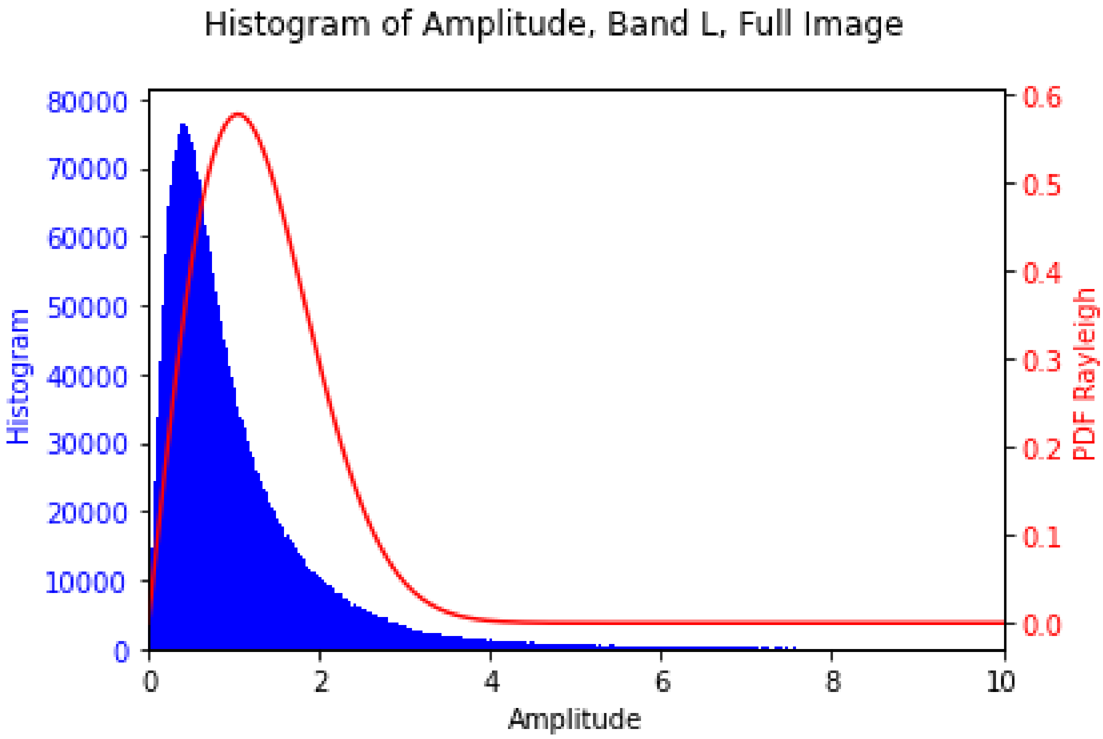

Histogram of Amplitude & Rayleigh PDF Comparison. Full Image. Band L

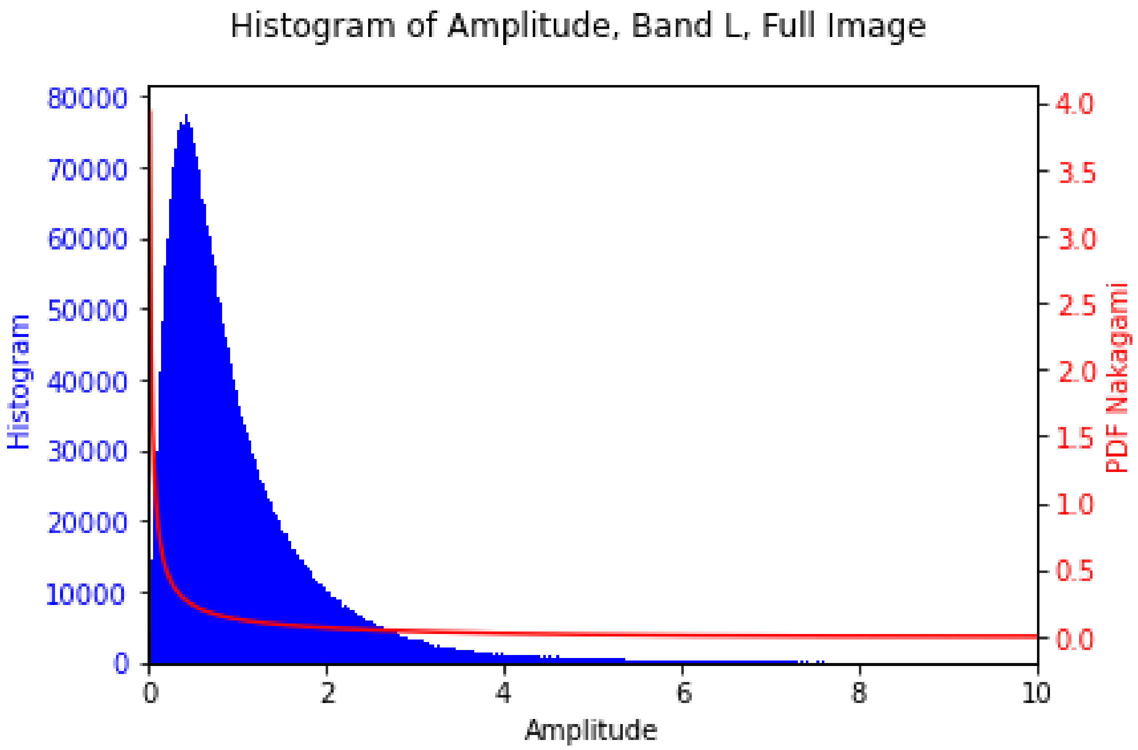

Histogram of Amplitude & Nakagami PDF Comparison. Full Image. Band L

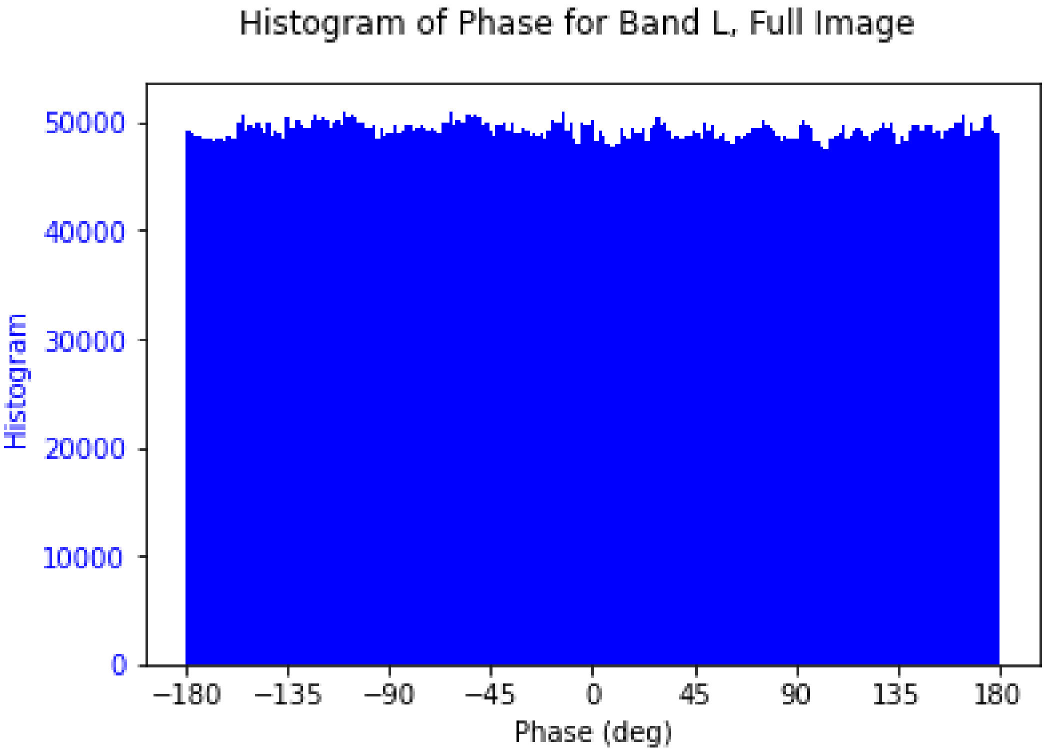

Histogram of Phase. Full Image. Band L

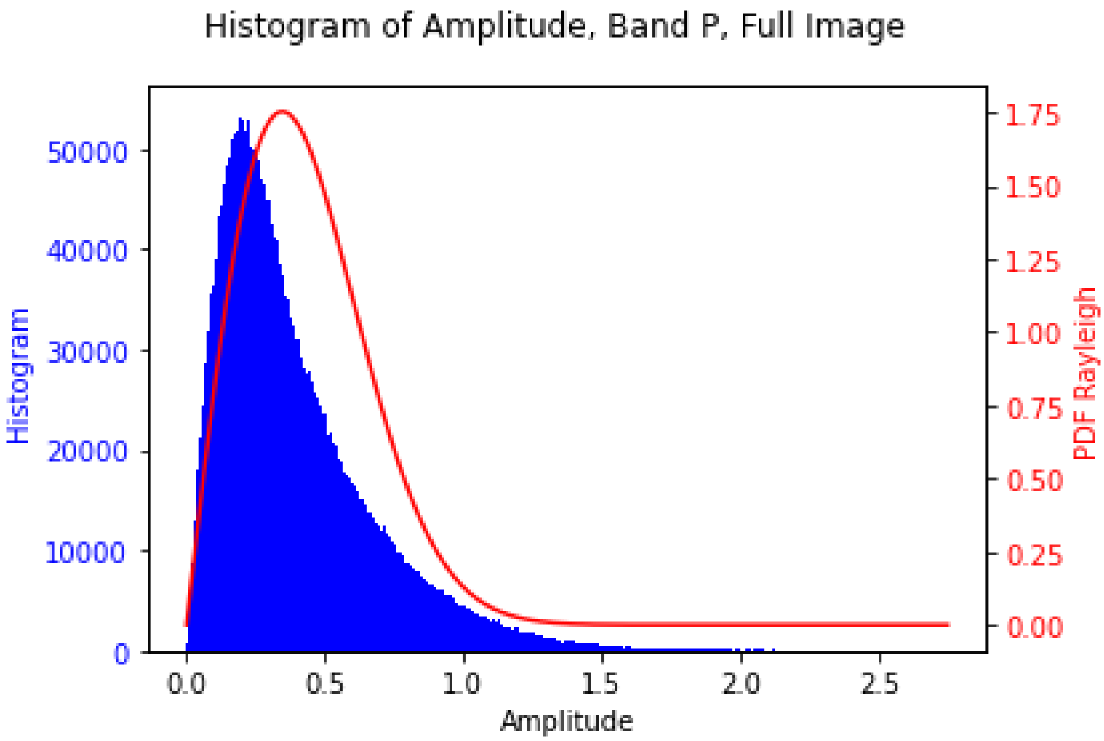

Histogram of Amplitude & Rayleigh PDF Comparison. Full Image. Band P

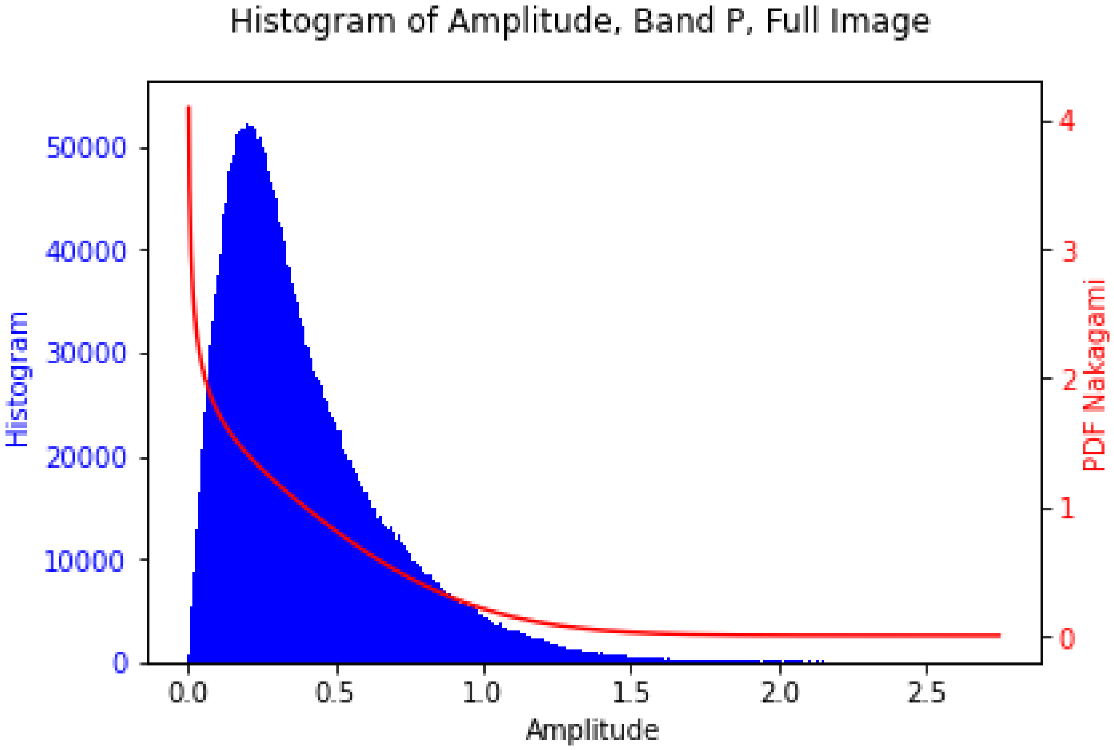

Histogram of Amplitude & Nakagami PDF Comparison. Full Image. Band P

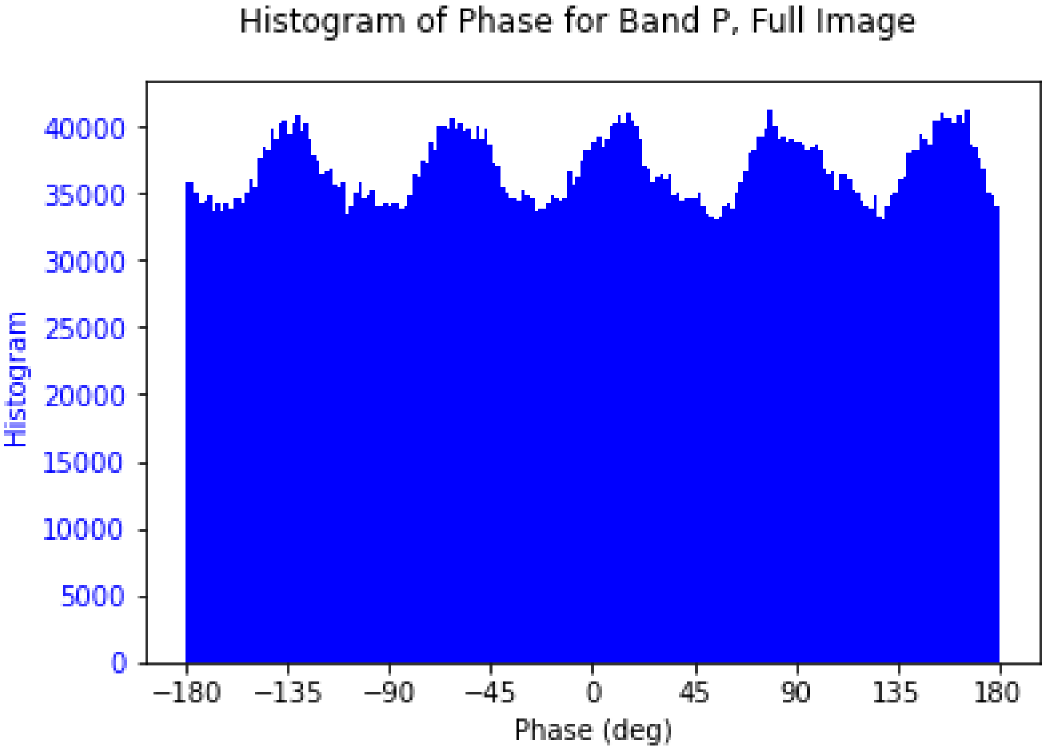

Histogram of Phase. Full Image. Band P

3.1.2. Close up to the Reference Points

Here are shown the histograms obtained from using the pixels surrounding the reflectors from all images at each band. Two windows of different size are used to get the pixels.

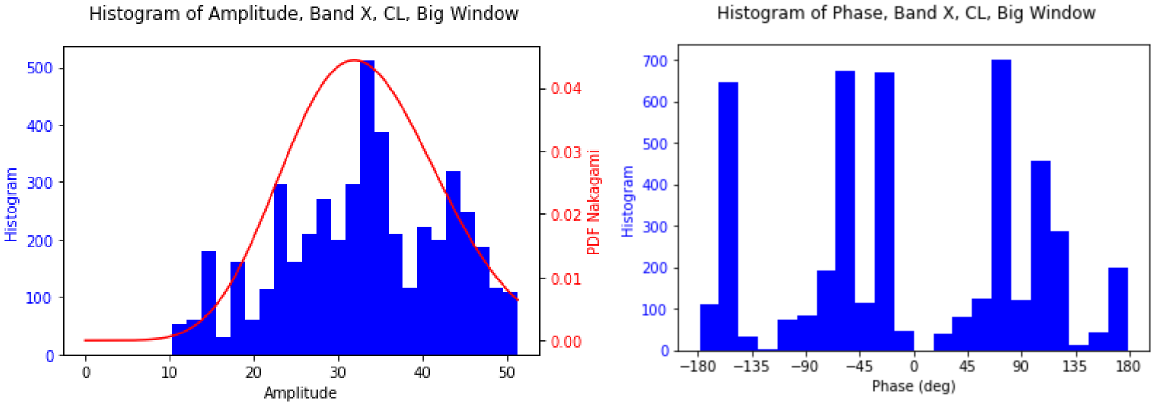

Histogram of Amplitude & Nakagami PDF Comparison. Histogram of Phase. Big Window. Corner Large. Band X

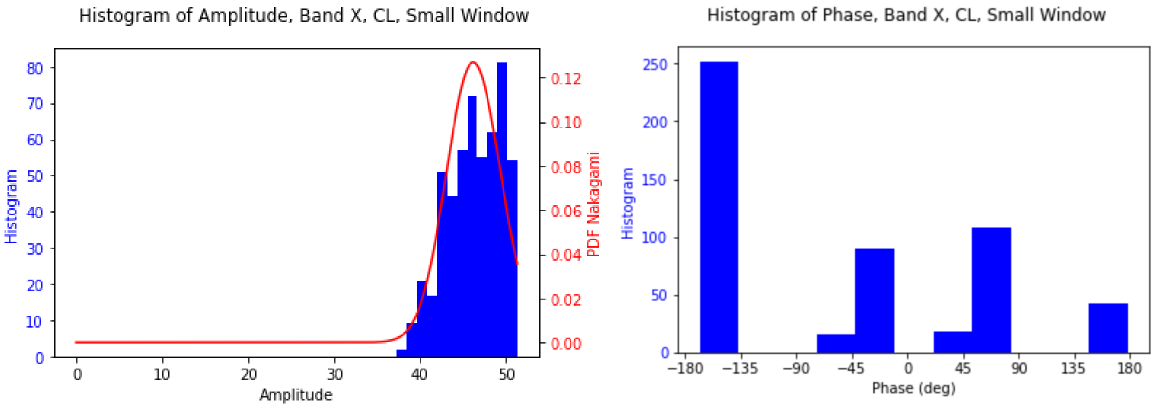

Histogram of Amplitude & Nakagami PDF Comparison. Histogram of Phase. Small Window. Corner Large. Band X

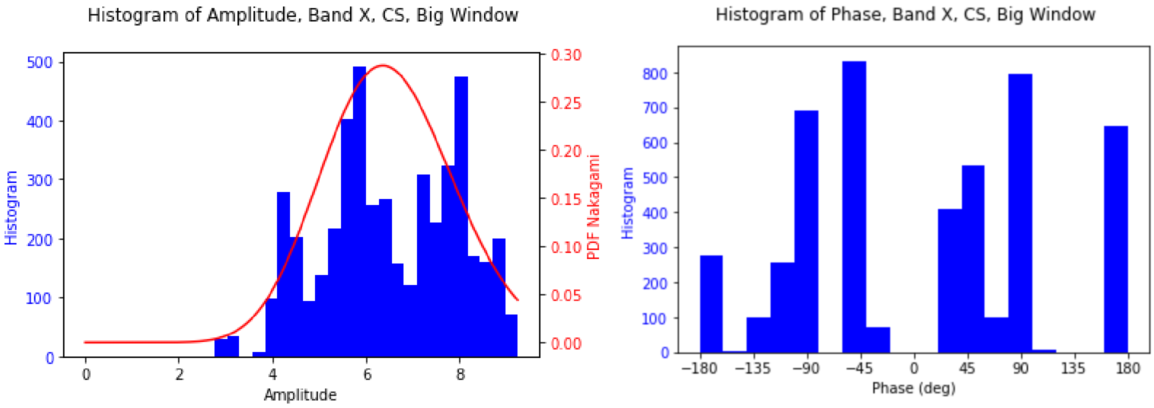

Histogram of Amplitude & Nakagami PDF Comparison. Histogram of Phase. Big Window. Corner Small. Band X

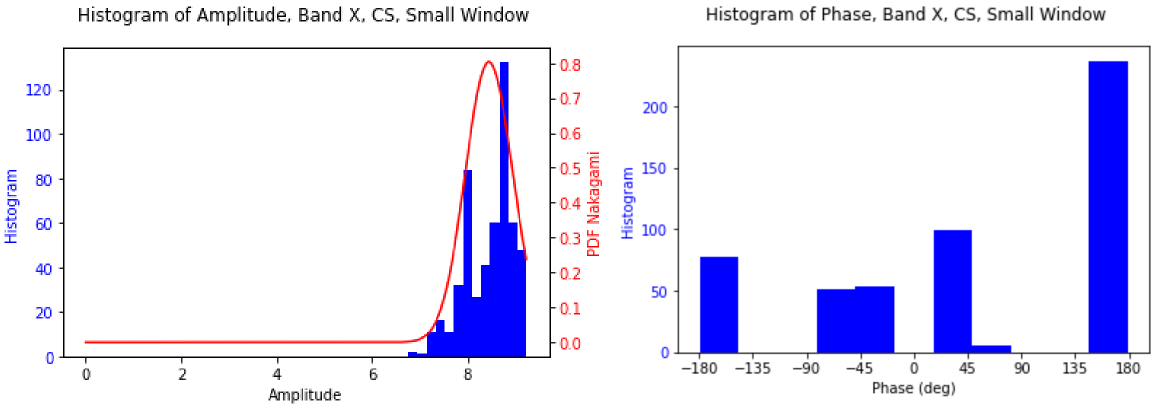

Histogram of Amplitude & Nakagami PDF Comparison. Histogram of Phase. Small Window. Corner Small. Band X

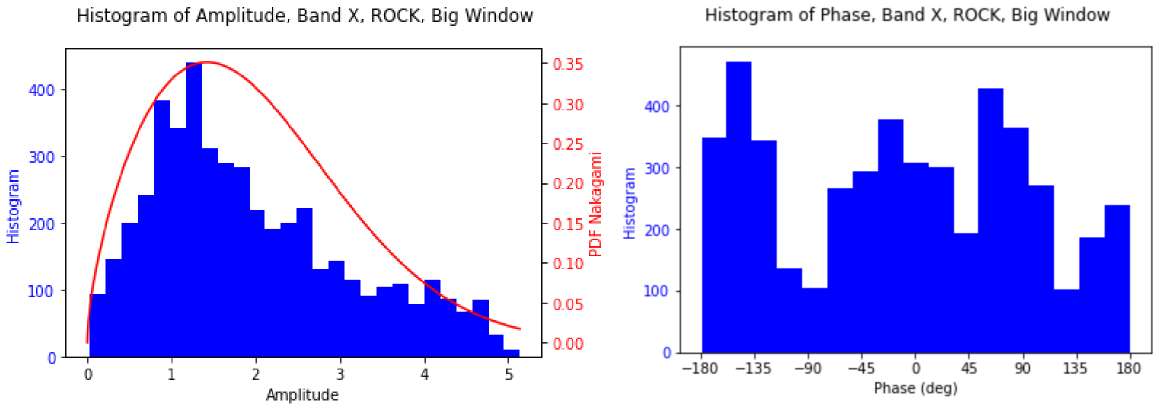

Histogram of Amplitude & Nakagami PDF Comparison. Histogram of Phase. Big Window. Rock. Band X

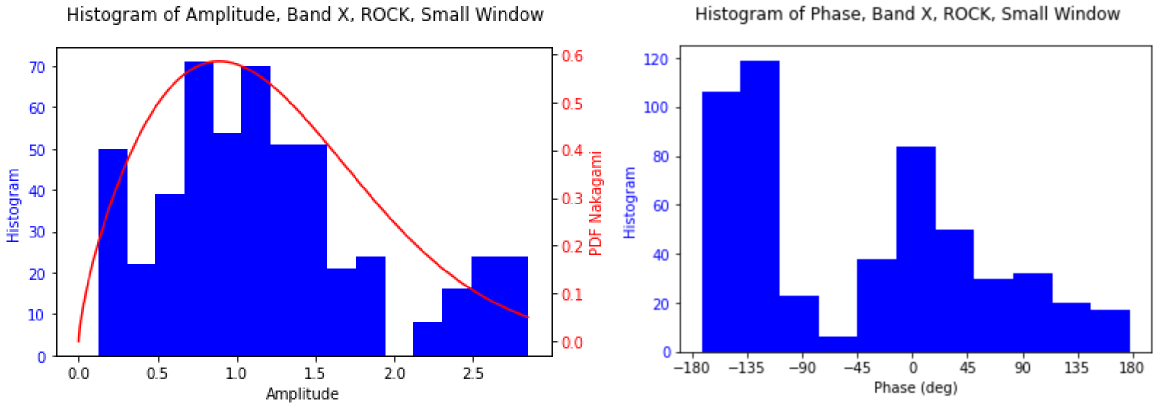

Histogram of Amplitude & Nakagami PDF Comparison. Histogram of Phase. Small Window. Rock. Band X

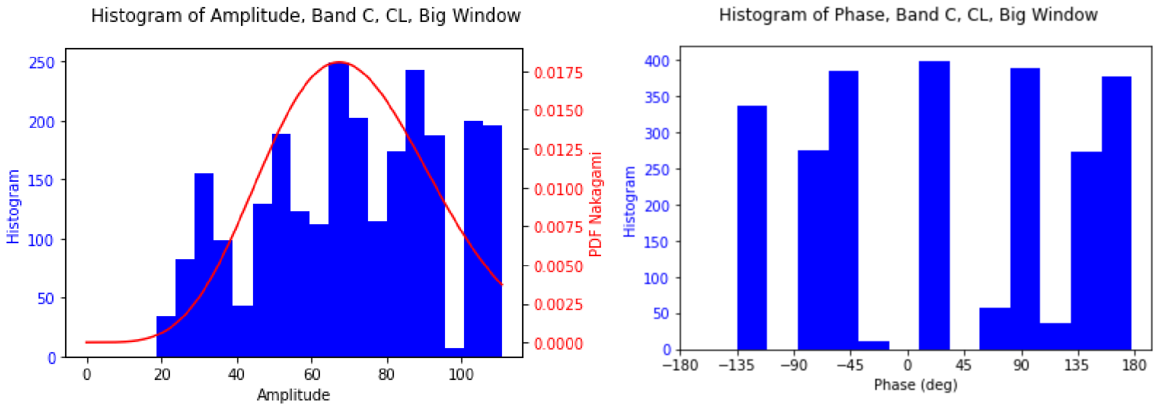

Histogram of Amplitude & Nakagami PDF Comparison. Histogram of Phase. Big Window. Corner Large. Band C

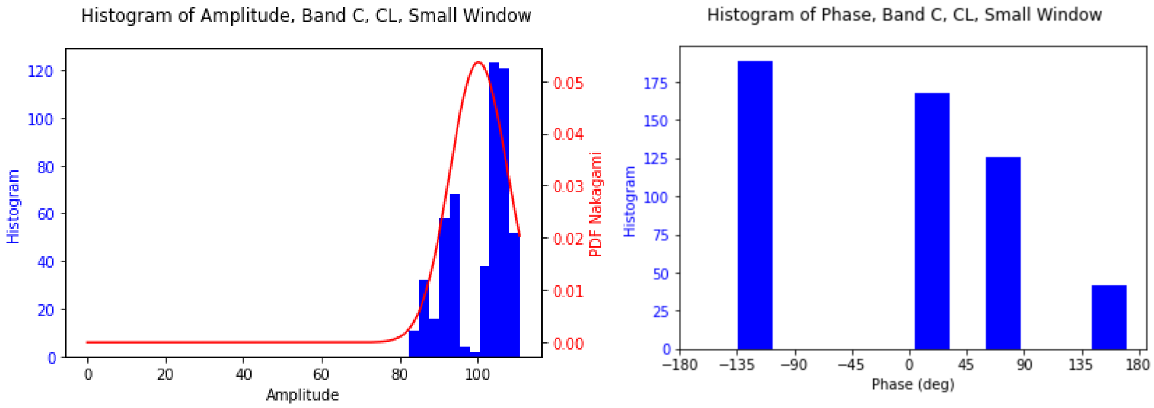

Histogram of Amplitude & Nakagami PDF Comparison. Histogram of Phase. Small Window. Corner Large. Band C

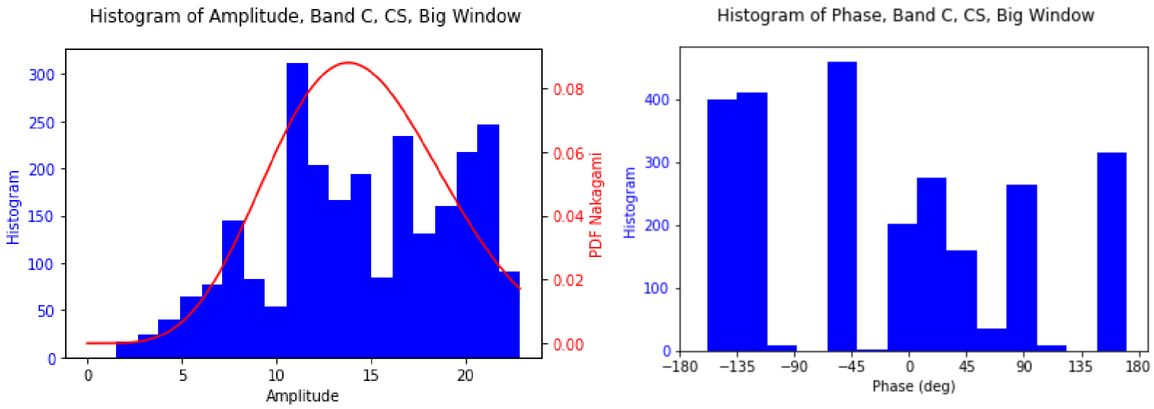

Histogram of Amplitude & Nakagami PDF Comparison. Histogram of Phase. Big Window. Corner Small. Band C

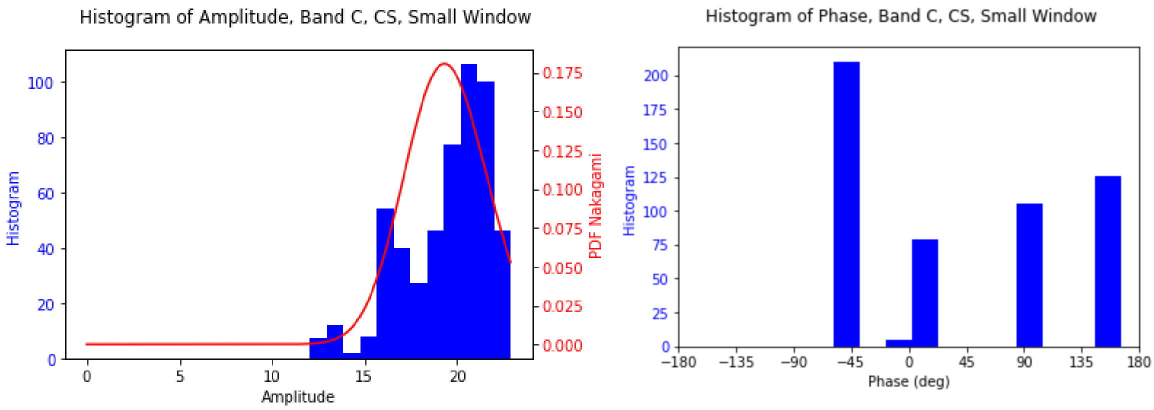

Histogram of Amplitude & Nakagami PDF Comparison. Histogram of Phase. Small Window. Corner Small. Band C

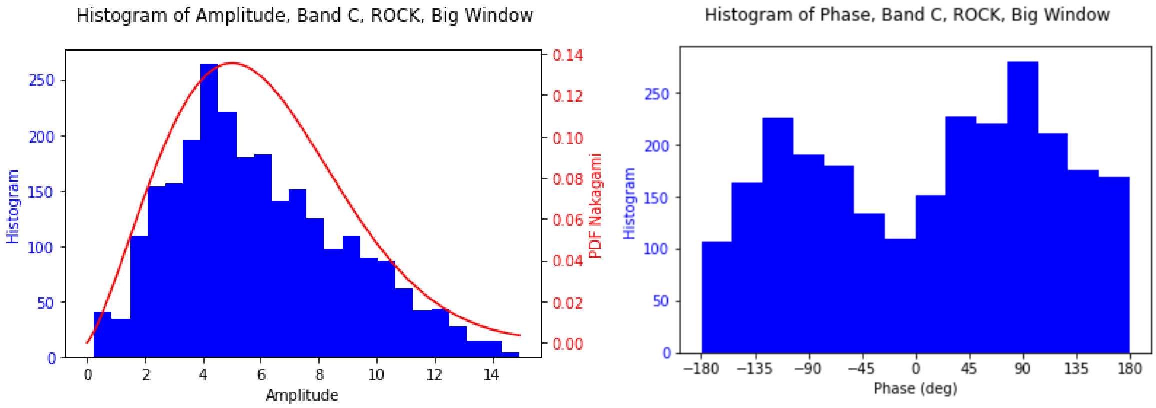

Histogram of Amplitude & Nakagami PDF Comparison. Histogram of Phase. Big Window. Rock. Band C

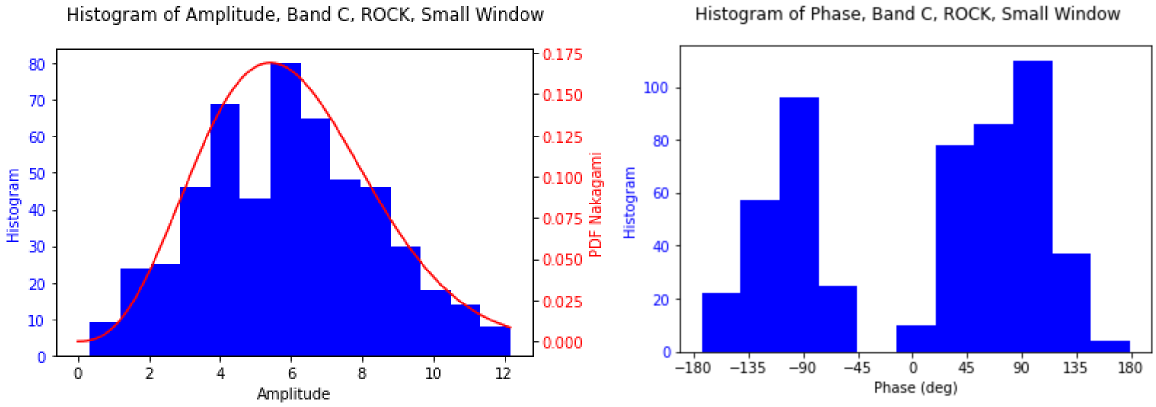

Histogram of Amplitude & Nakagami PDF Comparison. Histogram of Phase. Small Window. Rock. Band C

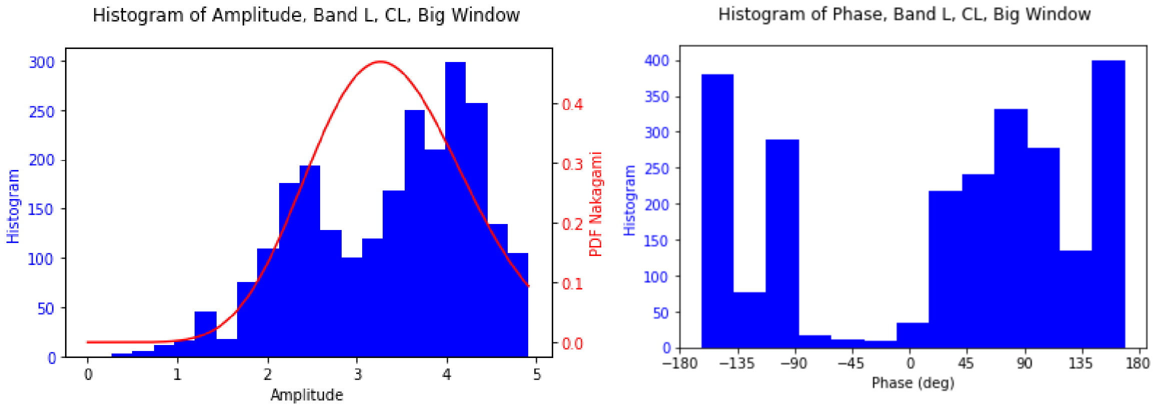

Histogram of Amplitude & Nakagami PDF Comparison. Histogram of Phase. Big Window. Corner Large. Band L

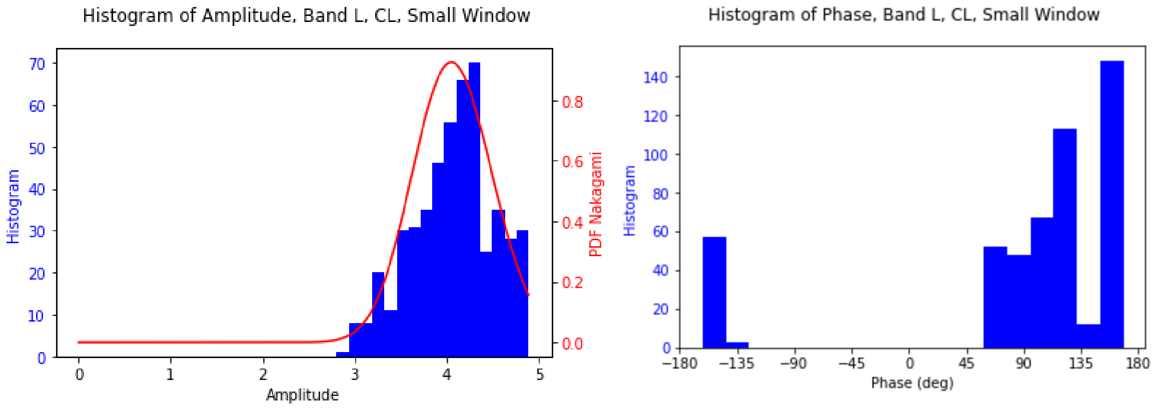

Histogram of Amplitude & Nakagami PDF Comparison. Histogram of Phase. Small Window. Corner Large. Band L

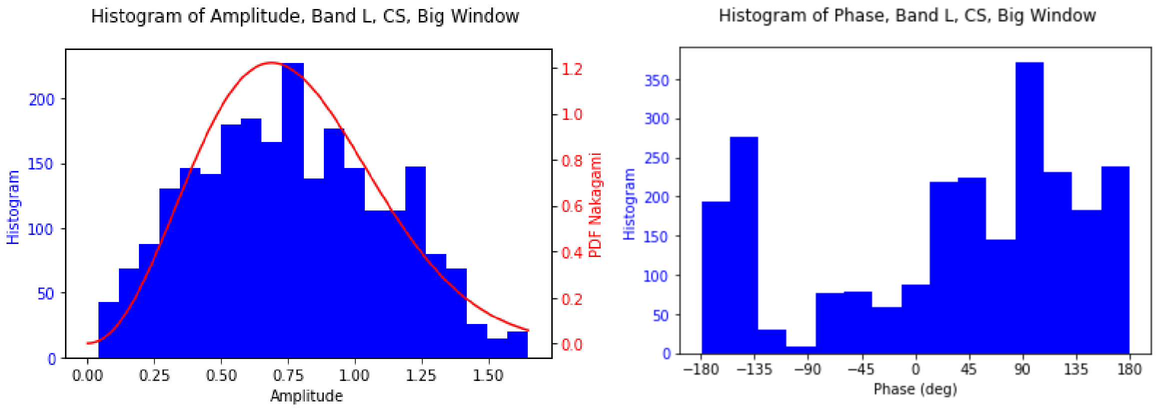

Histogram of Amplitude & Nakagami PDF Comparison. Histogram of Phase. Big Window. Corner Small. Band L

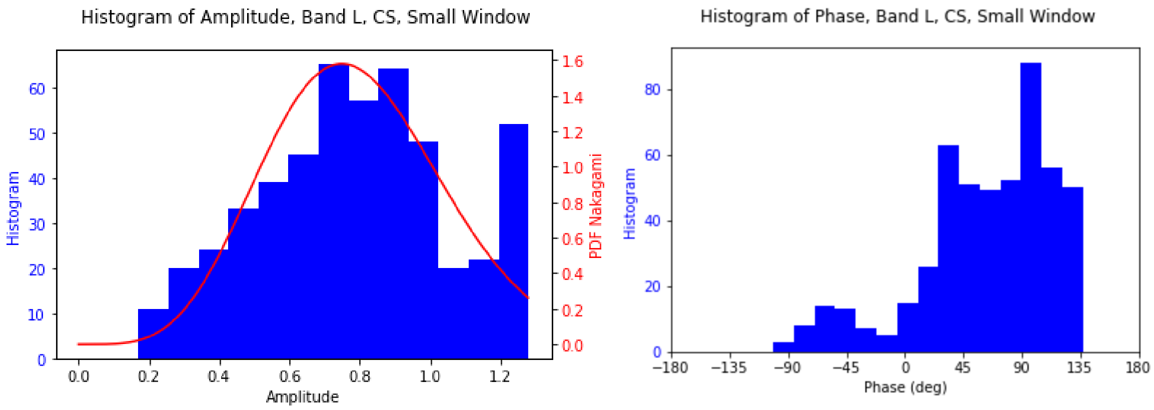

Histogram of Amplitude & Nakagami PDF Comparison. Histogram of Phase. Small Window. Corner Small. Band L

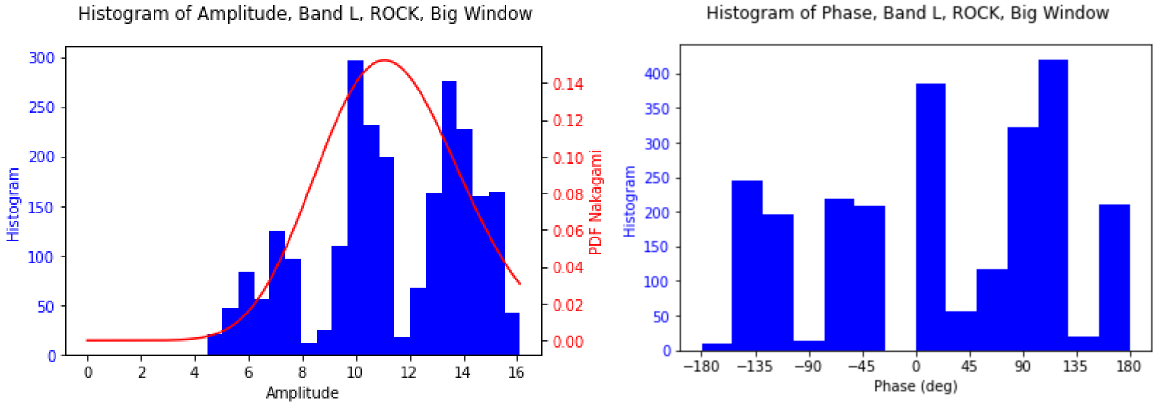

Histogram of Amplitude & Nakagami PDF Comparison. Histogram of Phase. Big Window. Rock. Band L

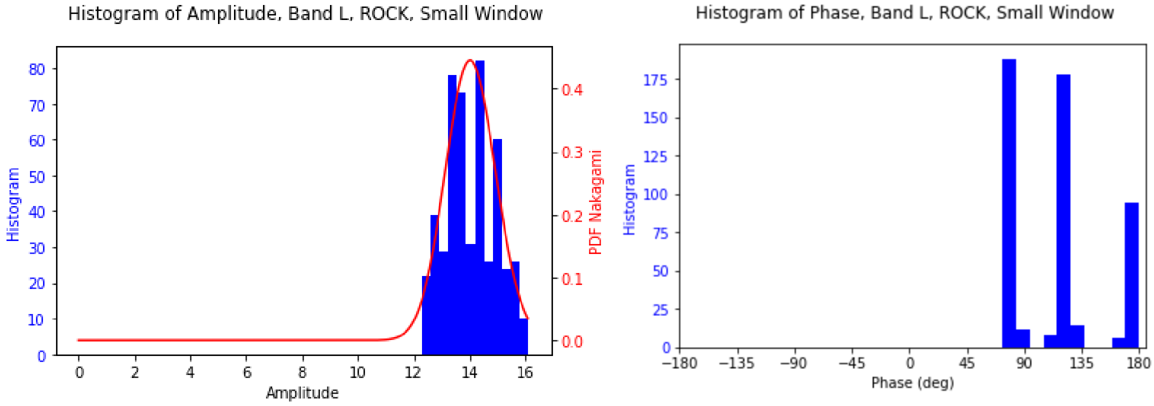

Histogram of Amplitude & Nakagami PDF Comparison. Histogram of Phase. Small Window. Rock. Band L

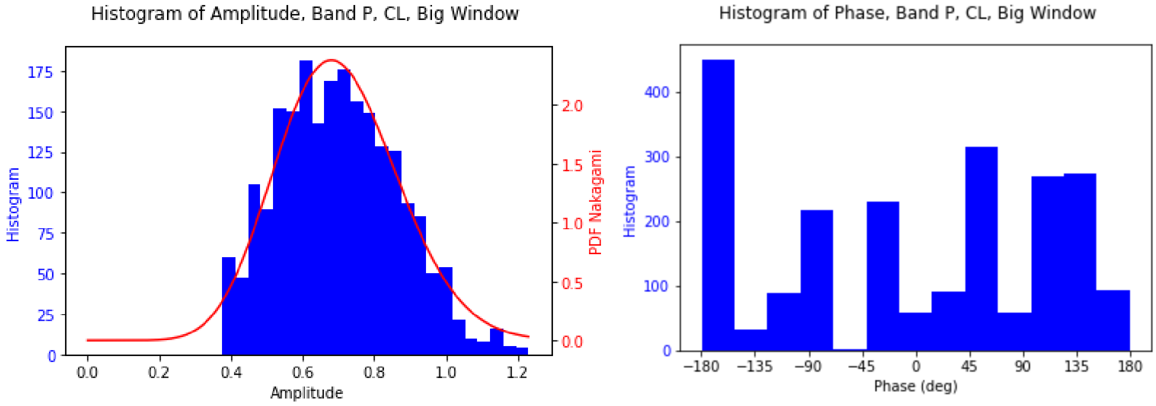

Histogram of Amplitude & Nakagami PDF Comparison. Histogram of Phase. Big Window. Corner Large. Band P

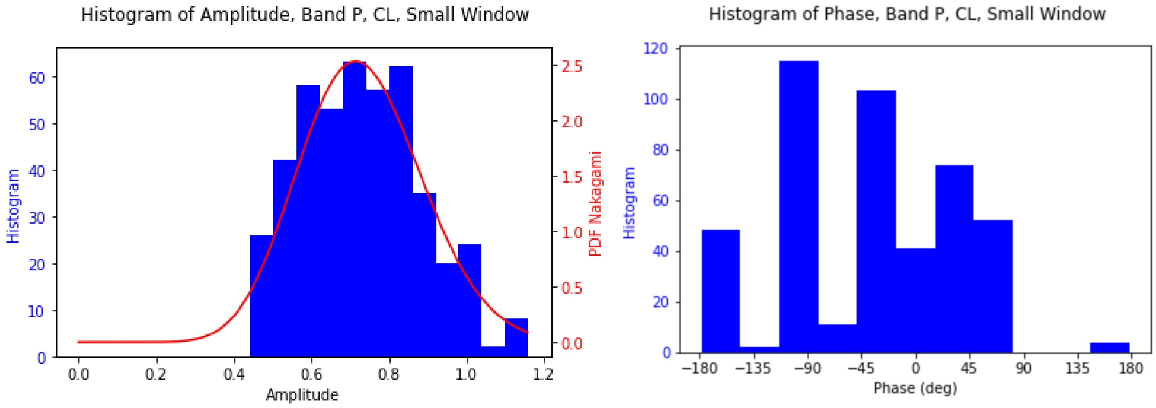

Histogram of Amplitude & Nakagami PDF Comparison. Histogram of Phase. Small Window. Corner Large. Band P

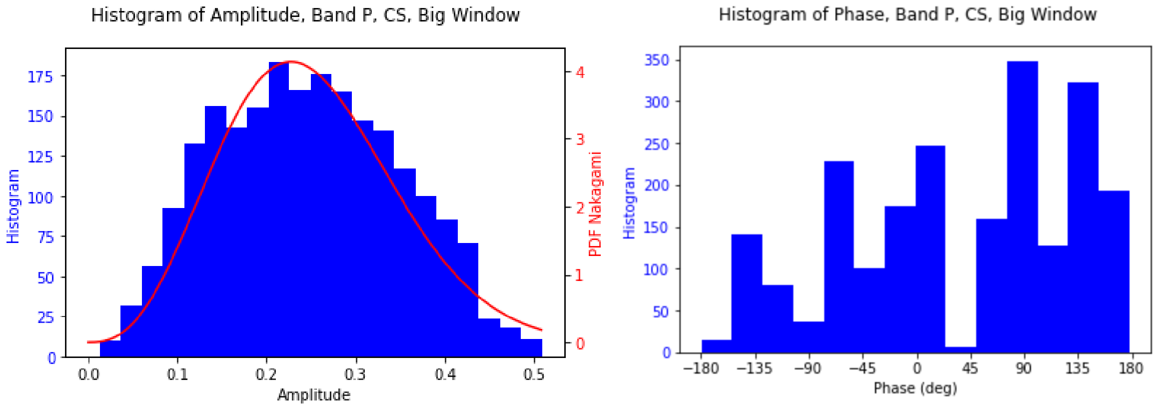

Histogram of Amplitude & Nakagami PDF Comparison. Histogram of Phase. Big Window. Corner Small. Band P

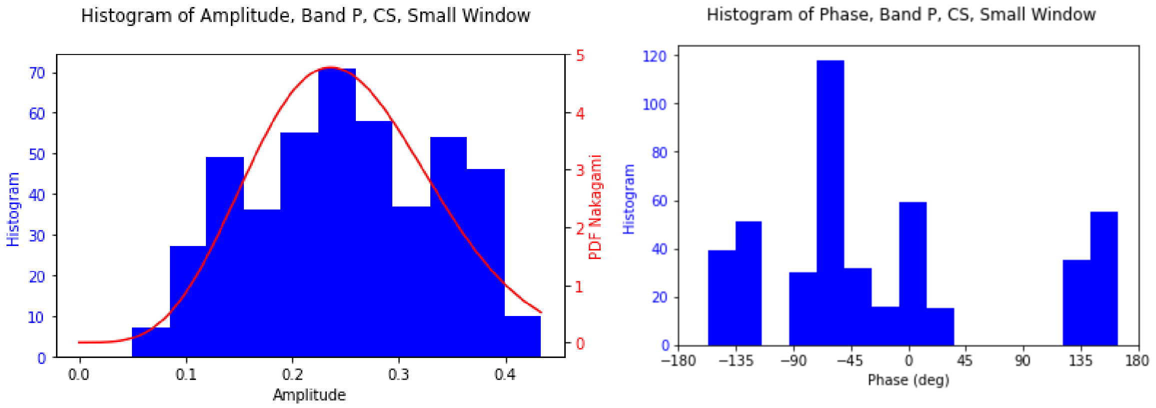

Histogram of Amplitude & Nakagami PDF Comparison. Histogram of Phase. Small Window. Corner Small. Band P

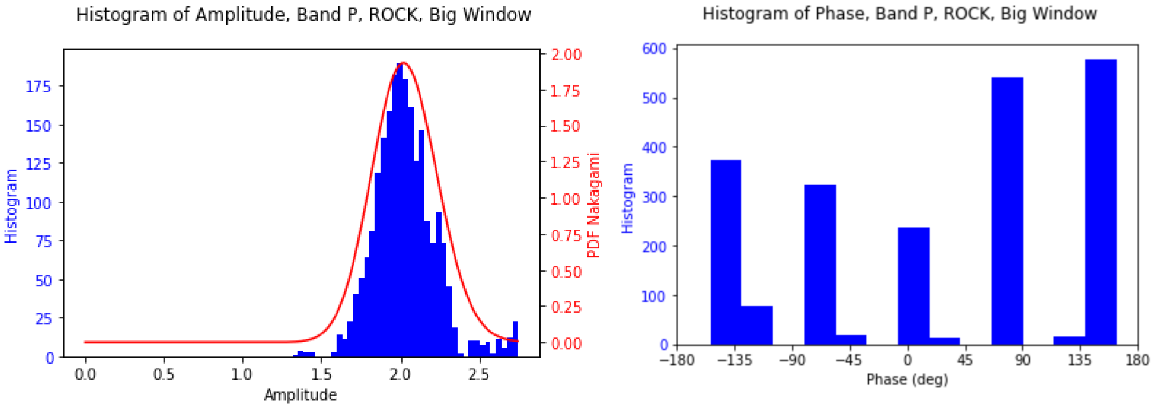

Histogram of Amplitude & Nakagami PDF Comparison. Histogram of Phase. Big Window. Rock. Band P

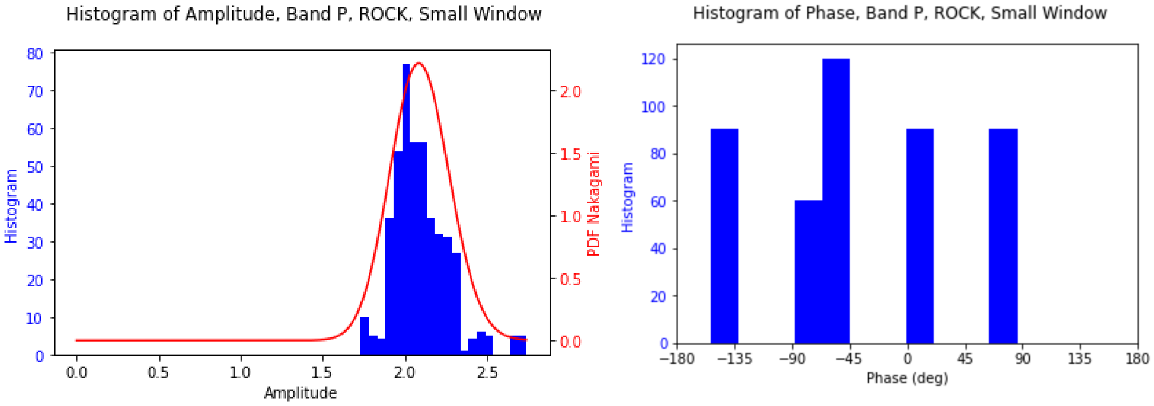

Histogram of Amplitude & Nakagami PDF Comparison. Histogram of Phase. Small Window. Rock. Band P

3.2. Probability Parameters Temporal Evolution

In this section the figures show the Probability Density Function for each acquisition obtained from the pixels of the images and the temporal evolution of the parameters used to compute the PDFs.

3.2.1. Complete Images

Here are shown the PDFs computed from using all the pixels, except for the shadowed area just below the sensor, for each image at each band.

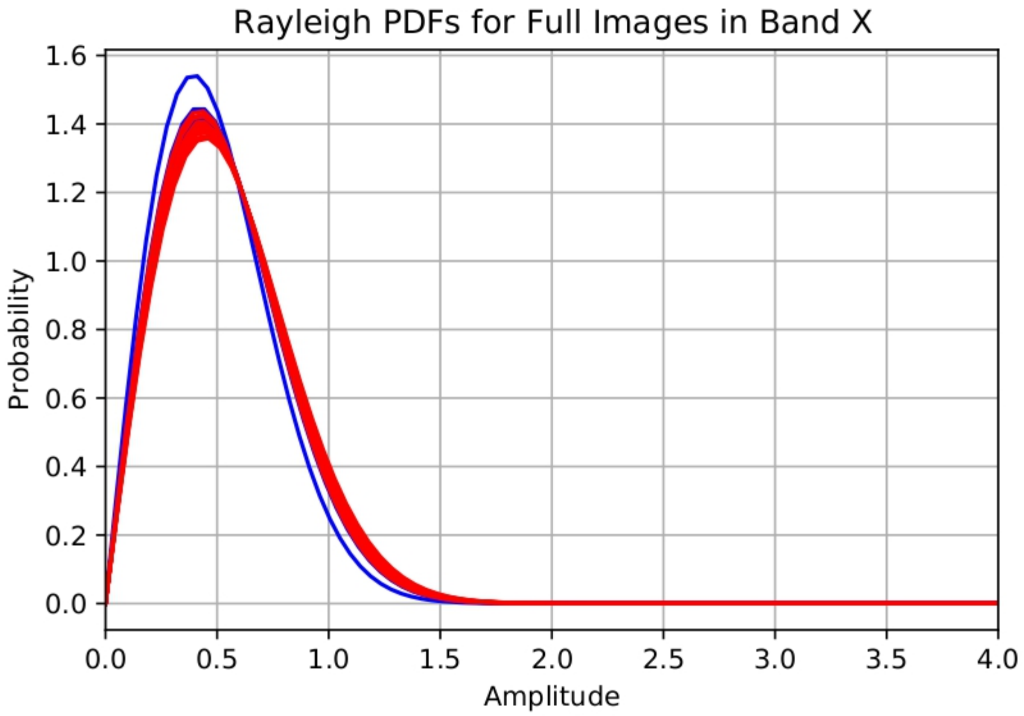

Rayleigh PDFs for each acquisition. Full Image. Band X

(acquisitions number 2, 12 & 17 plotted in colour blue)

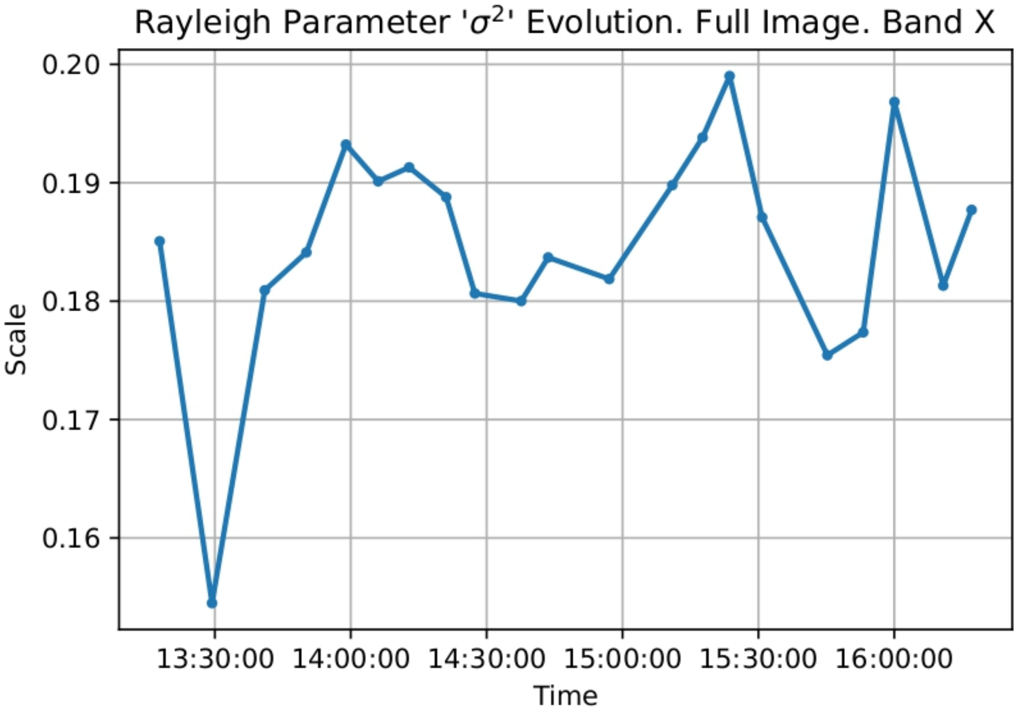

Rayleigh scale parameter 'σ^2' Evolution in Time. Full Image. Band X

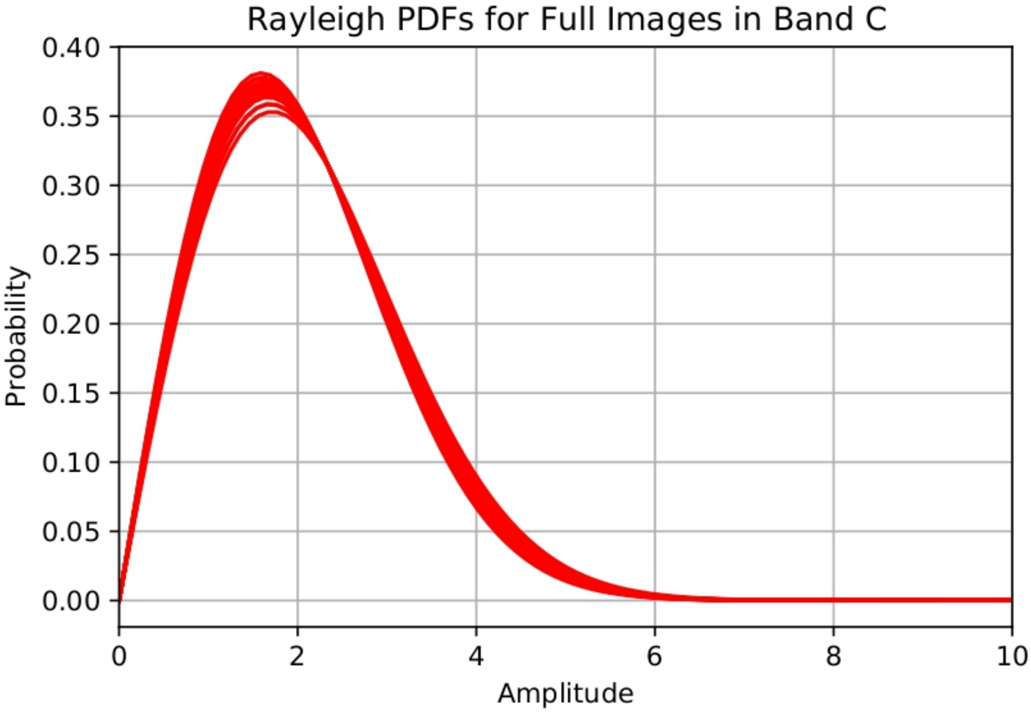

Rayleigh PDFs for each acquisition. Full Image. Band C

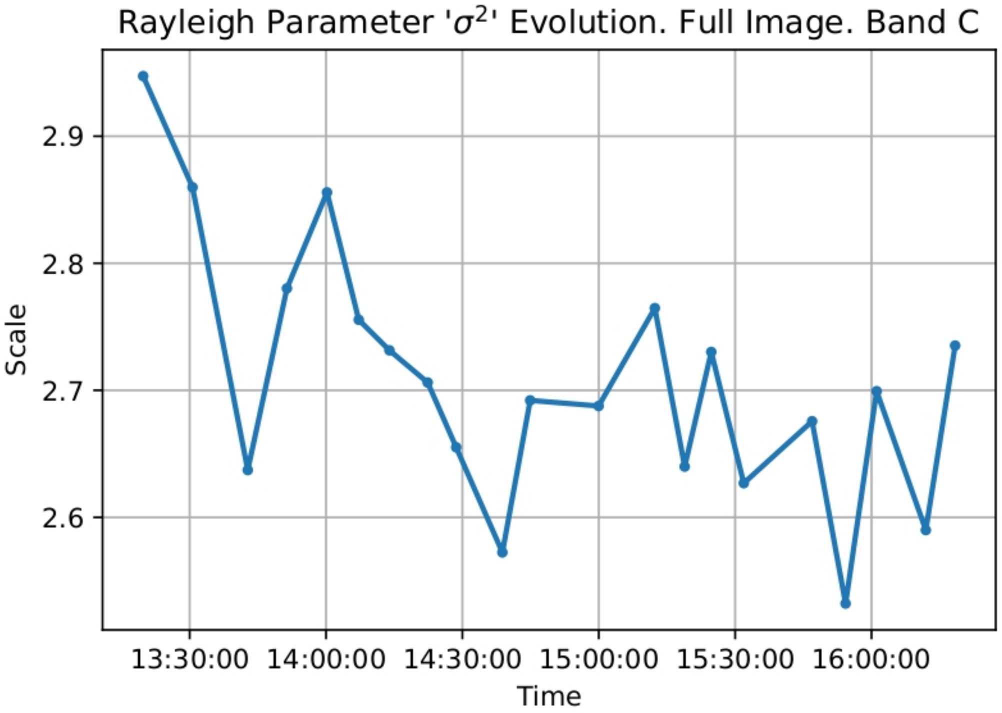

Rayleigh scale parameter ‘σ^2’ Evolution in Time. Full Image. Band C

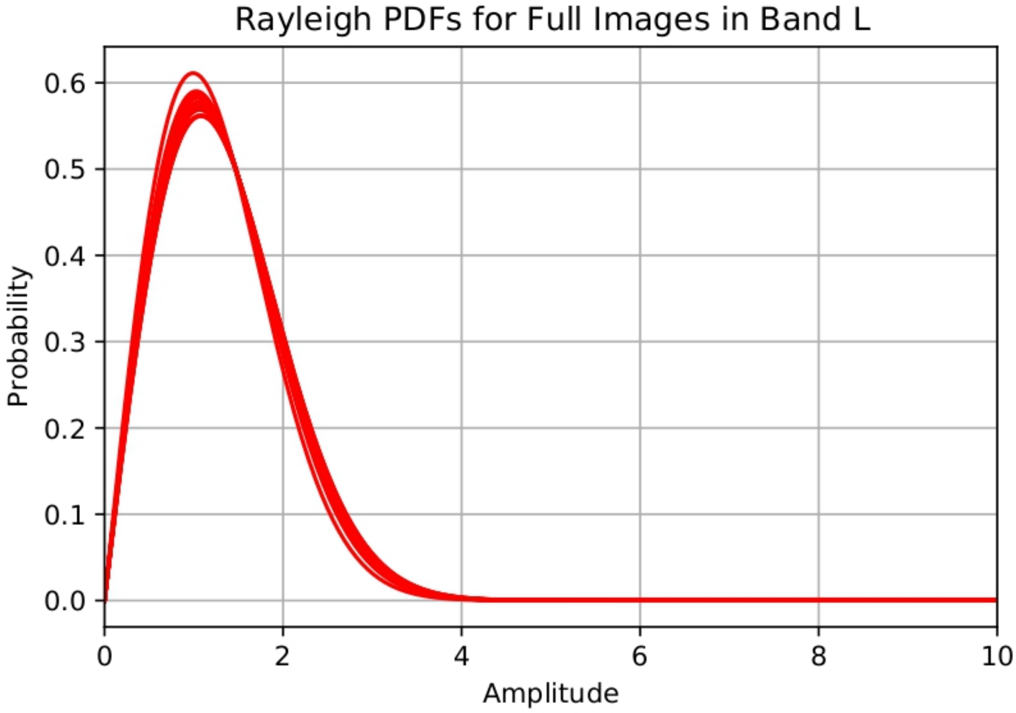

Rayleigh PDFs for each acquisition. Full Image. Band L

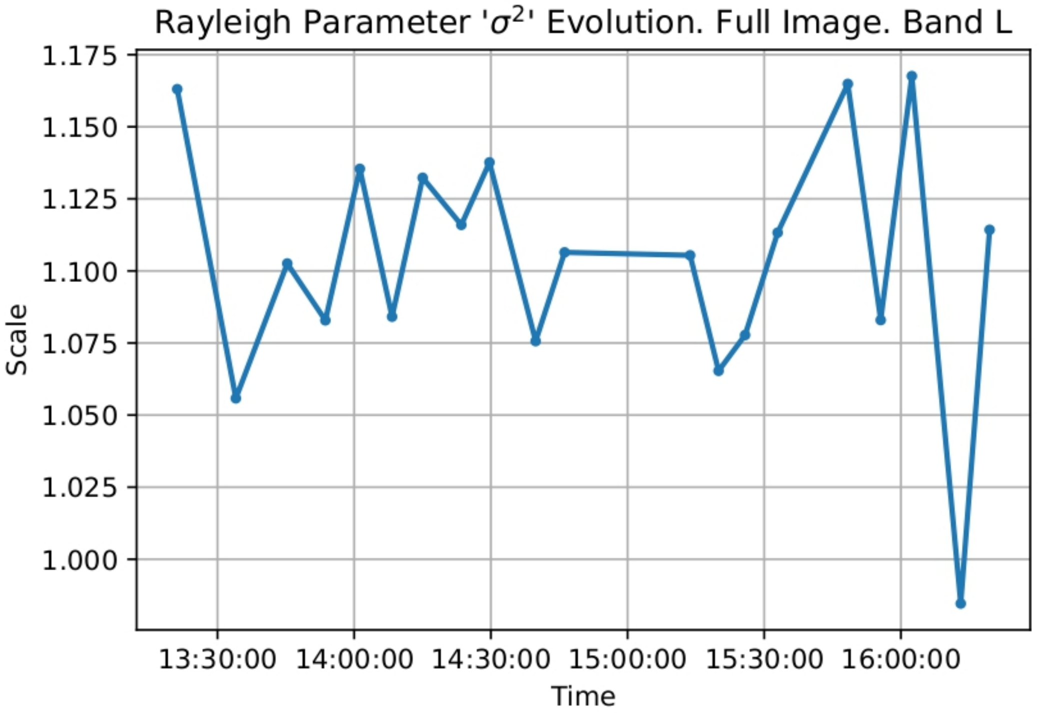

Rayleigh scale parameter 'σ^2' Evolution in Time. Full Image. Band L

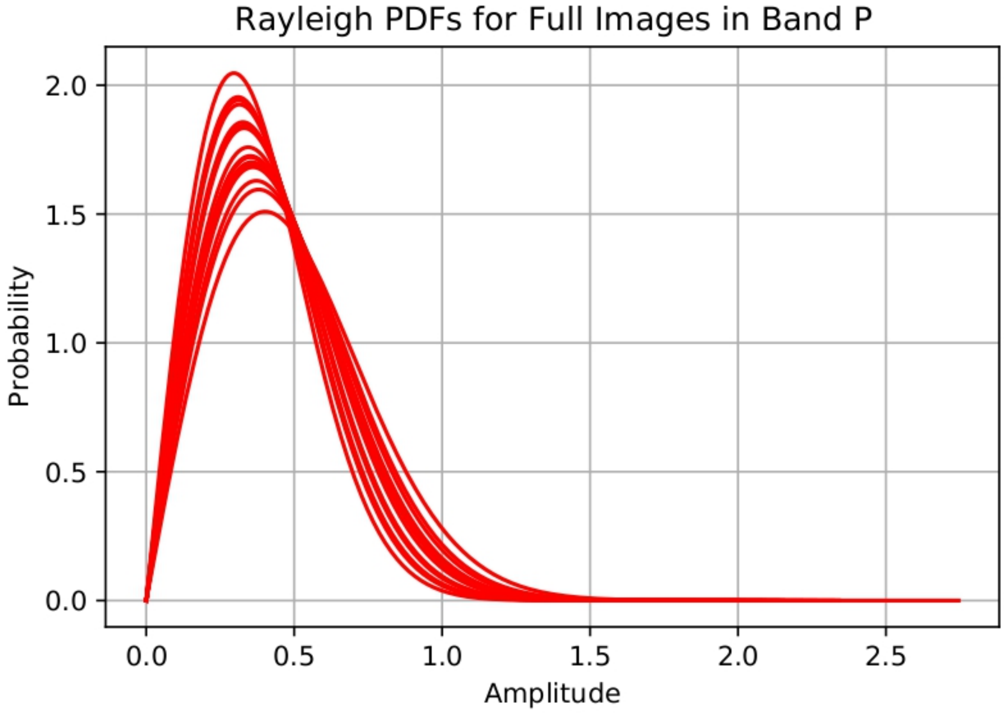

Rayleigh PDFs for each acquisition. Full Image. Band P

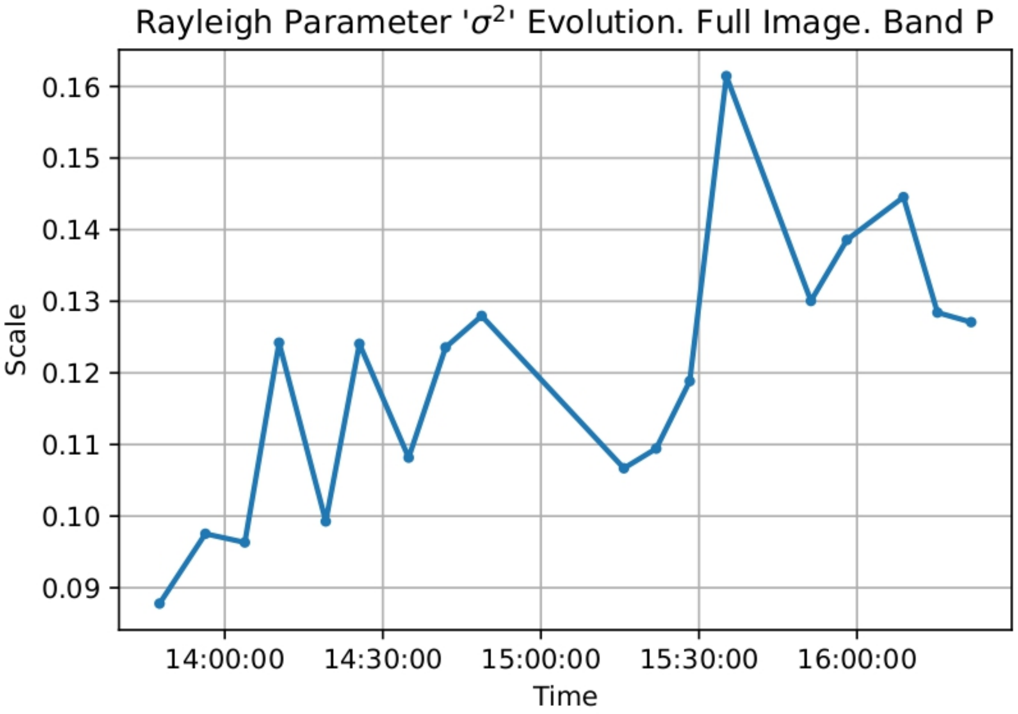

Rayleigh scale parameter ‘σ^2’ Evolution in Time. Full Image. Band P

3.2.2. Close up to the Reference Points

Here are shown the PDFs computed from using the pixels surrounding the reflectors for each image at each band. Here only the small window is used.

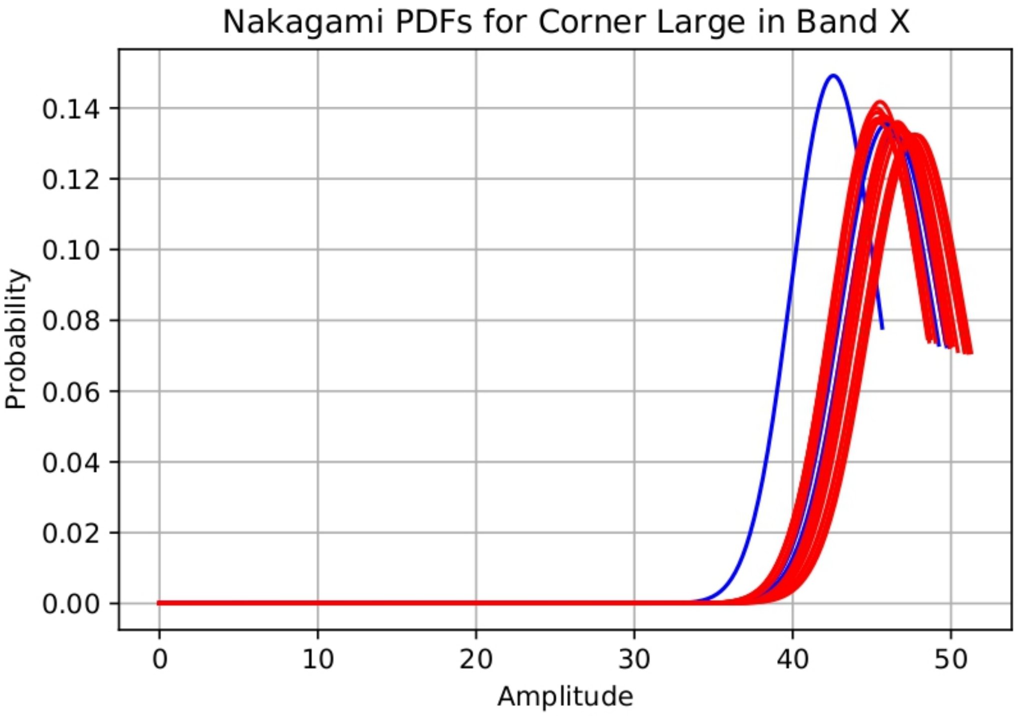

Nakagami PDFs for each acquisition. Corner Large. Band X

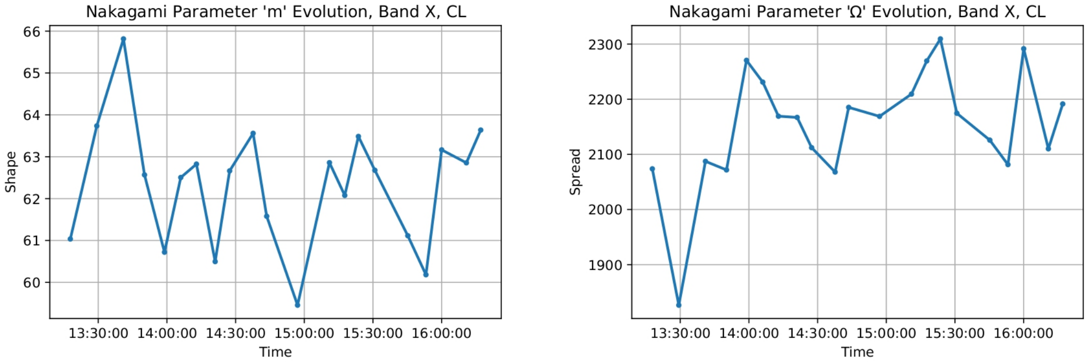

Nakagami parameters ‘m’ & ‘Ω’ Evolution in Time. Corner Large. Band X

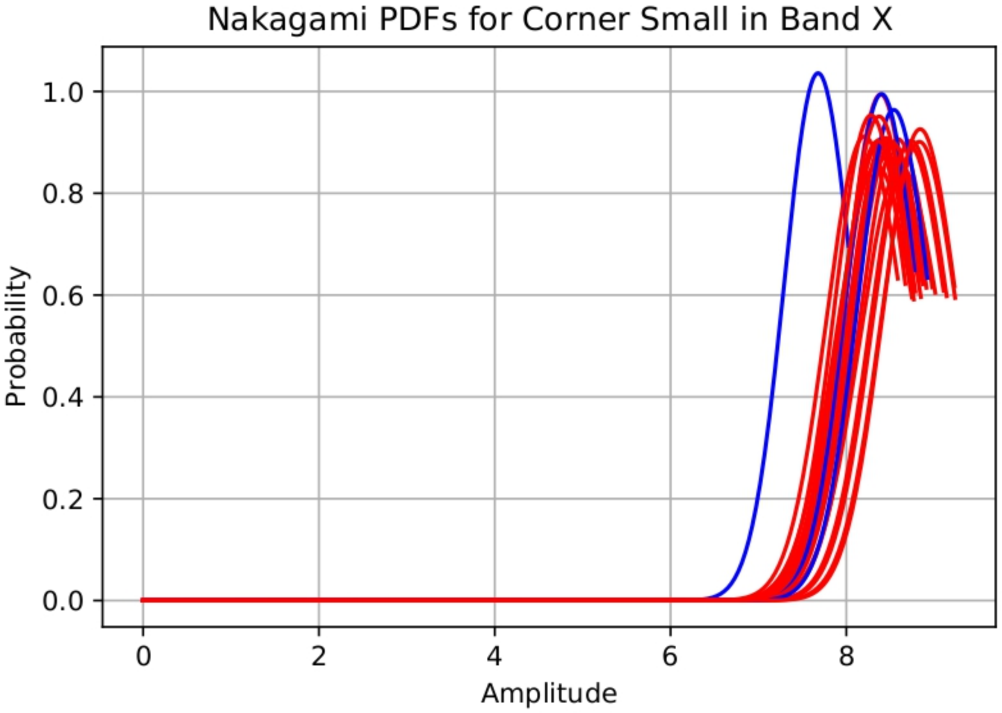

Nakagami PDFs for each acquisition. Corner Small. Band X

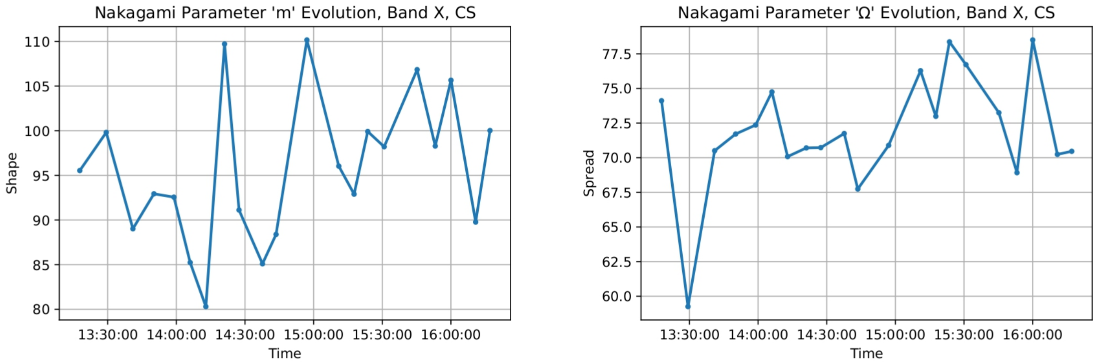

Nakagami parameters ‘m’ & ‘Ω’ Evolution in Time. Corner Small. Band X

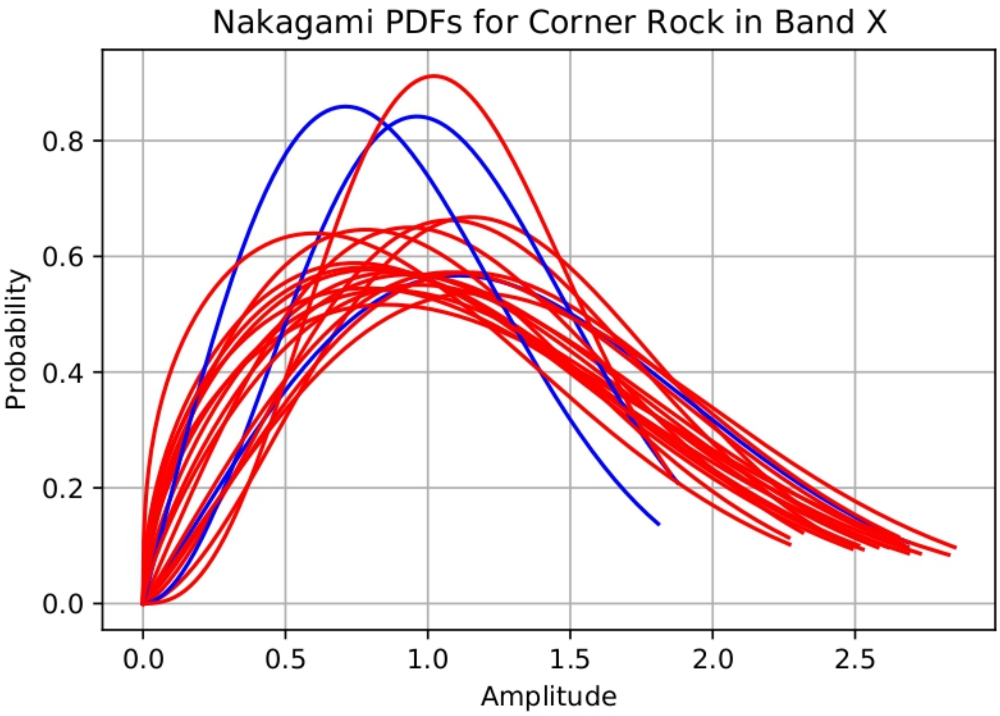

Nakagami PDFs for each acquisition. Rock. Band X

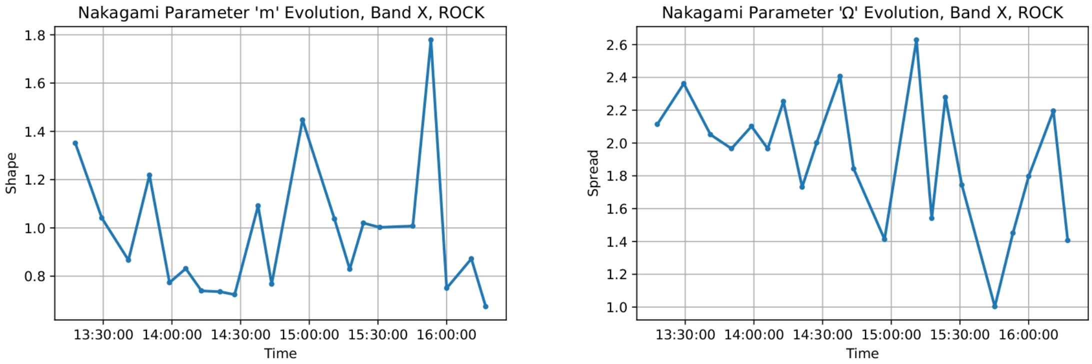

Nakagami parameters ‘m’ & ‘Ω’ Evolution in Time. Rock. Band X

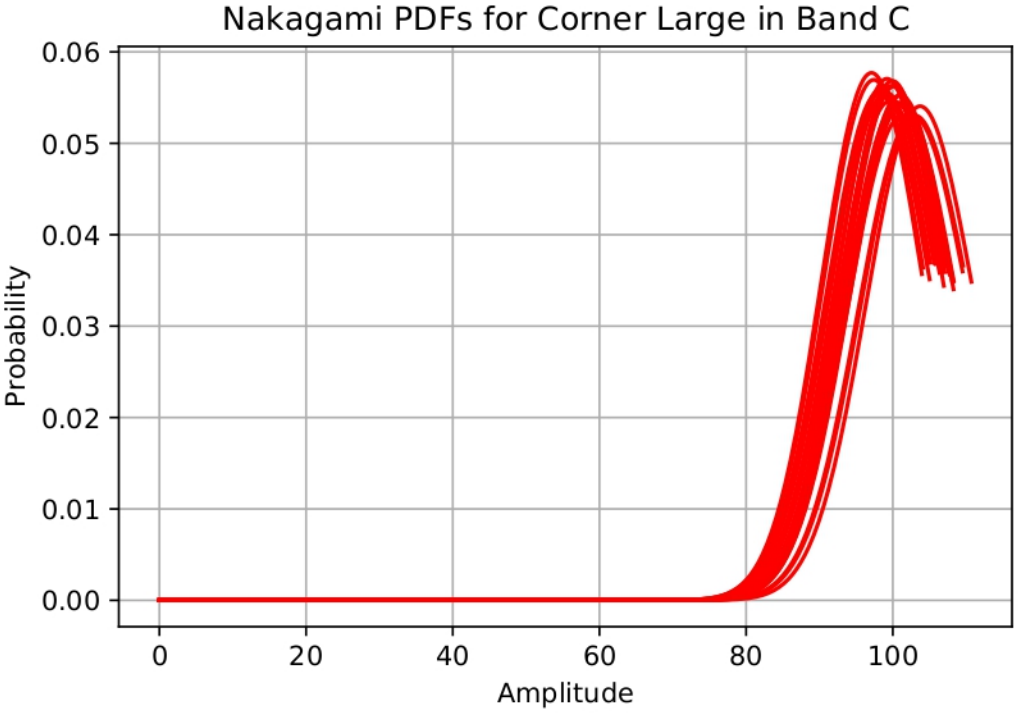

Nakagami PDFs for each acquisition. Corner Large. Band C

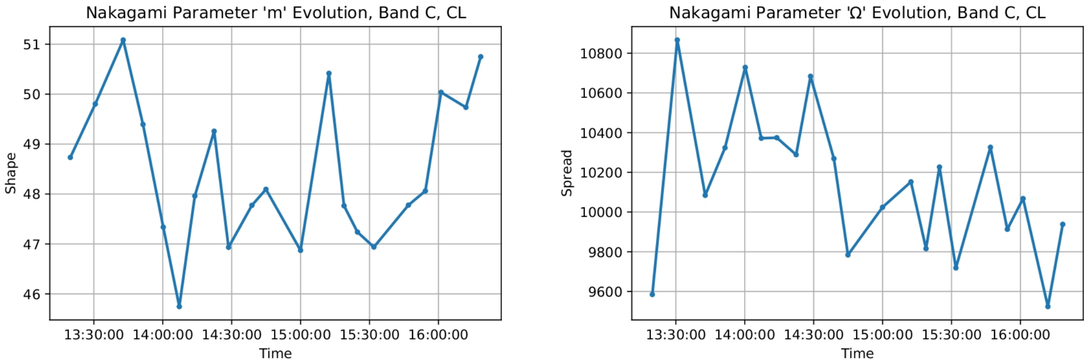

Nakagami parameters ‘m’ & ‘Ω’ Evolution in Time. Corner Large. Band C

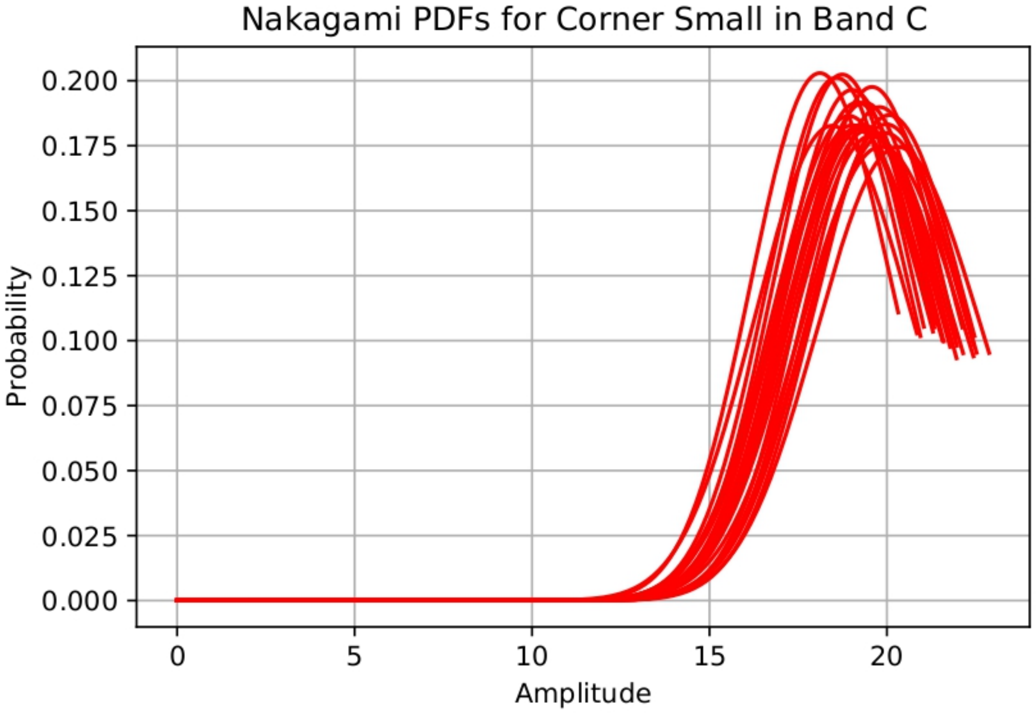

Nakagami PDFs for each acquisition. Corner Small. Band C

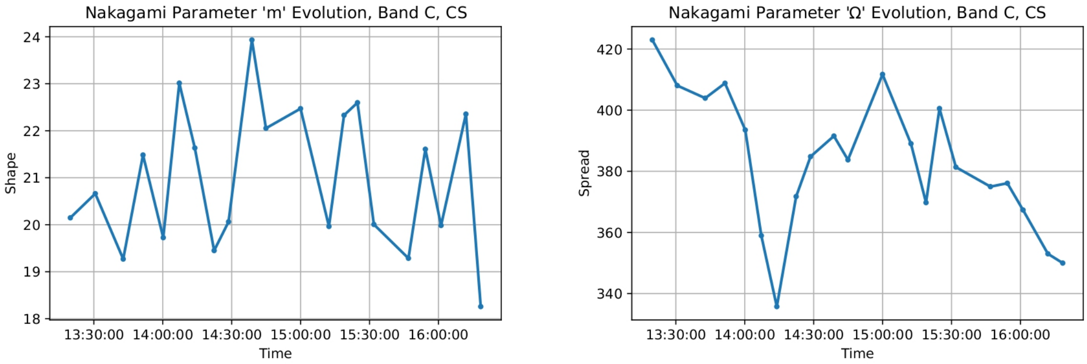

Nakagami parameters ‘m’ & ‘Ω’ Evolution in Time. Corner Small. Band C

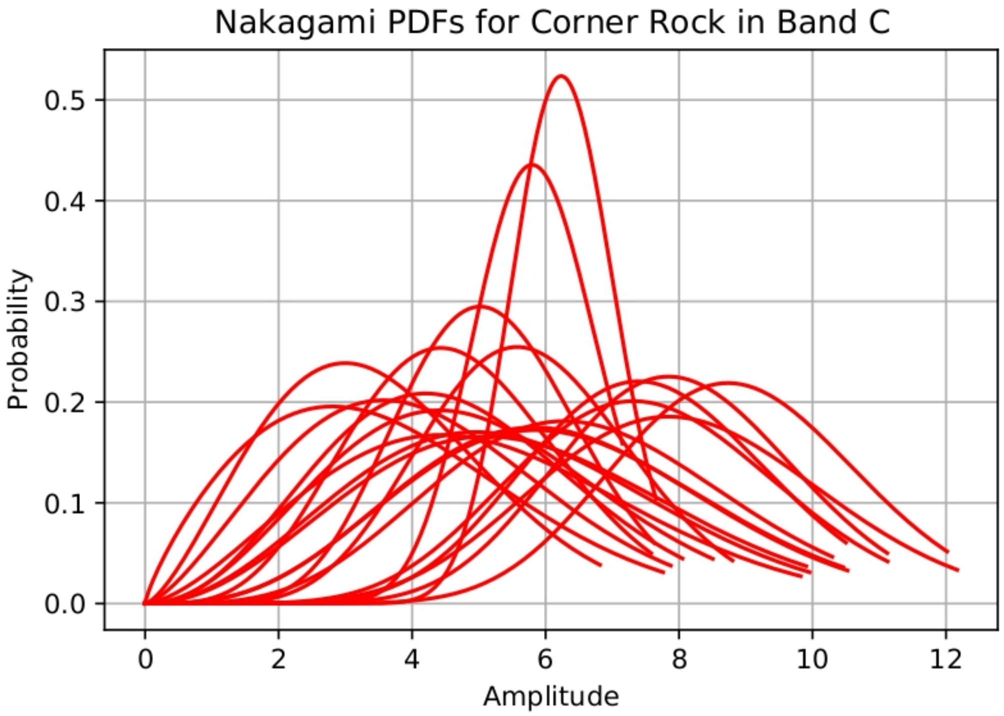

Nakagami PDFs for each acquisition. Rock. Band C

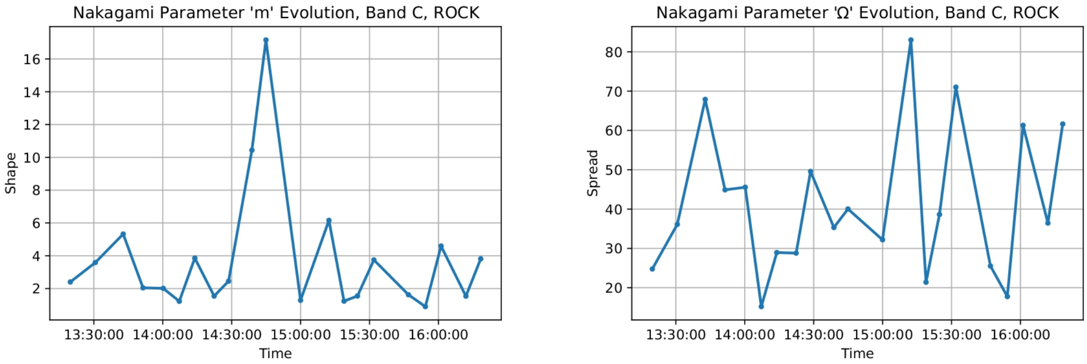

Nakagami parameters ‘m’ & ‘Ω’ Evolution in Time. Rock. Band C

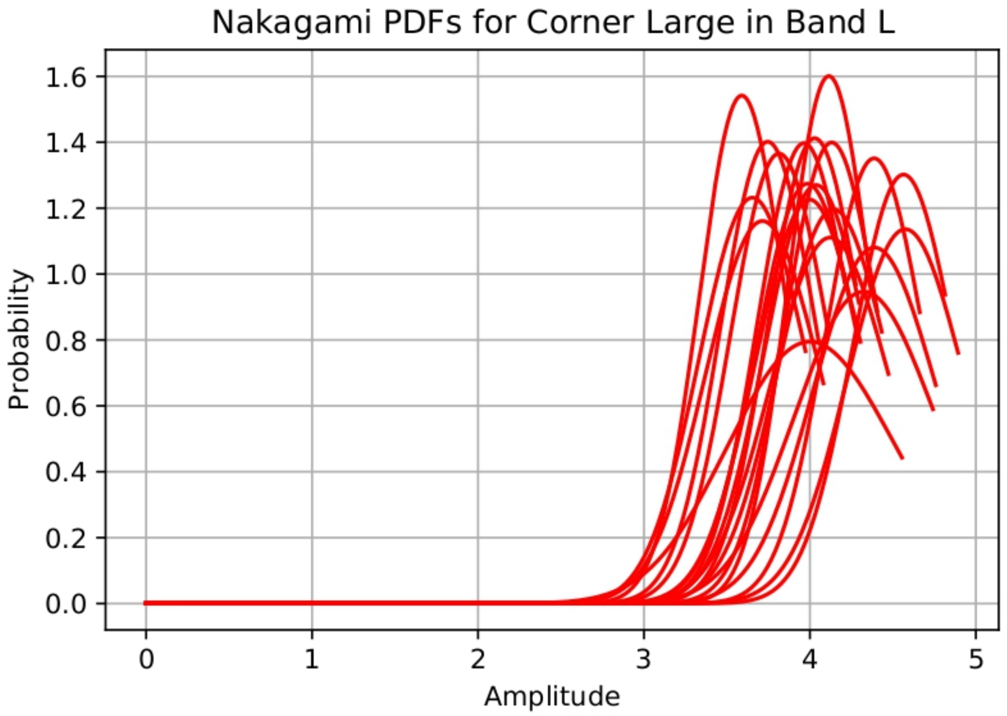

Nakagami PDFs for each acquisition. Corner Large. Band L

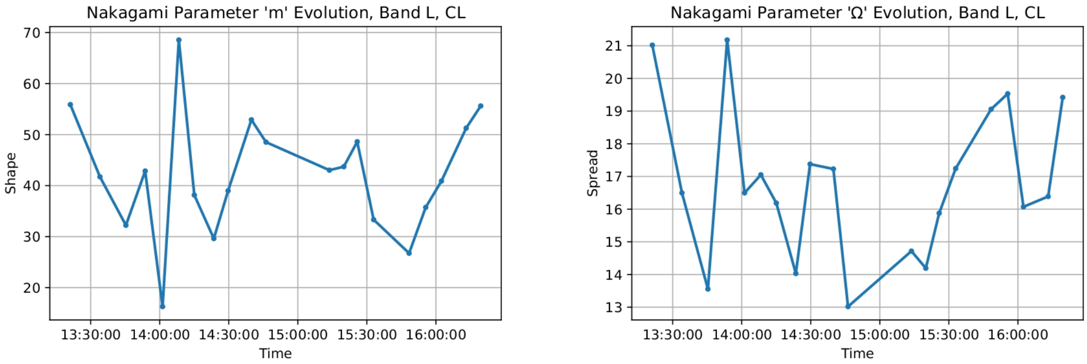

Nakagami parameters ‘m’ & ‘Ω’ Evolution in Time. Corner Large. Band L

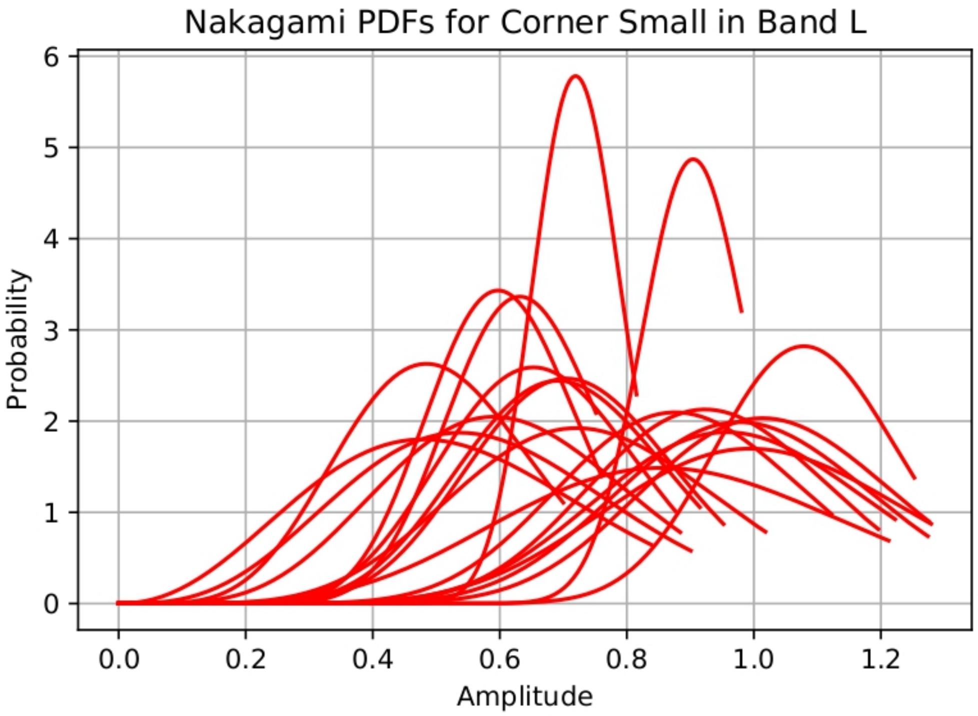

Nakagami PDFs for each acquisition. Corner Small. Band L

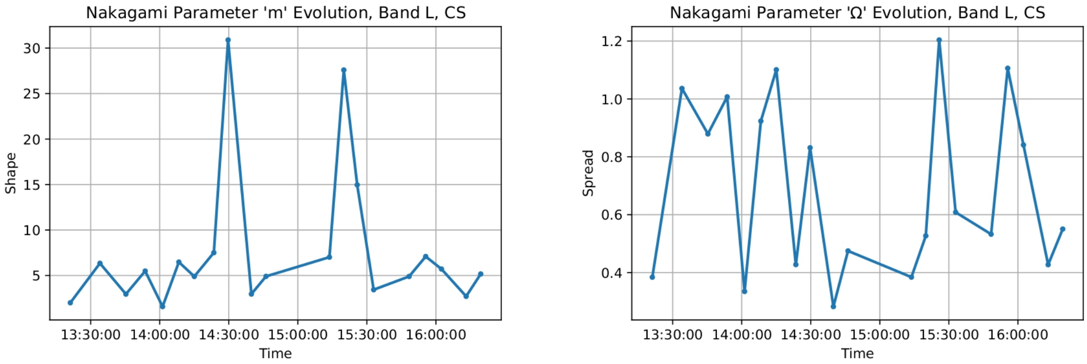

Nakagami parameters ‘m’ & ‘Ω’ Evolution in Time. Corner Small. Band L

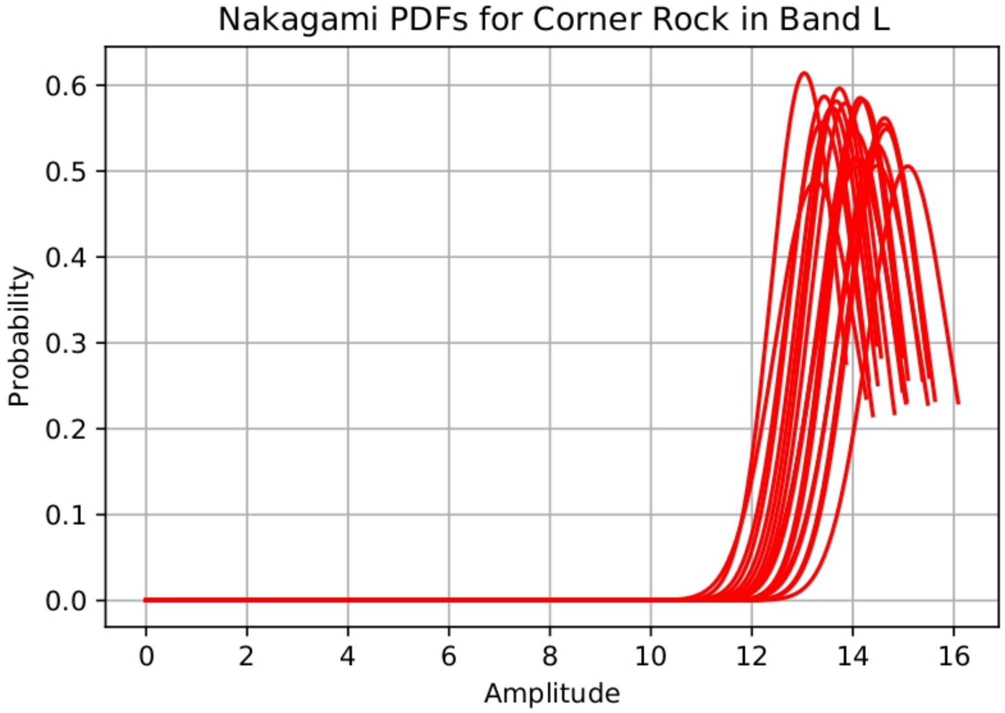

Nakagami PDFs for each acquisition. Rock. Band L

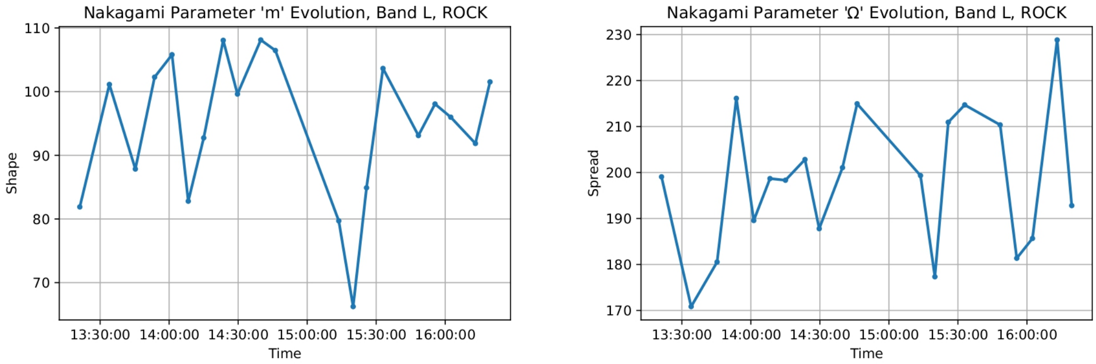

Nakagami parameters ‘m’ & ‘Ω’ Evolution in Time. Rock. Band L

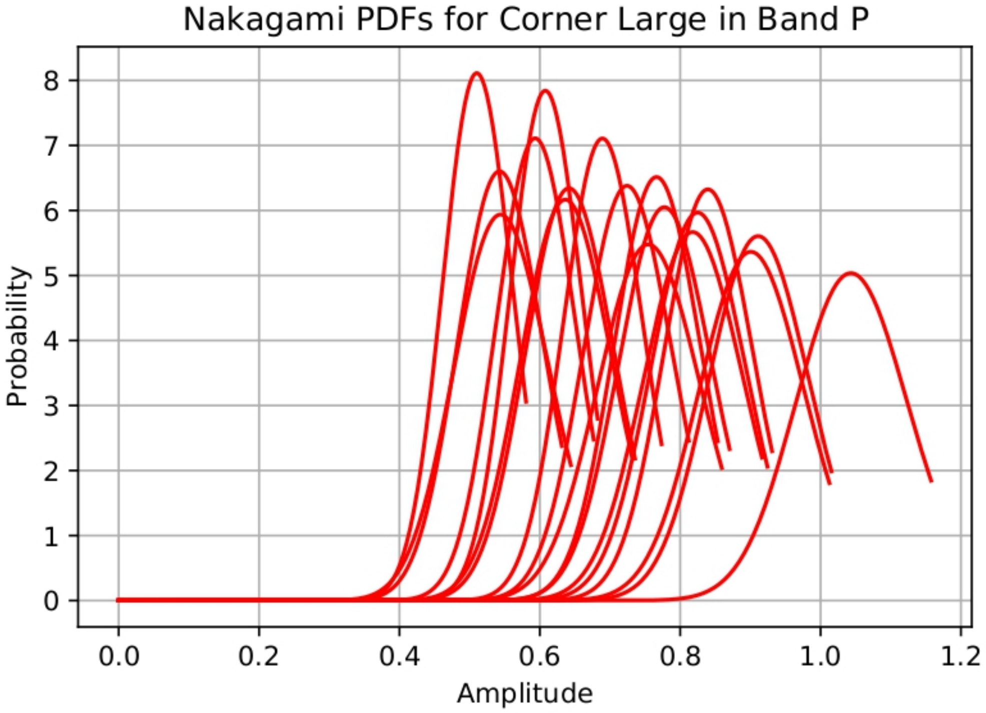

Nakagami PDFs for each acquisition. Corner Large. Band P

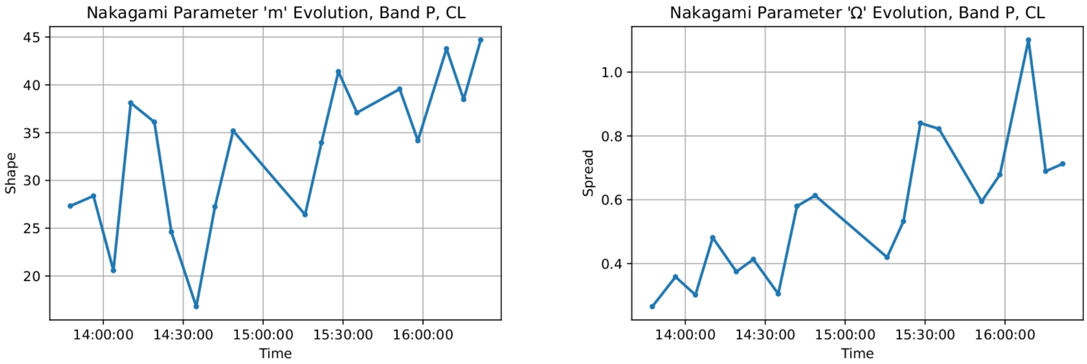

Nakagami parameters ‘m’ & ‘Ω’ Evolution in Time. Corner Large. Band P

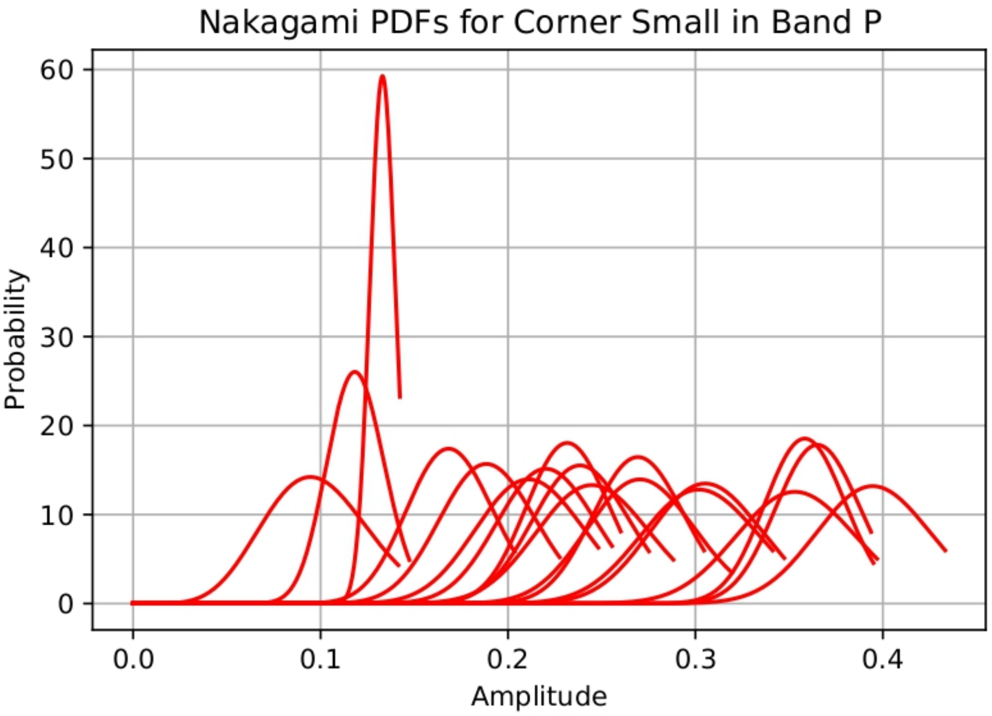

Nakagami PDFs for each acquisition. Corner Small. Band P

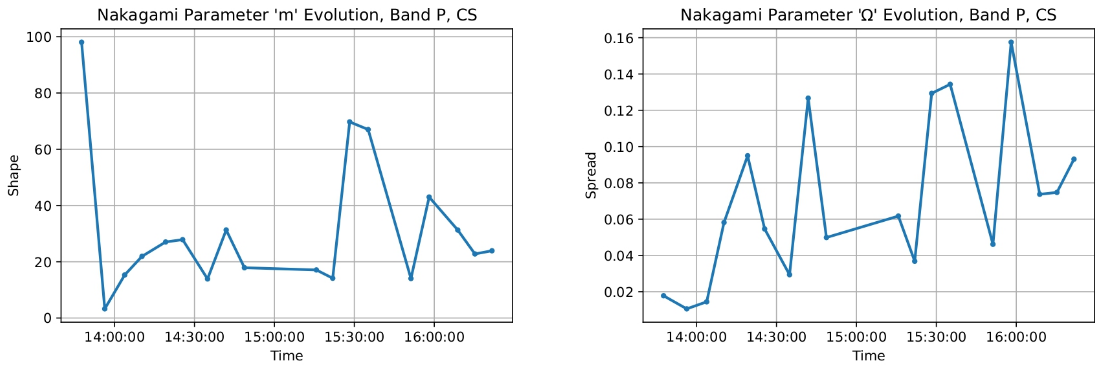

Nakagami parameters ‘m’ & ‘Ω’ Evolution in Time. Corner Small. Band P

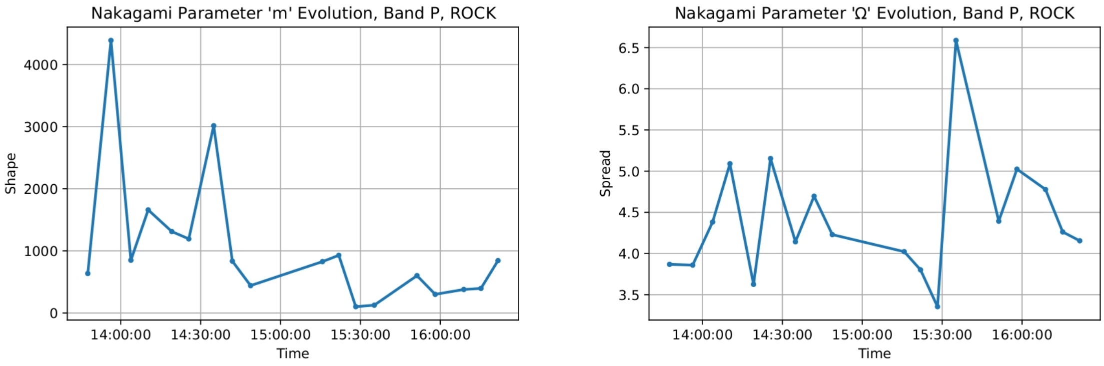

Nakagami parameters ‘m’ & ‘Ω’ Evolution in Time. Rock. Band P

Glossary

A list of all acronyms and the meaning they stand for:

CL Corner Large

CLT Central Limit Theorem

CS Corner Small

DEM Digital Elevation Model

ESA European Space Agency

FMCW Frequency Modulated Continuous Wave

GB-SAR Ground Based SAR

GPU Graphics Processing Unit

InSAR Interferometric SAR

INV Inverse Normalized Variance Estimator

MIMO Multiple Input Multiple Output

MLE Maximum Likelihood Estimator

PDF Probability Density Function

PolSAR Polarimetric SAR

RADAR Radio Detection And Ranging

RCS Radar Cross Section

ROCK Rock

Rx Receiver

SAR Synthetic Aperture Radar

SDR Software Defined Radio

SLC Single Look Complex

SSA Short Synthetic Aperture

TCR Trihedral Corner Reflectors

TSC Signal Theory and Communication Department of UPC

Tx Transmitter

UPC Universitat Politècnica de Catalunya

WP Work Package

[This page is intentionally left blank]